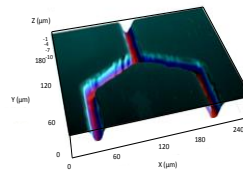
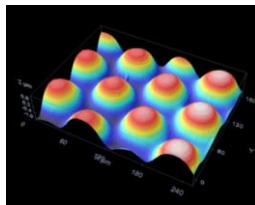




MICROSTRUCTURING OF GLASS BY LASER IRRADIATION: APPLICATIONS ON MICROOPTICS AND MICROFLUIDICS

(MICROESTRUCTURADO DE VIDRIO MEDIANTE IRRADIACIÓN LASER:
APLICACIONES EN MICROOPTICA Y MICROFLUÍDICA)

DOCTORAL THESIS



Daniel Nieto García

Área de Óptica, Departamento de Física Aplicada
Universidade de Santiago de Compostela

Dña. María Teresa Flores Arias y D. Justo Arines Piferrer, Profesora Titular de Universidad e Investigador “Isidro Parga Pondal”, respectivamente, del Área de Óptica del Departamento de Física Aplicada de la Universidade de Santiago de Compostela.

INFORMAN

que la presente memoria, titulada “ Microstructuring of glass by laser irradiation: applications on microoptics and microfluidics” ha sido realizada por **D. Daniel Nieto García** bajo su dirección y constituye la Tesis que presenta para optar al Grado de Doctor en Fotónica e Tecnoloxías do laser

Santiago de Compostela, 1 de Junio de 2012

Vº. Bº Director de la Tesis

Vº. Bº Director de la Tesis

María Teresa Flores Arias

Justo Arines Piferrer

El Doctorando

Daniel Nieto García

This work has been funded by the Ministerio de Ciencia e Innovación (MICINN) under the projects TEC2006 10496, CEN 2007-2014, SURFALUX SOL-00030930 and MAT2010-18519; by Xunta de Galicia/FEDER through the project INCITE08PXIB206013PR.

a Mar y a Izan

Summary

The aim of this thesis is to develop a method for fabricating microlens and microfluidic microchannels on soda-lime glass. The method consists in a combination of the laser direct write technique for fabricating the promoting glass structures, a wet chemical etching to remove the imperfections generated during laser ablation and a thermal treatment for reshaping and or improving of the optical and morphological qualities of the generated microlens and microfluidic microchannels.

The laser direct write technique used for glass microstructuring consists of a pulsed laser combined with a galvanometer system for addressing the output laser beam. Using this configuration cylindrical post and microchannels on soda-lime glass are fabricated. A later wet chemical etching technique (HF) is used successfully to carry out the surface smoothing and eliminate secondary structures generated during lasing the soda-lime glass. The mechanism to modify the surface roughness and shape by etching is also studied. Finally, a thermal treatment is used to modify the shape and the roughness of the element. Thanks to the thermal reflowing of glass it was possible to obtain microlens and microchannels in different configurations with a roughness of 7.35 nm, which is two orders of magnitude below the roughness after laser microstructuring. It was also investigated the influence of temperature, heating time and the mechanism of thermal displacement on the shape of the fabricated elements. In parallel to the fabrication process, it was investigated the interaction between a laser beam and the glass materials, presenting an overview of the ablative process on soda-

lime glass. The influence of impurities, the role of roughness and defects at surfaces, and the effect of the pulse width in the ablation process are also studied. The beam spot size, pulse overlapping, ablation threshold and debris deposition are investigated and optimized for fabricating optimal elements. Additionally, it is presented the mechanism of the ablative process using a thin film layer deposited over the glass. From this experiments it was identified the presence of Sn impurities only in one side of soda-lime glass, which acts as enhancement mechanism of the ablation process, reducing two orders of magnitude the ablation threshold. Finally, it is presented the structuring capabilities of microlens arrays for micro-patterning surfaces of materials. Surface multi-drilling, debris removing and microstructuring are some examples of application developed in this thesis. However, we observed in all this tasks a significant deterioration of the employed microlens arrays due to debris deposition on its surface. In order to reduce this degradation we propose and demonstrate the applicability of the Talbot effect which allows us to work with a bigger separation between the microlens array and the substrate, reducing the debris deposition, resulting in a longer lifetime for the optical element.

The outline of the thesis is presented as follows:

CHAPTER 1 gives a general introduction to the role of glass materials and its applications on micro-optics and microfluidics technologies. Besides, we describe some common methods used for microstructuring glass materials, focusing on the role of lasers and its different approaches.

CHAPTER 2 gives a general introduction to the mechanism that leads to laser ablation on glass and highlights the differences between nanosecond, picoseconds and femtoseconds pulses.

CHAPTER 3 introduces the soda-lime glass, the characterization tools for determining the morphological, optical and chemical composition, the lasers used and the furnace on which a thermal treatment was applied.

CHAPTER 4 presents an overview of the ablative process on soda-lime glass, the influence of impurities, the role of roughness and the defects of the surface and pulse width. The beam diameter, the ablation threshold and the debris deposition were also determined in this chapter. Additionally, it is presented the enhancements mechanism of the ablative process using a thin film layer deposited over the glass.

CHAPTER 5 reports the direct-write technique for fabricating plano-convex microlens and microchannels based on the laser ablation of a soda-lime glass. The wet chemical etching technique used to carry out smoothing of surfaces fabricated on the soda-lime glass and their dependence on the etching time were studied. Analysis of the thermal treatment applied to modify the shape and reduce the roughness of the elements, the influence of temperature; heating time and the mechanism of thermal displacement are also described. Finally, a morphological and optical characterization of the elements fabricated is given.

CHAPTER 6 presents the structuring capabilities of microlens arrays for micro-patterning surfaces of materials on performing surface multi-drilling, debris removing and microstructuring. Exploitation of the Talbot effect for reducing the degradation of the microlens array is also demonstrated.

CHAPTER 7 presents the conclusions.

Contents

Summary	ix
1 Microoptics fabrication techniques	
<hr/>	
1.1 Introduction	2
1.2 Importance of glass	2
1.3 Microstructuring of glass	4
1.3.1 Direct laser ablation of glass	5
1.3.2 In-direct laser ablation of glass	7
1.3.3 Etching	9
1.3.4 Precision glass molding	11
1.3.5 Mechanical micromachining : grinding and polishing techniques	12
2 Laser–Glass ablation mechanism	
<hr/>	
2.1 Introduction	16
2.2 Laser Ablation mechanism	17
3 Materials, instrumentation and characterization methods	
<hr/>	
3.1 Introduction	28
3.2 Glass material	28
3.3 Lasers	31
3.4 Thermal treatment	33

3.5	Characterization methods	34
3.5.1	Confocal microscope	34
3.5.2	Scanning electron microscope	35
3.5.3	Optical microscope	37
3.5.4	UV/VIS Spectrophotometer	38
3.5.5	Beam profiler	40

4 Ablative process of soda-lime glass

4.1	Introduction	44
4.2	Role of Impurities	45
4.3	Role of surface roughness	49
4.4	Influence of pulse width	51
4.5	Laser ablation parameters optimization	55
4.5.1	Ablation threshold and beam diameter	55
4.5.2	Mark analysis and pulse overlap	57
4.5.3	Debris deposition	62
4.6	Enhancement of ablative process using a thin absorber layer	64
4.6.1	Factor affecting the ablation region:	
	Role of roughness	66
4.6.2	Factors affecting the ablation region:	
	Role of diffusion	70
	4.6.2.1 Diffusion at covering the glass	70
	4.6.2.2 Diffusion during ablation	71
4.6.3	Factors affecting the ablation region:	
	Role of charge transfer	75

5 Microstructuring of glass: fabrication and characterization

5.1 Introduction	80
5.2 Laser microstructuring of glass	80
5.3 Thermal treatment	83
5.4 Chemical etching	87
5.5 Morphological and optical characterization	96
5.5.1 Microlens	96
5.5.2 Optical aberrations	103
5.5.3 Microchannels	111

6 Applications on surfaces microstructuring

6.1 Introduction and motivation	120
6.2 Structuring capabilities of microlens arrays	121
6.2.1 Surface microstructuring	122
6.2.2 Selective elimination of thin films	125
6.2.3 Removing of contaminated layers	126
6.3 Talbot effect	127

Conclusions	133
--------------------	-----

References	141
-------------------	-----

Resumen (<i>castellano</i>)	153
------------------------------------	-----

List of publications	166
-----------------------------	-----

CHAPTER 1

MICROOPTICS FABRICATION TECHNIQUES

This chapter gives a general introduction to the role of glass materials and its applications on micro-optics and microfluidics technologies. Besides, describes the commonly used methods for microstructuring glass materials, focusing on the role of lasers and its different approaches.

1.1 Introduccion

Glass materials due to their inertness and other thermo-mechanical attributes are suitable for many micro and nanotechnological applications. Micro-optics and microfluidics demands high quality microstructures on glass. The large and well developed glass micromachining toolbox provide the capability to obtain microstructures with high precision and repeatability. Common techniques used for microstructuring glass are wet etching, deep reactive ion etching, precision glass molding, polishing, grinding and laser ablation.

Laser ablation, because of its non-contact nature, allows the micromachining and surface patterning of glass materials with minimal mechanical and thermal deformation. Due to the low cost, the ease to implement in industry, and the wide quantity of lasers available, this technique is extremely important for machining glass.

1.2 Importance of glass.

Glasses are extremely useful and important optical materials, which have been widely used in optical instruments as windows or lenses. Due to their inertness and other thermo-mechanical attributes, glasses are suitable for many applications. Glasses are not crystalline solids, so do not exhibit the optical anisotropy that is characteristic of some crystals, and because glass has quite distinct properties from silicon, PMMA and metals, applications exist where only glass devices meet the requirements [Karthe1995].

Most glasses are composed of sand (Silica) mixed with other chemicals. By adding different chemicals to silica during the fusion process it is possible to fabricate different kinds of glass that differ in the refraction index and the wavelength range for transmission. It can be expected that, since silica is a glass, it presents

the same characteristic as insulators. Optically, they are transparent in the visible region, absorb in the UV due to the electronic transitions, and in the IR due to vibrational absorption [Sugioka2004].

The main advantages of glass derive from its specific characteristic including properties such as that it is natural, inexpensive and highly aesthetic. These make it suitable for manufacturing on sustainable and healthy material. For many applications in clinical medicine, biology and chemistry, glass is the preferred material. Some of these applications involve the microstructuring of glass [Coughlan2008].

Micro-optics: micro-optics play an important role in various industrial production processes, like micro-electronics, laser micro-machining, materials processing, optical inspection, machine vision and precision metrology. Micro-optics elements are additionally found in the medical industry, analytical systems in bio-photonics and optical sensors. Various applications and their subsequent requirements with respect to cost structure, accuracy, quality and lifetime, caused different manufacturing technologies [Flores-Arias2009, Sohn2005].

Traditionally, three different kinds of materials are used for micro-optics: glass, polymers and crystal. Of course polymer optics is the most cost-effective solution, however, they have some limitations due to the reduced number of materials with different refractive index, limited stability at higher temperatures, burning at high laser powers, transparency and degradation under UV-light. These limits can be overcome by using glass.

Microfluidics: Microfluidics refers to a set of technologies that control the flow of minute amounts of liquids or gases in a miniaturized system. The use of

microfluidic devices is making rapid inroads in the modern analytical laboratory, primarily because of their small physical footprint, speed and efficiency of chemical separations, and reduced reagent consumption. Traditionally, lab-on-a-chip devices have been manufactured in silica due to its well understood surface chemistry and favourable micromachining techniques that are ubiquitous in the microelectronics industry. Recently researchers have begun to utilize devices fabricated from polymer substrates as an alternative to glass, although in clinical medicine, biology and chemistry, glass may still be the preferred materials. Microchannels fabricated on glass have a growing importance in the miniaturization of microfluidic devices for chemical and biological micrototal analysis system [Cheng2004, Malalahalli2004, Erickson2004].

1.3 Microstructuring of glass.

The large and well developed glass micromachining methods provide the capability to obtain microstructures with high precision and repeatability. Common techniques used for microstructuring glass are laser ablation, etching, precision glass molding and mechanical micromachining. Laser micromachining offers a single-step method for direct writing of microchannels in glass. Using this laser ablation technique, it is possible to fabricate geometries with variable depth and high aspect ratio that cannot be achieved through traditional microlithographic techniques. The mechanical rigidity, chemical resistance, and low permeability properties of glass, combined with their optical transparency, make them a good choice for many demanding lab-on-a-chip applications.

Although some techniques have been widely used for structuring glass most of them are complex, high in cost and come with significant contamination risk. Table 1.1 shows the common methods used for microstructuring glass materials.

Table 1.1 Commonly methods used for microstructuring glass.

Technology	Substrate configuration	Material	Tool/Master/Mask
<i>Laser-direct write</i>	<i>Substrate based</i>	<i>Glass</i>	<i>None</i>
<i>Laser-Indirect write</i>	<i>Substrate based</i>	<i>Glass</i>	<i>Absorption source</i>
<i>Etching</i>	<i>Wafer based</i>	<i>Glass</i>	<i>Mask for optical lithography</i>
<i>Precision glass molding</i>	<i>Substrate based</i>	<i>Special thermal Glass</i>	<i>Mold pre-form</i>
<i>Mechanical micromachining: grinding and polishing</i>	<i>Single optics</i>	<i>Glass</i>	<i>None</i>

1.3.1 Direct Laser ablation of glass.

Laser has become increasingly important in recent years for many fields, including micro-optics, micro-electronics, micro-biology, and micro-chemistry. High micromachining quality with ns-pulse and fs-pulse lasers was demonstrated for direct ablation of dielectrics [Liu1997].

Laser ablation, because of its non-contact nature, allows the micromachining and surface patterning of glass materials with minimal mechanical and thermal deformation. Due to the low cost, the ease implementation in industry, and the wide quantity of lasers available, this technique is extremely important for machining glass.

For transparent materials, in the visible spectral range, laser ablation should ideally be performed with ultraviolet radiation because of the linear optical

absorption in this wavelength range. Alternatively, non-linear coupling of ultra-high-intensity laser pulses in the near-IR range with sub-picosecond duration may show advantages. The interaction between a laser beam and a material is determined by: (1) laser characteristics (the wavelength, fluence or energy density, the pulse duration, repetition rate and pulse energy); (2) the properties of the material (absorption characteristics, thermal relaxation,) which is governed by the composition and structure of the material.

From the earliest work on laser interactions with materials, direct-write processes have been important and relevant techniques to modify, add, and subtract materials for a wide variety of systems and applications. In general, direct-write processing refers to any technique that is able to create a pattern on a surface or volume in a serial or “spot-by-spot” fashion. This is in contrast to lithography, stamping, directed self-assembly, or other patterning approaches that require masks or pre-existing patterns [Hirai2003, Wensink2000].

Laser direct-write subtraction (LDWS) is the most common type of laser direct-write. In general, this entails processes that result in photochemical, photothermal, or photophysical ablation on a substrate or target surface, directly leading to the features of interest. Common processes include laser scribing, cutting, drilling, or etching to produce relief structures or holes in materials in ambient or controlled atmospheres. The fundamental interactions leading to material removal can be thermal or athermal, depending primarily on the material characteristics and the pulse duration of the laser [Li2001, Mannion2004].

On laser direct-write modification (LDWM) the incident laser energy is usually not sufficient to cause ablative effects but is sufficient to cause a permanent change in the material properties. Typically, these processes rely on thermal modifications that cause a structural or chemical change in the material. A

common example of such processes is the rewritable compact disc, in which a diode laser induces a phase transition between crystalline and amorphous material. Many LDWM applications require a specific optical response in the material of interest beyond simple thermal effects. Optically induced defects or changes in mechanical properties can lead to many non-ablative material modifications [Cheng2004].

Laser Direct-Write Addition (LDWA) is perhaps the most recent of the laser direct-write processes. In this technique, material is added to a substrate using various laser-induced processes. Many techniques are derived from laser induced forward transfer (LIFT), where a sacrificial substrate of solid metal is positioned in close proximity to a second substrate to receive the removed material, the incident laser is absorbed by the material of interest, causing local evaporation. This vapor is propelled toward the waiting substrate, where it recondenses as an individual three-dimensional pixel, or voxel, of solid material [Piqué2006].

1.3.2 In-direct laser ablation of glass.

Since the ablation of transparent materials using IR wavelength is complicated due to low absorption, it can be easily understandable that some kind of element placed at the surface or backside of the transparent material can be able to confine the impinging laser beam which will lead to transfer energy from the interaction laser-absorber layer to the transparent material.

There are several indirect laser methods, which are suitable processing of non-absorbing targets. One of them is laser-induced plasma-assisted ablation (LIPAA). Another group of indirect methods are based on an absorbing material contacting the backside of the transparent target. The most common techniques that frequently use absorbers are: condensed vapour in the laser etching at a surface

adsorbed layer (LESAL), liquids in laser-induced backside wet etching (LIBWE) or solid thin films in the case of laser-induced backside dry etching (LIBDE).

In the LIPAA, the substrate must be transparent to the wavelength of the laser beam, so the laser beam goes through the substrate first, and then irradiates a metal target placed behind the substrate. At laser fluence below the damage threshold of the substrate and above the ablation threshold of the target, the plasma generated from the target surface propagates to the rear surface of the substrate at high speed. Strong interactions among the laser beam, the plasma, and the substrate take place, resulting in high-quality ablation with neither cracks nor severe distortions at the rear side of the substrate [Sugioka2004, Hanada2004].

A similar configuration is needed in case of LESAL. The substrate must be transparent for the wavelength of the laser beam, so the radiation goes through the substrate first, and then irradiates the absorber layer deposited at the rear side of the substrate. The absorber layer is usually deposited by vapour deposition. At laser fluence below the damage threshold of the substrate and above the ablation threshold of the target, the plasma generated from the interaction of the laser with the absorber layer transfers the energy to the substrate which leads to the ablation process [Ihlemann2008, Hopp2009, Zimmer2008].

LIBDE follows a configuration and mechanism like that of LESAL, although differs on using a solid thin film at the rear side of the transparent materials to be etched [Hopp2009]. On LIBWE the laser beam passes through a transparent substrate and is absorbed by a dye solution located at the rear surface of the substrate [Kopitkovas2003, Kopitkovas2007, Smausz2007, Huang2007]. The principle of LIBWE is based on the generation of intense temperature and pressure increase at the thin interface between the material and liquid. Due to strong laser absorption

by the dye solution, the laser energy is confined into a thin layer at the interface between the transparent substrate and the solution. The photo-activated layer interacts with the surface of the substrate, resulting in etching. The major difference with other techniques which are used for structuring of transparent materials is the application of conventional excimer lasers and an organic liquid which strongly absorbs the laser radiation.

1.3.3 Etching.

Etching is used in microfabrication to chemically remove layers from the surface of a wafer during manufacturing. Wet etching technique (HF etching) is commonly used to create channels and structures in glass [Haixin2009, Grosse2001, Steingoetter2005]. In the HF technique, etching is used to chemically remove the glass materials from the surface precisely protected using a mask. With this technique the amount of channels, reservoirs, mixing and reaction chambers is irrelevant for the cost of the process. Wet etching of glass is an isotropic etching technique. This means that the width of the channels is more than twice the depth of it, and that the corners are rounded. The bottom of the channel stays smooth and optically transparent.

Another etching method for machining glass is Reactive-ion etching (RIE). It uses chemically reactive plasma to remove material deposited on wafers. The plasma is generated under low pressure (vacuum) by an electromagnetic field. High-energy ions from the plasma attack the wafer surface and react with it. Plasma is initiated in the system by applying a strong electromagnetic field (in the radio frequency range) to the wafer platter. The oscillating electric field ionizes the gas molecules by stripping them of electrons, creating the plasma [Thienot2006, Righini1991]. Because of the large voltage difference, negative ions tend to drift toward the

wafer platter, where they collide with the samples to be etched. The ions react chemically with the materials on the surface of the samples, but can also sputter some material by transferring some of their kinetic energy. Due to the mostly vertical delivery of reactive ions, reactive-ion etching can produce very anisotropic etch profiles, which contrast with the typically isotropic profiles of wet chemical etching. Figure 1.1 shows the anisotropic and isotropic etching.

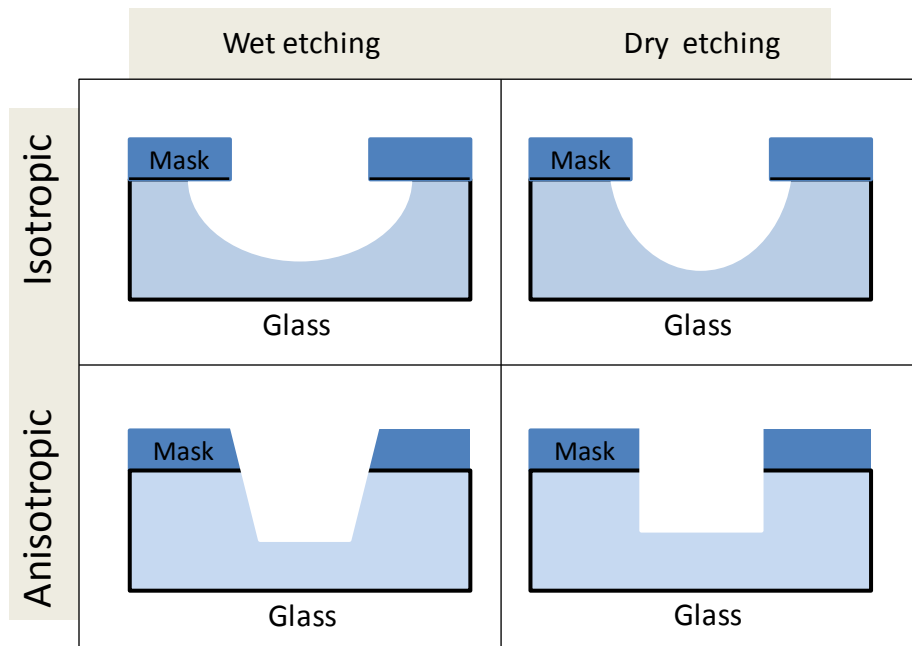


Figure 1.1 Anisotropic and isotropic etching.

Using Deep Reactive Ion Etching (DRIE or plasma etching) it is possible to create deep, high density and high aspect ratio structures in glass substrates [Akashi2006, Li2001]. Although this is an accurate technique, due to the nature of the process, it is a very expensive method and difficult to scale industrially, in comparison with other techniques. Table 1.2 shows the main characteristics of wet and dry etching.

Table 1.2 main characteristics of wet and dry etching.

	Wet	Dry (Plasma and RIE)
<i>Method</i>	<i>Chemical solutions</i>	<i>Ion Bombardment or Chemical Reactive</i>
<i>Environment and Equipment</i>	<i>Atmosphere, bath</i>	<i>Vacuum chamber</i>
<i>Advantage</i>	1)Low cost, easy to implement 2)High etching rate 3)Good selectivity for most materials	<i>Capable of defining small feature size (< 100 nm)</i>
<i>Disadvantage</i>	1) Inadequate for defining feature size < 1 μ m 2) Potential of chemical handling hazards 3) Wafer contamination issues	1)High cost, hard to implement 2)low throughput 3)Poor selectivity 4)Potential radiation damage
<i>Directionality</i>	<i>Isotropic (Except for etching Crystalline Materials)</i>	<i>Anisotropic</i>

1.3.4 Precision glass molding.

Precision glass molding is a replication process that allows us to manufacture large volumes of high precision optical components from glass [Su2008, Yi2006]. This process can be used to produce a large variety of optical free-form elements an array structures. It is used to manufacture precision glass lenses for consumer products such as digital cameras, and high-end products like medical systems.

Many glasses can be used with precision glass molding. However, there are some limitations. The glass transition temperature must not exceed the maximum heating temperature of the mould, the glass composition influences molding tool life and the coefficient of thermal expansion of mould and glass should match. Also, during the molding process, the glass exhibits a change in refractive index, called index drop, during the annealing process. This drop is caused by fast cooling of the mould insert, inducing a small amount of residual stress in the glass. As a result, the glass exhibits a small index change when compared to its fine anneal

state. Besides, the mould has some limitations. It must have sufficient strength, hardness and accuracy at high temperature and pressure. Good oxidation resistance, low thermal expansion and high thermal conductivity are also required. The material of the mould has to be suitable to withstand the process temperatures without undergoing deforming processes. Therefore, the mould material choice depends critically on the transition temperature of the glass material. Mold materials include tungsten carbide, vitreous carbon, aluminum alloys, silicon carbide, silicon nitride and a mixture of silicon carbide and carbon.

1.3.5 Mechanical micromachining: grinding and polishing technologies.

The fabrication of classical macroscopic optical components is traditionally based on mechanical techniques such as grinding and polishing. Grinding and polishing glass is similar to doing the same operations on any hard material.

- Grinding makes use of coarse particles of hard material to rapidly remove large quantities of glass, for shaping or for removing gross surface imperfections [Kurmar2006, Luo2006, Philips1977].
- Polishing uses particles of ever decreasing size and often of softer materials to remove finer surface imperfections, so that any remaining is too small to scatter the light [Wang2002].

The abrasive materials are often attached to paper, bonded to discs or machined shapes to allow them to be used with power tools. The waste product produced can clog the surface and reduce the cutting action, so water is used to help flush it away. The use of water is important when grinding glass to prevent the localized build-up of heat, which could break small pieces and cause fine crazing in larger pieces. Available materials suitable for scratching glass, and thus for grinding and polishing it include; diamond, silicon carbide, corundum, aluminum oxide and

Garnet. Grinding and polishing can be done to pieces large or small; using a range of electric or air powered tools, grinding wheels or discs, polishing mops or hand held pads. Some applications include, removing mold marks from glass castings, shaping large sharps, improving edges of mating pieces, removing imperfections and obtaining clarity and brilliance of glass substrates

There are several problems related to mechanical micromachining fabrication. Due to the mechanical alignment of the machining tool and the movement of the substrate, the precision of the fabricated microrelief strongly depend on the geometry of the surface relief profile.

CHAPTER 2

LASER - GLASS ABLATION MECHANISM

This chapter describes the mechanisms that lead to laser ablation of transparent materials for long and ultra-short pulses. The primary interaction mechanisms, free electron generation, plasma formation and energy transfer to the lattice resulting in the ablation process are described here.

2.1 Introduction

During laser ablation, the energy that reaches the sample is absorbed, transmitted and reflected depending on the properties of the materials. The laser parameters, wavelength, pulse duration, repetition rate and the energy density of fluencies applied to the samples also determines the response of the material. The laser beam is absorbed by the sample through electronic and vibration excitation of the atoms, if the electric field exceeds a critical value; it results in a rapid ionization and the formation of plasma.

When the density of free electrons is above the plasma threshold, irreversible material breakdown occurs and ablation begins. The temperature increases with the number of photons reaching the sample, which also increase the fraction of light absorbed. At this time, the electrons absorb energy by collisions with ions and are heated to higher temperatures. The electrons also transfer energy to the lattice, which contributes to material heating. The amount of energy transferred to the lattice during the laser pulse depends on the pulse duration and on the energy coupling coefficient.

For pulse durations longer than a few tens of picoseconds, energy goes from the electrons to the lattice on the time scale of the pulse duration. In this case the damage occurs via heat deposition resulting in melting and boiling, and consequently an expansion and expulsion of material occurs [Yamamoto2010, Huang2010]].

On the other hand, for pulses shorter than a few picoseconds, the time scale for absorption is shorter than for energy transfer to the lattice, which decouples the absorption and the heating process of the lattice, which result in a direct vaporization of the material from the surface.

2.2 Laser Ablation mechanism

Laser induced breakdown is a process where a normally transparent material is first transformed into an absorber plasma by the strong laser pulse. After that, the plasma absorbs the laser energy and it causes an heating that leads to an irreversible damage at the surface material.

A conceptual framework for a physical model of laser ablation based on electronic processes incorporates [Miller2002]:

- The primary interaction mechanism of photons with solids surfaces,
- Electronic, vibrational and configurational electron-lattice relaxation,
- The evolution of defect and other characteristic vacancy cluster,
- Secondary energy-dissipation processes that produce the catastrophic nonlinear response typical of laser ablation.

The pulse duration and so the material response time is an important factor that will determine the kind of mechanism that leads to ablation of material.

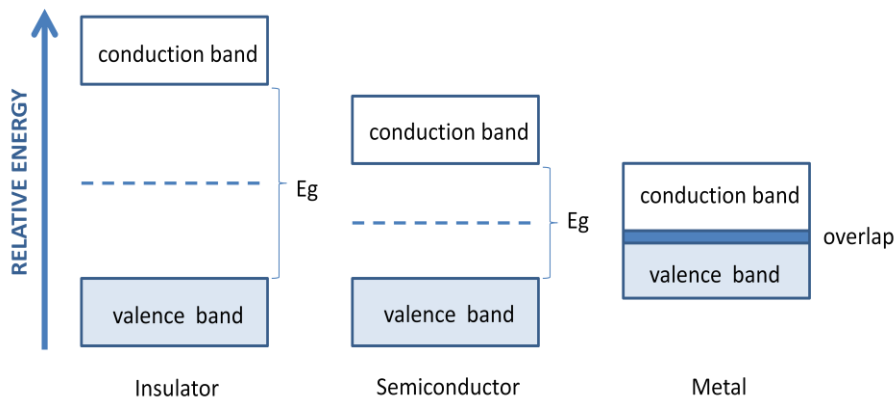


Figure 2 Diagram of valence and conduction band for insulators, semiconductors and metal.

The energy bands each correspond to a large number of discrete quantum states, and most of the states with low energy are full, up to a particular band called the valence band. The easiness with which electrons in an insulator can be excited from the valence band to the conduction band depends on the energy gap determining the wavelength range over which interband absorption takes place (fig.2.1).

The absorption of light, which leads to the ablation of transparent materials, comes from linear and nonlinear effects. Important characteristic of laser parameters such pulse durations and photon energy are involved in the kind mechanism that predominates. While using IR wavelengths and long pulses, avalanche effects is the responsible mechanism, with short pulse durations multiphoton absorption takes place [Sze2001, Fox2010].

As pointed above, the absorption of light, which leads to the ablation of materials, comes from a photophysical response which involves inter-band, intra-band and impurities effects (Fig.2.2).

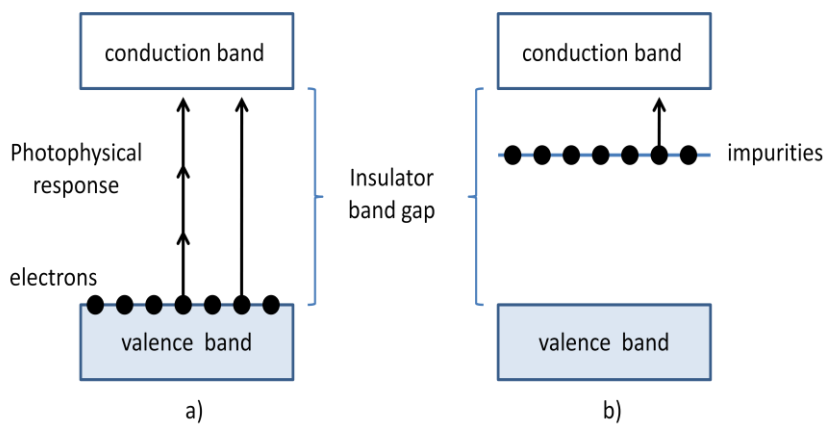


Figure 2.2 Diagram of the mechanism of absorption of light on transparent materials through a) single and multi-photon inter-band absorption and b) impurity-based absorption.

At the initial stages of pulsed laser interaction with dielectrics, the process that contributes to the formation of free electrons are multiphoton absorption, absorption at lattice and surface defects, nonlinear absorption and chemical decomposition. At high intensity threshold a free electrons gas in the conduction band of the dielectric is formed, which leads to a strong absorption.

Classically, a free-electron generation in dielectrics is given by a single rate equation describing the increase of the total free electron density inherent in the conduction band n_{total} , eq. (2.1) [Rethfeld2006],

$$\frac{dn_{total}}{dt} = n_{pi}(E_L) + \alpha(E_L)n_{total} \quad (2.1)$$

This equation combines the probability of photoionization n_{pi} , directly depending on the amplitude of the electric laser field E_L , with the impact ionization, assumed to depend on the total free electron density. Due to photoionization, electrons are shifted from the valence band into the conduction band, [Keldysh1965]. In contrast electro-electron impact ionization is caused by a free electron already existing in the conduction band. If its kinetic energy is large enough, it may transfer part of it to an electron in the valence band, such that the latter is enabled to overcome the ionization potential [Keldysh1960, Bloemberger1964]. The avalanche coefficient α depends on the effective energy gain of the free electron in the electric laser field E_L and can be estimated by eq.(2.2)

$$\alpha = W_{1pt}(E_L)\hbar\omega_L/\varepsilon_{crit} \quad (2.2)$$

where, $W_{1pt}(E_L)$ is the probability of one intraband photon *absorption*, $\hbar\omega_L$ the *photon energy of the laser light*, and ε_{crit} the *critical energy of the impact*

ionization, which is on the order of E_{gap} , the band gap between the valence band and the conduction band.

Eq. 2.1-2.2 was proposed and verified for laser pulses in the nanosecond regime [Smith1978, Jones1989]. Experimental studies applying eq. 2.1, have led to contradictory results, refuting [Stuard1996, Apostolova2000] or emphasizing [Kaiser2000, Vatsa2002, Sudrie2002] the importance of the electron avalanche in picosecond and below, which has introduced doubts about the application of eq. 2.1 to ultrashort time scales [Manenkov1986, Bityurin2003]. One basic assumption of eq. 2.1 is that impact ionization depends directly on the total density of free electrons. However, the energy of a particular electron plays an important role, since the photoionization generates electrons with low kinetic energy in the conduction band while impact ionization requires electrons of high kinetic energies. The additional energy is absorbed from the laser light by intraband absorption. If this absorption process takes time comparable to the laser pulse duration, it can be appreciated that eq. (2.1) is oversimplified.

Multiple rate equation (MRE) [Rethfeld2004] provides a possibility of clarifying these controversies within the framework of a unified approach, valid on a broad range of time scales. On ultrashort time scales the shape of the electron distribution in the conduction band may change on time, thus energy-averaged total electron density n_{total} is not the adequate parameter to describe the ionization process.

Defining the density n_k of electrons above $\varepsilon_{\text{crit}}$, where κ will be identified with the number of photons necessary to reach $\varepsilon_{\text{crit}}$, a modified rate equation from ref [Rethfeld2004] can be formulated as eq. (2.3)

$$\frac{dn_{total}}{dt} = n_{pi}(E_L) + n_k \tag{2.3}$$

The difference in the last term of eq. 2.3 compared with eq.(2.1) is substantial. While in eq. (2.1) the impact ionization is assumed to depend on the total free-electron density, n_{total} , eq. (2.3) considers the fact that only those electrons which bear sufficiently high energy may produce impact ionization. Figure 2.3 shows an illustration of the process providing changes in the density and the energy, respectively, of free electrons in the conduction band of a dielectric.

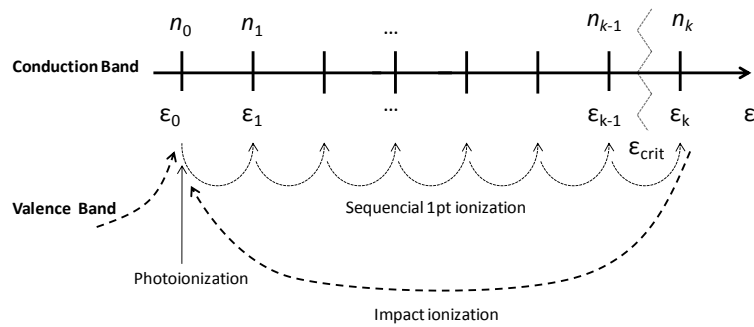


Figure 2.3 Illustration of the process of impact ionization. [Rethfeld2006]

When the density of electrons reaches the plasma threshold, irreversible material breakdown occurs and ablation takes place. After that the electrons transfer energy to the ions and the lattice, which results in heating of the material. The amount of energy transfer, hence the heating, during the laser pulse are conditioned by pulse duration and the energy coupling coefficient.

Since the heating time is equivalent to the pulse width, different interactions times are involved in transferring the energy from the laser to the lattice of the material. The ultra short pulse laser-matter interaction mode corresponds to conditions when the electron-to-ion energy transfer time and the heat conduction time exceed significantly the pulse. With all types of materials, ablation is strongly

non-stationary and starts only after about 1 to 10ps. The electron-phonon/lattice coupling time is in the range of 1 ps and the overall relaxation time is in the range of 200 ps (fig. 2.4).

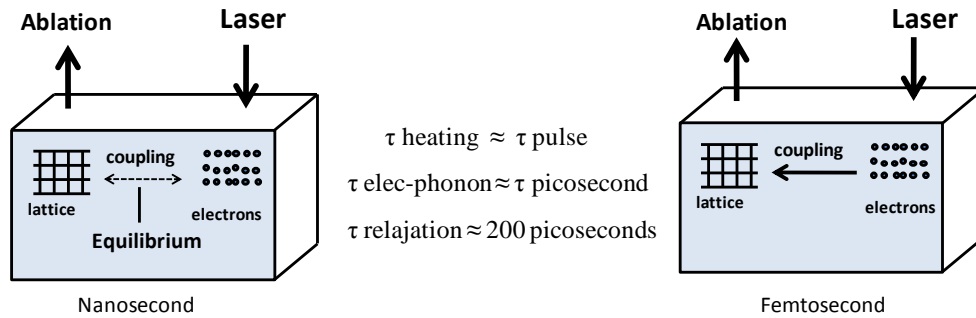


Figure 2.4 Sketch of electron-phonon coupling time.

The electron-to-lattice energy exchange time is, in a long-pulse ablation mode, of several orders of magnitude shorter than the pulse duration. By this reason the electrons and ions are in equilibrium, and ablation has a conventional character of thermal expansion. By contrast, for the short pulse interaction the electron-to-ion energy exchange time, as well as the heat conduction time, is much larger than the pulse duration, and the ions remain cold. Electrons can gain energy from the laser field in excess of the Fermi energy, and escape the target. The electric field of a charge separation pulls ions out of the target thus creating an efficient non-equilibrium mechanism of ablation.

In conventional continuous wave and long pulse (nanosecond) laser processing, the mechanism that dominates the ablation process is the heating of the target material through the liquid phase to the vapor phase, resulting in expansion and expulsion of material. This is accompanied by heating and collateral damage to the surrounding area, the degree of which is determined by the rate of energy absorption and the rate of energy loss through thermal conduction in the

material. This collateral damage is a limiting factor when high precision ablation is required.

On the other hand, due to their peak intensities, ultrashort (picosecond and femtosecond) pulses ablate material via the rapid creation of plasma that absorbs the incident energy resulting in direct vaporization of material from the surface. This produces negligible collateral heating and shock-wave damage (fig.2.5).

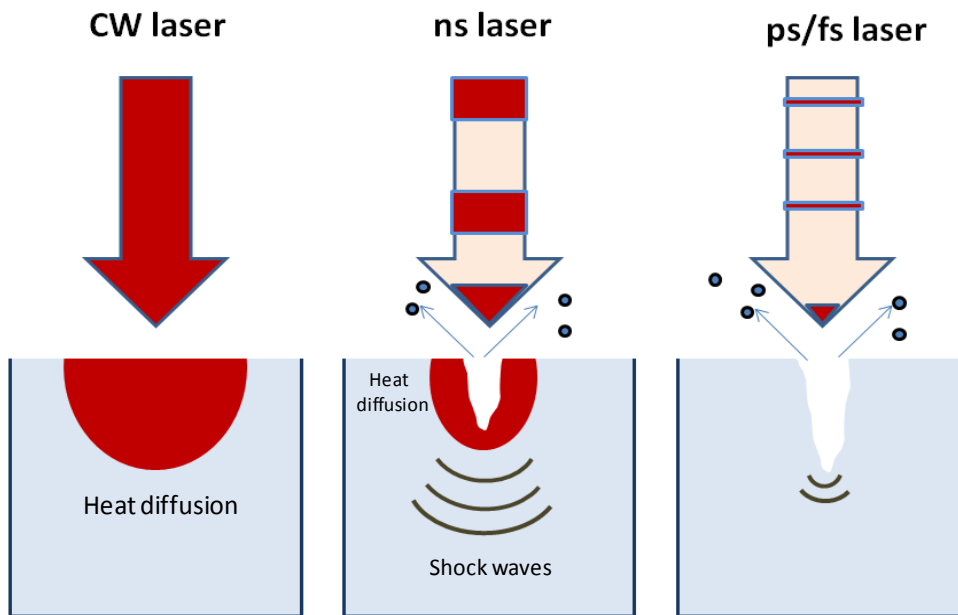


Figure 2.5 Sketch of the different mechanism related with the pulse width.

By decreasing the pulse widths, the laser field strength increases, which means short interaction time. The electrons achieve more energy, reaching a few to tens of electron volts, in contrast with the low energy of the lattice, which remain relatively cold. After the laser pulse is over, the electron-ion energy transfer will heat the ions to much higher temperatures compared to the long pulse cases and the material is vaporized directly without suffering a melting phase. Because of the short interaction time the heat affected zone is significantly smaller.

After reaching the melting (long pulses) or vaporization (short pulses) temperatures, the material is damaged, which is also accompanied by acoustic waves and optical radiation.

The energy is deposited in a surface layer and the thickness is given by the absorption or penetration skin depth $l_s = \frac{1}{\beta}$, where β is the absorption coefficient. The heat diffusion length during the pulse gives the heat penetration depth due to thermal conduction. This diffusion length is given by eq. 2.4.

$$l_d = \sqrt{D\tau_l} \quad (2.4)$$

where D is the heat diffusion coefficient and τ_l is the laser pulsewidth. For long pulses, $l_d > l_s$ and the volume of the material heated by the laser pulse, hence the temperature, is determined by the heat diffusion length during the laser pulse. Therefore, for long pulses, the fluence breakdown threshold varies with laser pulsewidth as $F_{th} \propto \sqrt{\tau_l}$.

As the laser pulsewidth decreases to a value τ_c such that $l_d = \sqrt{D\tau_c} < l_s$, the skin depth determines the heated volume during the laser pulse. It can be applied to transparent materials once significant absorption due to plasma generation occurs, and it has been used to explain the observed scaling $\sqrt{\tau_l}$ of the breakdown threshold [Krzystof2005].

When using long pulses a large volume of material is heated and melted, the ablation and material removal is accomplished through melt expulsion by the vapor pressure and the recoil of the light pressure. In this case the heat diffusion is larger than the skin depth.

In some micromachining applications with long pulse lasers the melt material generated after the ablation can lead to very irregular shapes. On the other hand, when using ultrashort pulses, the deposited laser energy is limited in a layer with a thickness l_s , so the material pass from the liquid phase to the vapor phase with high kinetic energy. Plasma shielding is strongly diminished or even avoided. Thus, ultrashort pulses allow strong material excitation prior to the expansion of the plasma plume [Bäuerle2006]. The heat affected zone tends to be smaller than the focus when applying a laser with fluence just at the ablation threshold. The material is removed away by direct vaporization from the surface.

Most of this process takes place after the laser pulse is over. Although, the material is still heated, the thickness of the melt layer is small. As the heated material is evaporated the material turn into cold due to the steep temperature gradient and because of the absorbed laser energy is carried away by evaporation. Because of this ablation and material removal using short pulses is more precise compared with long pulses case.

CHAPTER 3

MATERIALS, INSTRUMENTATION AND CHARACTERIZATION METHODS

In this chapter a short introduction of soda-lime glass is given. The characterization tools for determining the morphological and chemical composition, the lasers used and the furnace on which a thermal treatment was applied are also described.

3.1 Introduction

The characterization of glass samples before laser processing is of crucial importance. This let us to identify the mechanism that leads to ablation process and so to ensure the repetitiveness. The transmission spectrum was obtained with a PerkinElmer Lamb25 spectrometer and the composition was determined using EDX analysis performed with a Scaning electron microscope FESEM ULTRA Plus.

The lasers used in our experiments were a *Rofin power e-line* operating at 1064 nm wavelength and 20 ns pulsewidth, a picosecond *Trumpf Trumicro 5050* system operating at 1030 nm wavelength and 10 ps pulsewidth and a femtosecond pulse *Amplitude Systemes S-pulse HP* operating at 1030 nm wavelength and 500 fs pulse width.

The finished samples were examined using both optical and confocal microscopes. The optical microscope MM-400 was used to visualize the sample and pre-determine damage at the surface. The confocal microscope SENSOFAR 2300 Plμ was used for topography measurement and 3D mapping of the fabricated elements. The irradiance distribution of the laser beam and the microlens spot size and irradiance at focus were analyzed using a beam profiler BP-109UV.

3.2 Glass material.

Soda Lime Glasses

Soda lime glass is the most used commercial glass, with minor additions of other oxides to adjust the properties of specific applications. Addition of soda-lime to silica results in a large decrease in the temperature required for melting, but in the other hand, a large amount of soda also lead to poor chemical durability of

the glass. Replacement of a portion of soda (Na_2O) by lime (CaO) partially offsets the reduction in chemical durability and results in a glass with a reasonable melting temperature ($\approx 1500\text{ }^\circ\text{C}$), while maintaining acceptable properties for most consumer applications.

The soda-lime glasses used in this work were characterized in terms of optical transmission and chemical composition. The transmission spectrum of soda-lime glass, obtained with a PerkinElmer Lamb25 spectrometer, is showed in figure 3.1

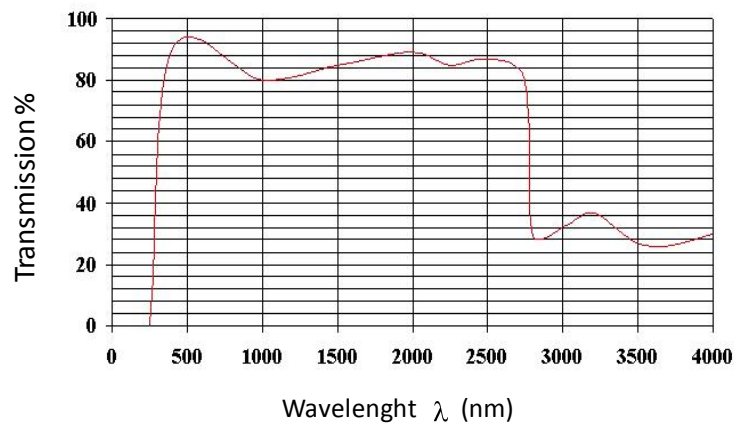
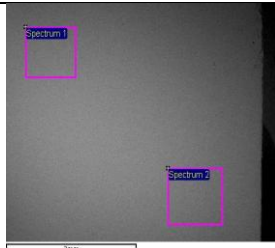
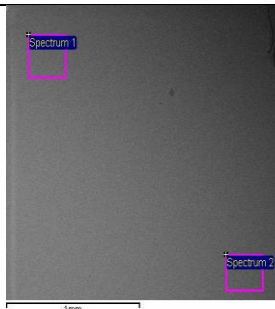


Figure 3.1 Transmission spectrum of soda-lime glass.

The composition of the glass was determined using EDX (table 3.1). The analysis reveals the presence of Sn only in one side of the glass. This is related to float technique used for producing window glasses, which causes diffusion of tin into the glass surface when in contact during the molding step. The other face, which is in contact with inert atmosphere, is weakly contaminated with tin. Thus float glass is composed of two composite surface layers and a bulk. That is important for the laser ablation process, since the Sn impurities acts as absorber centers enabling the ablation of glass (see section 4.2 for details).

Table 3.1 Chemical composition of soda-lime glass

Front side	Spectrum 1			Spectrum 2		
	Element	Weight	Atomic	Element	Weight	Atomic
	O	50.25	63.51	O	50.15	62.55
	Na	9.08	7.99	Na	9.40	6.44
	Mg	2.19	1.82	Mg	2.34	2.08
	Al	0.54	0.40	Al	0.41	0.30
	Si	33.08	23.82	Si	32.66	23.49
	Ca	4.87	2.45	Ca	4.72	2.32
Totals	100.00			100.00		

Rear side	Spectrum 1			Spectrum 2		
	Element	Weight	Atomic	Element	Weight	Atomic
	O	48.97	63.00	O	52.08	63.78
	Na	9.14	8.18	Na	9.30	7.92
	Mg	2.24	1.90	Mg	2.30	1.86
	Al	0.49	0.37	Al	0.43	0.31
	Si	32.34	23.70	Si	30.82	24.15
	Ca	4.91	2.52	Ca	3.55	1.74
	Sn	1.90	0.33	Sn	1.52	0.25
Totals	100.00			100.00		

We analyzed also the mechanical, thermal, optical and electrical properties of the soda-lime glasses provided by our supplier. We show in table 3.2 the data collected during those measurements.

Table 3.2 Mechanical, thermal, optical and electrical properties of soda-lime glass.

Mechanical	Thermal	Optical	Electrical
Rigidity (Shear): 3.0×10^{10} Pa	Thermal Conductivity: 0.937 W/mK	Refractive Index: 1.523 (at 633nm)	Dielectric Constant: @ 20°C E= 7.75
Elasticity(Young's): 7.2×10^{10} Pa	Thermal Coefficient of Expansion (0/300 °C): $8.6 \times 10^{-6}/^{\circ}\text{C}$		Specific Resistivity: log R ohms/cm: 11@60Hz,25°C 9.7@1000Hz, 25 9.1@1000Hz,100°C 6.5@1000Hz,250°C
	Softening Point: 726°C/1340°F		
Hardness (Moh's Scale): 6 - 7	Annealing Range: 546°C/1015°F		
	Strain Point: 514°C/957°F		

3.3 Lasers

The lasers used in our experiments were: (1) a *Rofin power e-line* operating at 1064 nm wavelength and 20 ns pulsewidth (fig.3.2); (2) a picosecond *Trumpf Trumicro 5050* system operating at 1030 nm wavelength and 10 ps pulsewidth (fig.3.3); (3) and a femtosecond pulse *Amplitude Systemes S-pulse HP* operating at 1030 nm wavelength and 500 fs pulse width (fig.3.4). The laser specifications are showed in table 3.3.



Figure 3.2 Nanosecond laser work station.



Figure 3.3 Picosecond laser work station.

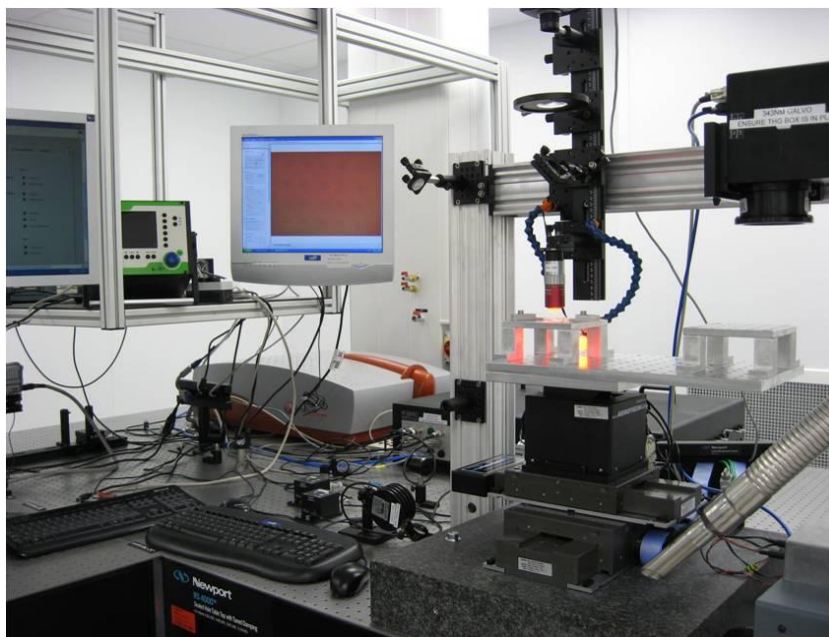


Figure 3.4 Femtosecond laser work station.

Table 3.3 Specifications of lasers.

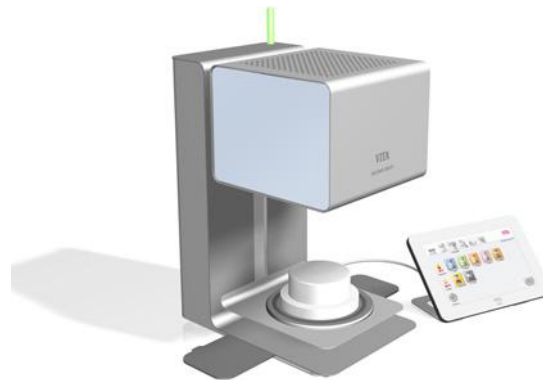
Lasers parameters	Femtosecond	Picosecond	Nanosecond
Laser sources:	Diode Pumped Femtosecond based on Ytterbium crystal technology	Diode Pumped Picosecond laser based on Thin Crystal Disk technology	Nd:YVO ₄
Wavelength:	1030 nm	1030 nm	1064nm
Pulse Duration:	500 fs	<10 ps	8-200 ns
Pulse Energy:	1mJ	125 μ J	105 μ J
Average Power:	up to 4W	50 W	20W
Pulse Repetition Rate:	Single Pulse to 300 kHz	Single shot to- 400 kHz	Single shot to - 200kHz
M²	1.2	1.3	1.2

3.4 Thermal treatment.

The thermal treatment was applied in two different ovens; (1) a *Heraeus* mufla oven; (2) and a *VITA Vacumat* (fig 3.5). Table 3.4 shows the operational specifications of both devices.



a)



b)

Figure 3.5 a) Heraeus mufla oven and b) VITA Vacumat mufla oven.

Table 3.4 Operational specifications for the Mufla ovens.

Heraeus mufla oven	VITA Vacumet 6000M
Temperature range 40 °C- 1100 °C	Temperature range 200 °C- 1100 °C
Adjustable fresh air supply	Vacuum setting options, pre-vacuum and main vacuum can be selected
Thermal stability ± 1 °C ± 10 °C	Temperature accuracy ± 1 °C
Thermal speed 0.1 °C/min....40 °C/min	
Uniformity at 1000: ± 4 °C	
Thermal Accuracy ± 1 °C	
Thermicon P digital program controller	

3.5 Characterization methods

The tools used for determining the topographical and compositional data were a confocal microscope and a scanning electron microscope, respectively.

3.5.1 Confocal microscope

The Confocal microscopy is an optical imaging technique used to increase optical resolution and contrast of a micrograph by using point illumination and a spatial pinhole to eliminate out-of-focus light in specimens that are thicker than the focal plane. It enables the reconstruction of three-dimensional structures and therefore the conduction of topographical analysis. In this thesis we use the confocal microscope SENSOFAR 2300 (fig. 3.6) [Sensofar]. This instrument is a non-contact optical profiler which uses a dual-technology sensor head combining both confocal and interferometric techniques.



Figure 3.6 Confocal microscope SENSOFAR 2300 plu

The measurements were performed using a 20XEPI microscope objective, which was selected according to the resolution features and the requirements of the sample to analyze. Table 3.5 shows the confocal specifications in function of the selected objective.

Table 3.5 Confocal objectives specifications.

Confocal objectives	5XEPI	10XEPI	20XEPI	50XEPI	100XEPI
Working Distance (mm)	23.5	17.3	4.5	1.0	1.0
Numerical aperture	0.15	0.3	0.45	0.8	0.9
Field of View (μm)	2546x1909	1273x955	637x437	253x190	123x92
Spatial Sampling(μm)	3.32	1.66	0.83	0.33	0.17
Maximum Slope	8.5°	14°	21°	42°	51°
Repeatability Rms(nm)	±100	±50	±20	±4	±3
Acquisition time					
Confocal image(s)	0.5	0.5	0.5	0.5	0.5
Topography($\mu\text{m/s}$)	50-800	25-400	12.5-200	2.5-40	2.5-40

3.5.2 Scanning electron microscope.

A scanning electron microscope (SEM) is a type of electron microscope that images a sample by scanning it with a high-energy beam of electrons in a raster

scan pattern. The electrons interact with the atoms that make up the sample producing signals that contain information about the sample's surface topography, composition, and other properties such as electrical conductivity.

Energy-dispersive X-ray spectroscopy (EDS or EDX) is an analytical technique used for the elemental analysis or chemical characterization of a sample. It is a form of X-ray fluorescence spectroscopy which relies on the investigation of a sample through interactions between electromagnetic radiation and matter. It analyzes X-rays emitted by the matter in response to being excited by electrons. Its characterization capabilities are due in large part to the fundamental principle that each element has a unique atomic structure; the X-rays that are emitted are characteristic of an element's atomic structure to be identified uniquely from one another. Compositional analysis of soda-lime glass and morphological data of the fabricated samples were performed with a scanning electron microscope *Zeiss FESEM-ULTRA Plus* (fig. 3.8) [Fesem]. Table 3.6 shows the FESEM specifications.



Figure 3.7 Zeiss FESEM-ULTRA Plus.

Table 3.6 FESEM ULTRA plus specifications

Specifications	FESEM ULTRAPLUS
Resolution (optimal WD)	0.8 nm @ 30 kV (STEM mode) 0.8 nm @ 15 kV 1.6 nm @ 1 kV
Magnification	12 - 1,000,000 x in SE mode / 100 - 1,000,000 x with EsB® detector
Emitter	Thermal field emission type, stability >0.2%/h
Acceleration Voltage	0.02 kV - 30kV
Probe Current	Configuration 1: 4 pA – 20 nA / Configuration 2: 12 pA – 100nA
Detectors	EsB® detector with filtering grid (0 – 1500 V), High efficiency in-lens SE detector, Chamber mounted Everhart-Thornley detector, Integrated AsB® detector
Chamber	330mm (∅) x 270 mm (h), 3 EDS ports 35° TOA, CCD-camera with IR illumination
Vacuum System	Complete dry pumping system composed of Backing Pump, Turbomolecular Pump and Ion Getter Pump, Automatically controlled Quiet Mode to switch off Backing Pump
Charge Compensator	Fully automated and neumatic retractable local gas injector
Specimen Stage	5-Axes Motorised Eucentric Stage X = 130 mm, Y = 130mm, Z = 50mm, T = -3 to 70° R = 360° (continuous) 6-Axes Eucentric Stage X = 100 mm, Y = 100mm, Z = 42 mm, Z' = 13 mm, T = -4 to 70° R = 360° (continuous)
Image Processing	Resolution: Up to 3072 x2304pixel,
Image Display	High end 19" flat panel TFT colour display monitor with SEM image displayed at 1024 x 768 pixel
System Control	SmartSEM®* with Windows®XP.
Space Requirement	Minimum footprint: 1.97 m x 1.73m, Minimum working area: 3.5 m x 5.0 m

3.5.3 Optical microscope.

The diameter and optical images of the marks and elements fabricated by laser ablation of glass materials was performed with an optical microscope *Nikon MM-400* (fig. 3.8)[Microscope]. This instrument was also used for fast visual analysis of

the sample, allowing for their selection / rejection before continuing with the thermal treatment. [MM-400]. Table 3.7 shows the specifications.



Figure 3.8 Optical microscope Nikon MM-400

Table 3.7 Optical microscope MM-400 specifications.

Specifications		MM-400/SLU
Z-axis movement		Manual(dual side coarse/fine focus knob)
MM controller backpack interface		Built-in
Optical head		Y-TB binocular eyepiece tube, LV-TI3 trinocular eyepiece tube, LV-TT2 tilting trinocular eyepiece tube
Z-axis linear scale		Built-in
Eyepiece		CFI10x (Field n° 22), CFI10x CM (Field n° 22)
Objective		CFI60 LU Plan Fluor EPI series, CFI60 LU Plan Fluor BD series, CFI60 LPLAN EPI CR series
Stage		6x4, 4x4, 03L, 2x2
Light source	Diascopic	LED diascopic illuminator (standard), 12V-50W
	Episcopic	White LED illuminator LV-EPI LED, Motorized universal eEPI-illuminator LV-U EPI2A, Universal Illuminator with focusing Aid LV-U EPI FA
Max. workpiece height		150mm

3.5.4 UV/VIS Spectrophotometer.

The optical transmission of glass materials and the optical elements fabricated were analyzed with a UV/VIS spectrophotometer *PerkinElmer Lambda 25* covering

a spectral range between 200 and 1100 (fig 3.9) [Spectrophotometer]. Table 3.8 shows the *UV/VIS Perkin Elmer Spectrophotometer* specifications.

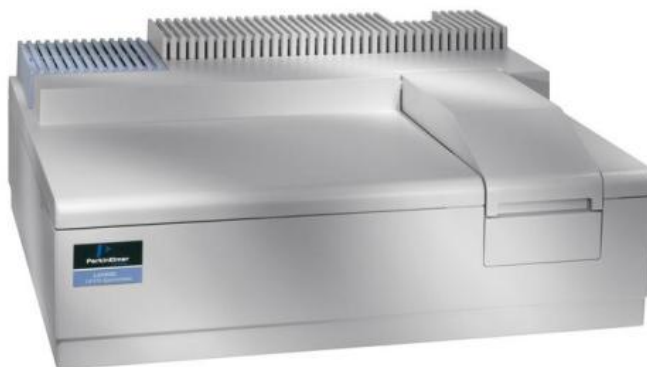


Figure 3.9 UV/VIS Perkin Elmer Spectrophotometer.

Table 3.8 UV-VIS-IR Perkin Elmer Spectrophotometer specifications.

Specifications	Lambda 25
Wavelength range	190-1100 nm
Bandwidth	1 nm
Stray light	At 220 nm (NaI) < 0.01%T At 340 nm (NaNO ₂) < 0.01%T At 370 nm (NaNO ₂) < 0.01%T At 200nm (KCl) < 0.01%T
Wavelength accuracy	At D ₂ Peak (656.1nm) ± 0.1nm
Wavelength reproducibility	10 measurements at 656.1nm ± 0.05 nm
Photometric accuracy	At 1 A using NIST 930D filter ± 0.001 A At 2 A using NIST 1930D filter ± 0.005 A Potassium dichromate ± 0.010 A
Photometric reproducibility	Maximum deviation of 10 measurements at 1 A < 0.001 A
Photometric stability	Stability at 1 A, at 500nm < 0.00015 A with 2 sec response time A/hour
Photometric noise at 500 nm(RMS)	Noise 500nm/0 A RMS Slit 1 nm < 0.00005 A
Baseline flatness	Slit 1 nm ±0.001 A

3.5.5 Beam profiler

The irradiance distribution of the laser beam and the microlens spot size and irradiance at focus were analyzed using a beam profiler BP-109UV, which is a high-precision instrument that can analyze the power distribution of laser beams with diameters from 10 μm to 9 mm. Figure 3.10 shows the beam profiler [Beam Profiler]. Table 3.9 shows the Beam profiler BP-109UV specifications.

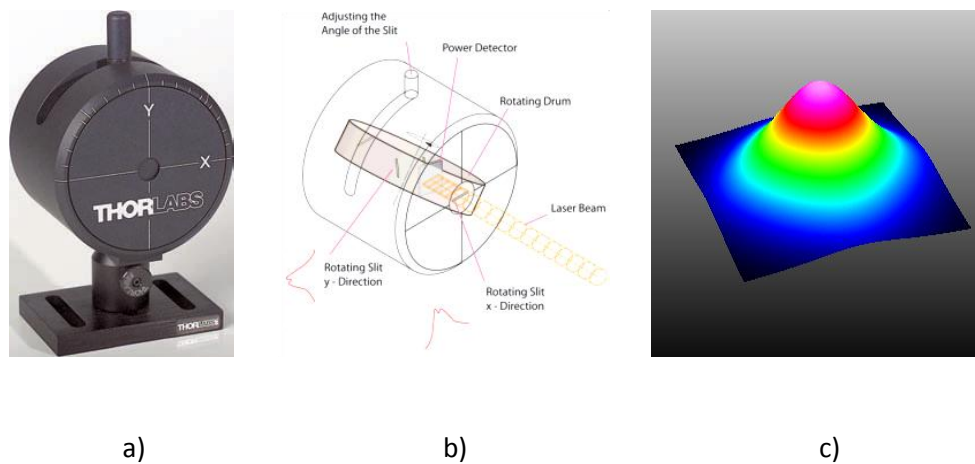


Figure 3.10 a) BP-104 beam profiler image, b) beam profiler internal mechanism and c) 3D profile of irradiance distribution provided by the beam profiler.

Table 3.9 Beam profiler BP-109 UV-IR specifications.

Specifications	BP-104 UV-IR
Wavelength Range (nm)	200 - 1100
Detector Type	Si - UV Enhanced
Aperture Diameter	4 mm
Scan Method	Scanning Slits
Slit Size	2.5 μm
Min Beam Diameter	10 μm
Max Beam Diameter	4 mm
Scan Rate	1.0 - 20.0 per s (continuously variable)
Sampling Resolution	0.5 - 38 μm (depending on scan rate)

Power Range	10 nW - 10 W (depending on beam diameter and model)
Amplifier Bandwidth	10 to 150 kHz in 10 kHz Steps (@ -1 dB)
Sample Frequency	0.0625 - 1.0 MHz
Dynamic Range	72 dB (Amplifier Switchable)
Signal Digitization	16 bit
Head Size	∅ 80 mm x 60 mm (including rotation mount)
Minimum Pulse Rate	10 Hz (300 kHz if using the M ² Option)
Software	
Displayed Parameters/Features	X-Y-Profile, Centroid Position, Peak Position, Pseudo 3D Profile, Beam Width Clip Level/Second Moment (4σ), Gaussian Fit Applicable, Colored Pass/Fail Test
Compliant to Norm	ISO 11146 (Beam Widths, Divergence Angle and Beam Propagation Factor)
General System Requirements	Windows™ 2000/XP/Vista or later, USB2.0 port recommended, 120 MB HD, 512 MB RAM
M² Analysis System	
Compatible M² Options	BP1M2-xx Series, M2SET-xxx Series
Compliant to Norm	ISO 11146
Measured Parameters**	M ² , Waist Width, Waist Position, Rayleigh Length, Divergence, Beam Pointing, Waist Asymmetry, Astigmatism

CHAPTER 4

ABLATIVE PROCESS OF SODA-LIME GLASS

This chapter presents an overview of the ablative process on soda-lime glass. The influence of impurities, the role of roughness and defects of the surface and pulse width are investigated. The beam diameter, the ablation threshold and the debris deposition are also determined in this chapter. Additionally, it is presented the enhancements mechanism of the ablative process using a thin film layer deposited over the glass.

4.1 Introduction

In transparent materials, the absorption of radiation at near IR wavelengths comes from different mechanisms (as saw in chapter 2). Impurities in the glass can transfer energy from the laser to the host material. Avalanche effects, where free electrons are further energized using long pulses, also result in effective coupling of light to the material. When the laser field strength is very high, as in the case of ultrashort pulse laser matter interaction, bound electrons of the transparent material can be directly ionized through multi-photon absorption, a bound electron can be lifted from the valence band to the conduction band, by simultaneously absorbing a single or multiple photons in the laser pulse.

In the particular case of soda-lime glass for IR nanosecond laser, the bound valence electrons have an ionization potential or bandgap greater than the laser photon energy. In glass, as in any real material there are always some free electrons presented, the laser radiation can interact with the free electrons and cause these electrons to move through the solid rapidly. If the free electron is moving rapidly enough, it may knock an electron away from an atom in the solid. This ejected electron (excited) can move freely through the solid and excite other electrons in the same way, in a process that leads to an avalanche effect (see section 2.2 of chapter 2). When enough bound electrons are ionized by this avalanche process, plasma with a critical density is created and the transparency of the material is broken and becomes absorbing. In the particular case of soda-lime glass, these seed electrons could come from metallic impurities, which are incorporated during the fabrication process. Figure 4.1 presents a diagram of the mechanism leading to ablation process in soda-lime glass.

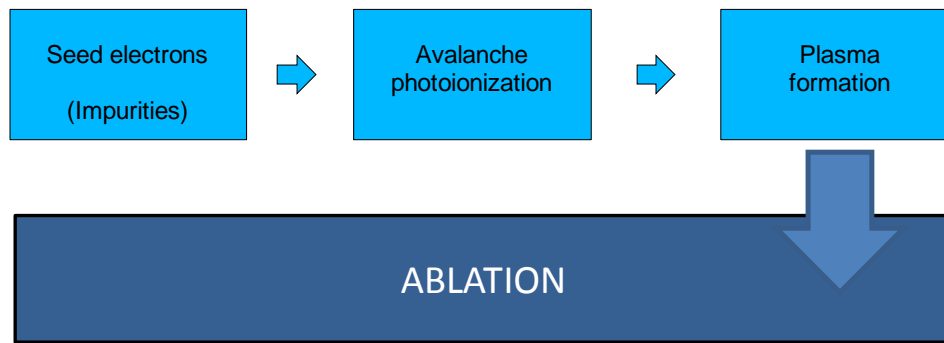


Figure 4.1 Diagram of the mechanism leading to the ablation process on soda-lime glass.

In this chapter we are going to analyze the influence of impurities presented in soda-lime glass, the role of roughness, pulse width and defects at surfaces that acts like scattering center for the incoming light making possible the light to interact with the surface of transparent materials leading to an enhancement of ablative process.

4.2 Role of Impurities.

The first approach to identify the role of impurities comes from the study of the chemical composition of soda-lime glass. Different percentage of impurities on each side of the soda-lime glass was identified using EDX analysis (section 3.1 of chapter 3). In order to evaluate the influence of these impurities as seed electrons for initiating the ablation process, the ablation threshold was identified independently over each side of the soda-lime glass. The laser used was an IR nanosecond laser operating at 1064nm. The ablations thresholds identified correspond to 112 J/cm² for the side A (with Sn impurities) and 920 J/cm² in side B (with non Sn impurities), which means a reduction nearly of one order of magnitude. Figures 4.1a and 4.1b show the mark obtained after firing one pulse over the soda-lime glass on sides B and A respectively, with the laser power corresponding to the ablation threshold of side A.

Figure 4.1c and 4.1d show the aspect of the soda-lime glass after fabricating one line, again on sides B and A respectively. The laser parameters used were 2W, 3 kHz and 20 mm/s at a laser fluence of 112 J/cm^2

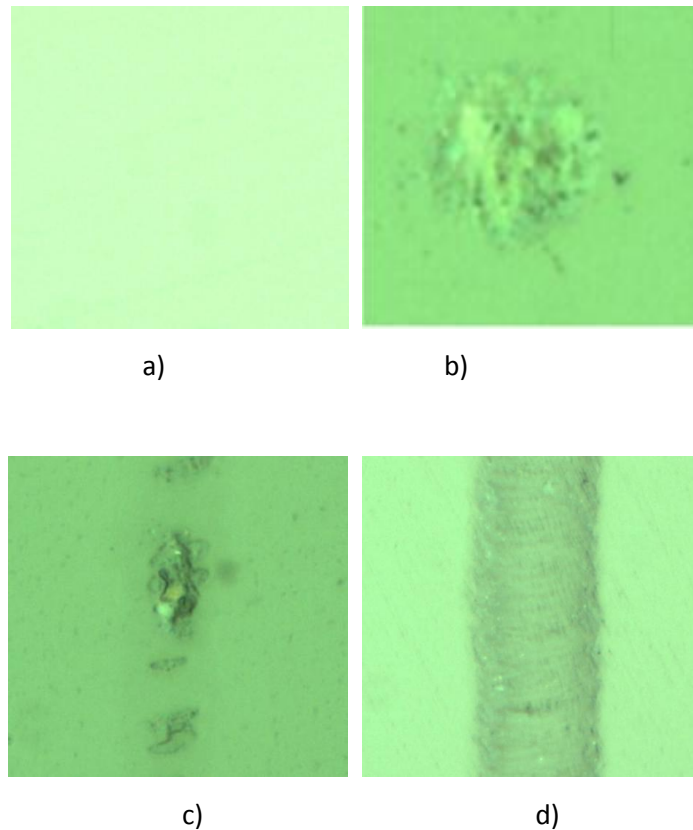


Figure 4.1 Images at the surface of soda-lime glass after firing one pulse over a) non Sn side, b) side with Sn; and a train of pulses over c) non Sn side and d) Sn side. The energy of the incident laser pulse was 0.2 mJ. The overlap shots per area for c) and b) were 20 pulses.

In figure 4.1 we clearly observe that the presence of the Sn impurities is crucial in the ablation process. On the side of the glass without the impurities, the ablative process cannot be initiated for the same laser work condition (see figs. 4.1a and c). On the other hand, fig.4.1b and c, show the mark obtained by the laser ablation on the side with presence of Sn.

In addition, the distribution of impurities on the glass was analyzed. To this purpose and array of holes was fabricated on soda-lime glass over the side with Sn impurities. Again, the laser used was an IR Nanosecond laser operating at 1064nm with pulse duration of 20 ns and 2.5 W, 1 kHz and 100 mm/s. Figure 4.2 shows a confocal image of the array of holes fabricated on glass.

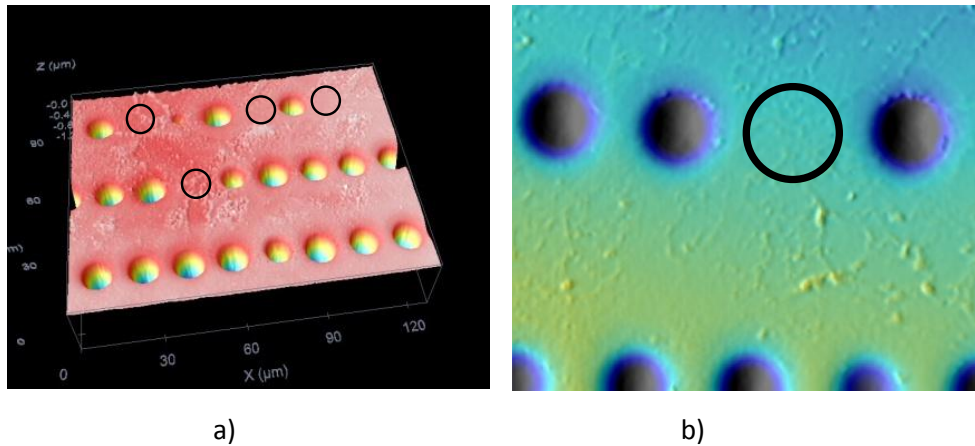


Figure 4.2. 3D confocal images of an array of holes machined on soda-lime glass (λ 1064nm, pulse duration of 20 ns, 2.5 W, 1 kHz and 100 mm/s. Black circles represent places where the pulse laser had impinged but no mark was obtained.

As it can be appreciated in figure 4.2, not all the holes were ablated onto the glass. Black circles represent places where the pulse laser had impinged but no mark was obtained, which correspond to areas of the glass where there are not presence of Sn.

Additionally, a study varying the power but maintaining fixed the repetition rate at 1 kHz and the scan speed at 100mm/s was done. Figure 4.3 shows the arrays of holes fabricated at different fluences.

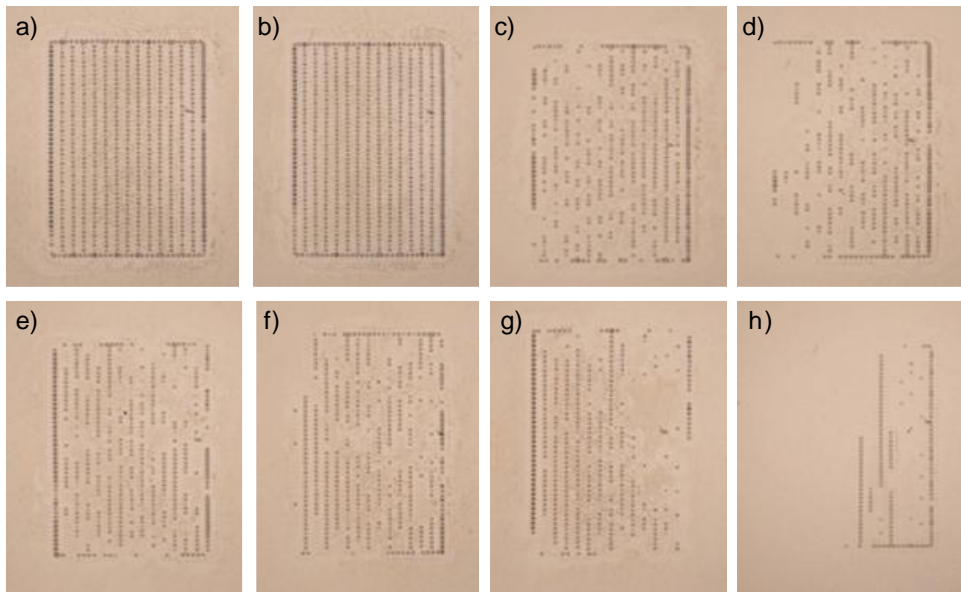


Figure 4.3 Images of an array of holes machined on soda-lime glass at 1 kHz, scan speed 100 mm/s and different fluences, a) 130 J/cm^2 , b) 126 J/cm^2 , c) 112 J/cm^2 , d) 109 J/cm^2 e) 103 J/cm^2 and f) 100 J/cm^2

As it can be appreciate on figure 4.3, which is in agreement with figure 4.2, each point at figures is the result of the ablation of one pulse shot at the surface of the glass.

As the energy per pulse is equal for all the points, the places where no holes appears means that the interaction between laser beam and substrate is difference on points at the surfaces of the glass.

Taking into account that we have demonstrated the role of impurities over the ablation process of glass and, assuming that the impurities incorporation is the result of having the glass floating in a Sn bath during the fabrication process, we can relate that the non-uniform distribution of impurities in the glass leads to differences on the ablation threshold and, as presented in figures 4.2 and 4.3 to non-uniform distribution of the holes.

4.3 Role of surface Roughness.

It has been reported through measurements of the polarization of light reflected from particulate surfaces that there is also a component of light reflected that has not been transmitted but has only interacted with the constituent particles [Dollfus1985]. We will prove the following hypothesis: the incoming light can be scattered by microscopic surface roughness and the defects make possible that light interacts with the surface of transparent materials, which leads to an enhanced ablative process.

After testing some samples it was realized that the roughness has a very important role in the mechanism of the process. In order to demonstrate it, some experiments were performed over unprocessed glass and a rough glass surface pre-treated in a polishing machine. The polishing process creates a surface with a Roughness Average (Ra) of 554 nm (Fig. 4.4).

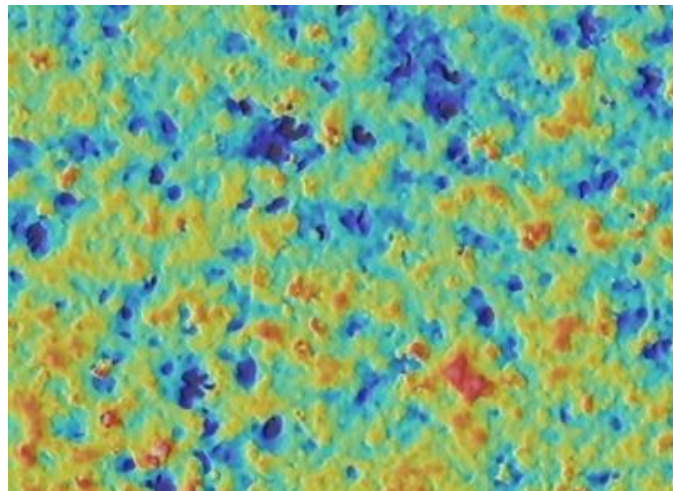


Figure 4.4 Confocal image of roughness generated at the surface of glass. It is found to consist of craters machined in the glass in the range of diameter 100-400 nm and height 100-600 nm.

Over the pretreated glass, it was fabricated a line at a fluence (15.66 J/cm^2) below the ablation threshold of soda-lime glass for non Sn side. Figure 4.5 shows a 3D confocal image and a profile of a line fabricated over the pre-treated glass. The laser used was an IR Nanosecond laser operating at 1064 nm with pulse duration of 20 ns .

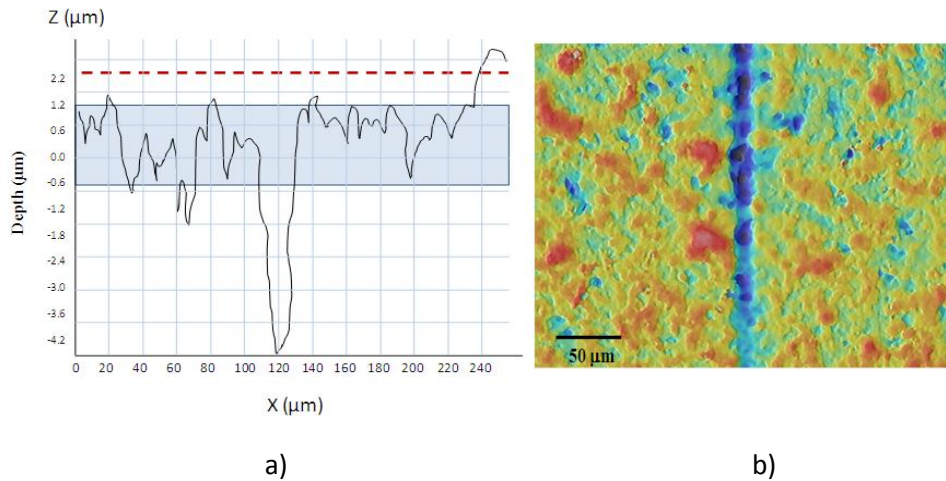


Figure 4.5 a) Profile and b) Confocal top view image of one line fabricated at surface of structured glass, the blue square in figure a) shows the topography of the roughness generated at glass surface with the polishing machine. The laser parameters were 5 W , 10 kHz , scan speed of 100 mm/s .

As it can be appreciate in figure 4.5, it was possible to fabricate a line on the top surface of a pre-treated glass at fluence of 15.66 J/cm^2 , which is two orders of magnitude below the ablation threshold for soda-lime glass with no Sn impurities.

The results obtained show that the roughness of the glass surface is significant for reducing the ablation threshold. Based on this experiment, we fabricate a line over pre-treated surface by applying various laser passes.

Figure 4.6 shows the depth as a function of number of passes over a pre-treated glass substrate.

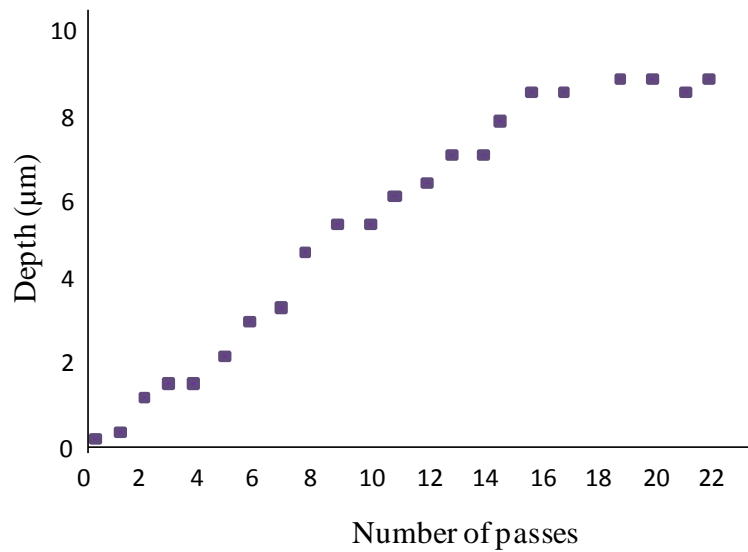


Figure 4.6 Depth as a function of number of passes for roughened glass substrate.

From the slope obtained on figure 4.6 it can be observed the evolution with the number of passes. The depth of the mark increases with the number of passes made with the laser, reaching a maximum value of depth $10\mu\text{m}$ after 18 pass, after this value, an increasing of the laser pass does not becomes in a increasing of the mark depth. That behavior is due to the fact that the ablation plume has not energy enough to take out the material detached on the ablation process.

4.4 Influence of pulse width.

The influence of pulse width was analyzed in the range of IR wavelength for femtosecond, picosecond and nanosecond lasers. Figure 4.7 shows the morphology obtained for each pulse width at the fluence threshold.

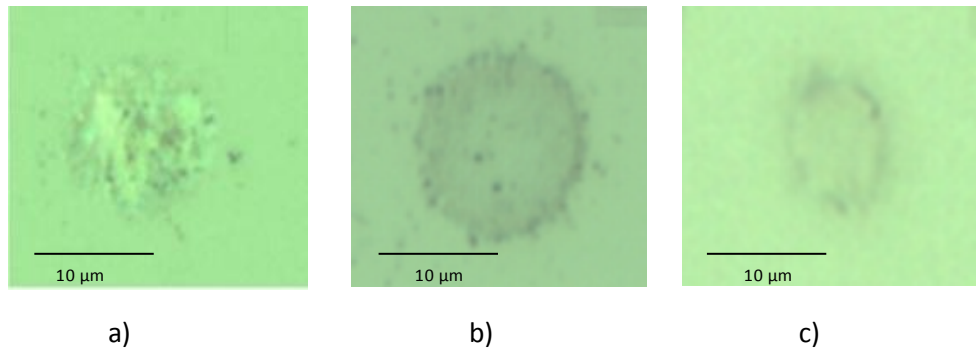


Figure 4.7 Morphology of the mark created after one laser shot on soda-lime glass for a) nanosecond laser, b) picosecond laser and c) femtosecond laser.

As it can be appreciated in figure 4.7, the morphology of the mark is different for each pulse width, which is expected to be related with the different mechanism involved in the ablation process. Since the heating time is equivalent to the pulse width, different interaction times are involved in transferring the energy from the laser to the lattice of the material. As the laser energy is principally absorbed by the electrons, the electron-phonon/lattice coupling time is in the range of 1 picosecond and the overall relaxation time is in the range of 200 picoseconds.

It is expected that when using nanosecond pulse width, the laser energy is absorbed while these interactions take place; it is the accumulative or thermal effects which will lead to ablation. When using a femtosecond pulse width, the interaction time of laser pulses with the materials is less than the electron-phonon interaction and relaxation times, so the electrons have time to absorb, transfer and relax before the next laser pulse comes; here the damage may accumulate in the material but the process will be less thermal [Krzysztof2005, Shinonaga2009, Rudolph1999, Stuart1996].

In order to get more useful data for a better understanding of the ablative process, investigations and comparison of several glasses (borosilicate, fused

silica, sapphire) with the results obtained for soda-lime glass were done. Figure 4.8, shows the ablation threshold data obtained for different glass samples for nanosecond, picosecond and femtosecond laser pulses.

	0	100	1000 J/cm ²
Nanosecond			⇒ Fused silica ⇒ Sapphire 954.86 Borosilicate 923.23 Soda-lime (Side without Sn) 112.68 Soda-lime (Side with Sn)
Picosecond	9.40 Borosilicate	11.02 Fused silica 9.54 Soda-lime (Side without Sn) 8.57 Soda-lime (Side with Sn)	⇒ Sapphire
Femtosecond	3.60 Fused silica 4.18 Sapphire 2.98 Borosilicate 2.90 Soda-lime (Side without Sn) 1.98 Soda-lime (Side with Sn)		

Figure 4.8 Ablation threshold data obtained for different glass samples, for nanosecond, picoseconds and femtosecond laser pulses.

In figure 4.8 it can be appreciate that the best result in terms of energy reduction is obtained for nanosecond pulses in the case of soda-lime glass with Sn impurities, which reduces the ablation threshold by one order of magnitude. This enhancement is very important since most of the glasses do not absorb IR wavelengths and most of the micromachining nanosecond IR lasers do not have enough power for machining the glass, or work just in the limits, so the important reduction in terms of energy that offer the ablation through the impurities is of crucial importance. In case of picoseconds, the ablation threshold is one order of magnitude below than the ablation threshold of nanosecond laser for all the glasses, excluding sapphire. Femtosecond pulse width presents the lowest ablation threshold, obtaining a reduction of two orders of magnitude. For

picosecond and femtosecond no significant reduction on the ablation threshold was observed for the soda-lime glass with Sn impurities, compared with Sn without impurities. It can be explained by the interaction mechanism of laser pulse and glass and its pulse width dependence. On glass materials, the absorption of light, which leads to the ablation, comes from a photophysical response, which involves non-linear and linear effects. The pulse duration and the material response time are important factors that will determine the kind of mechanism that leads to ablation of material.

Whit long pulse (nanosecond) laser processing, the dominant process involved is the heating of the target material through the liquid phase to the vapor phase, resulting in expansion and expulsion of the desired target material. The Sn impurities incorporated in soda-lime glass acts as seed electrons for initiating the avalanche ionization and the ablation process. The duration of the pulses allows for a long avalanche which results in a enhancement mechanism of the ablation process with a reduction of one order of magnitude on the ablation threshold of soda-lime glass.

On the other hand, when the laser field strength is very high, the bounded electrons of the transparent material can be directly ionized through multi-photon absorption. It results in a direct vaporization of the target surface. In this case, the soda-lime glass absorbs the incident laser energy preferable due to multiphoton ionization with low contribution of the electron avalanche ionization due to the short irradiation interval. Therefore the impurities in this case do not present any significant improvement, or at least it is not appreciated from our experiments.

4.5 Laser ablation parameters optimization.

Taking into account the results obtained in section 4.1 and 4.2, we selected the soda-lime glass as suitable material for fabricating microlens and microchannels with applications on micro-optics and microfluidics at low cost. The optimization of laser parameter comes from analyzing the ablation threshold, the diameter of the mark generated with the laser beam on the soda-lime glass and the pulse overlap, which determine number of pulse per area. In addition, the morphology of the mark generated at surface during laser ablation and the analysis of debris deposition will help us to determine the best laser parameters needed for fabricating different devices. To this purpose, it was investigated, for an identified threshold fluence and beam diameter, the morphology of damage created at the surface of the glass, using these data for optimizing the designing parameters of the posterior fabrication of micro-optics and microfluidics devices.

4.5.1 Ablation threshold and beam diameter

A simple theoretical value for a single-shot threshold fluence is found by assuming that the light is absorbed according to Beers Law and ablation occurs when the energy per unit volume exceeds the energy necessary for the material to undergo heating, melting and evaporation.

In terms of energy the ablation threshold F_{th} was determined using the Eq. (4.1) [Ben-Yakar2004],

$$F_{th} = \frac{2E_{th}}{\pi \omega_0^2} \quad (4.1)$$

Where E_{th} is the energy per pulse at the onset of ablation and ω_0 is the radius at $1/e^2$ of the Gaussian laser beam.

The beam spot size, which is required for determining the fluence threshold, was determined using the squared diameter (D^2) of the ablated areas [Ben-Yakar2004]. The D^2 of the ablated areas is plotted as a function of the peak fluence of the laser F_{peak} . The slope of the linear fit permit us to know the beam radius at the surface, ω_0 .

$$D^2 = 2\omega_0^2 \ln\left(\frac{F_{peak}}{F_{th}}\right) \quad (4.2)$$

In order to estimate the fluence, the precise knowledge of ω_0 is required. Since it is easier to measure the energy per pulse, E_{pulse} , experimentally, we replace the fluence ratio in Eq. (4.3) by the ratio of the pulse energies, yielding:

$$D^2 = 2\omega_0^2 \ln\left(\frac{E_{pulse}}{E_{th}}\right) \quad (4.3)$$

Because the measured Gaussian spot size on the surface is not necessarily equal to the calculated spot size at the focal point of the objective, D^2 calculation is more realistic than theoretical calculations of beam spot sizes.

Figure 4.9 shows this linear relation between the squared diameter and the natural logarithm of the average laser fluence in our measurements for the nanosecond laser. A value of $21.65 \mu\text{m}$ was obtained.

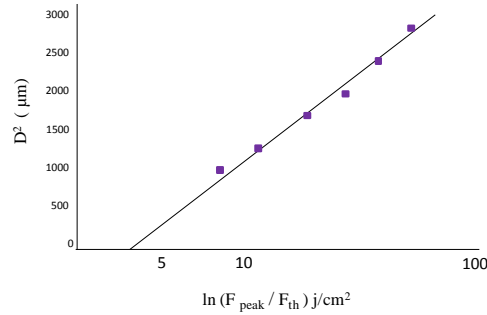


Figure 4.9 Linear relations between the squared diameter and the natural logarithm of the average laser fluence in our measurements for nanosecond.

4.5.2 Mark analysis and pulse overlap.

For determining the size of the mark made by the laser beam in the glass substrate, a crater was made in the glass after firing one shot at a fluence of 112 J/cm^2 . The size of the crater was analyzed with a confocal microscope obtaining $15 \mu\text{m}$ width and $8 \mu\text{m}$ height for soda-lime glass. Figure 4.10 shows the morphological data, height and diameter, of the mark obtained after one laser shot on soda-lime glass. These data also provide the useful information for calculating the pulses overlap, and so the number of pulses per area.

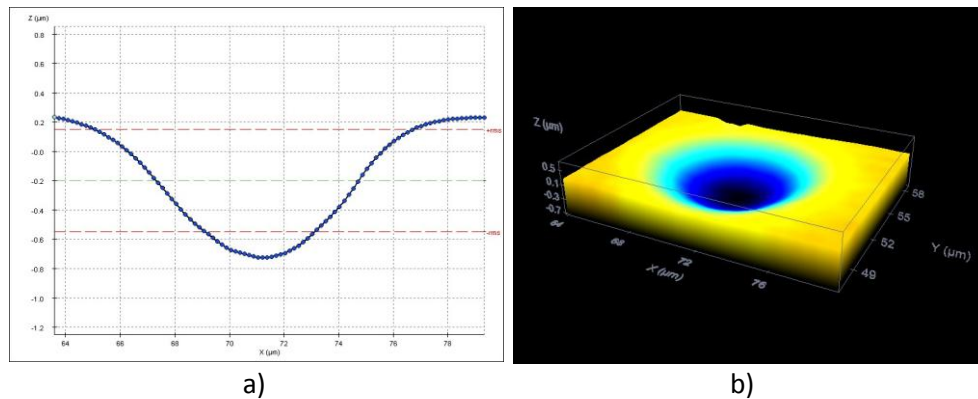


Figure 4.10 a) Profile and b) confocal image of a crater made on glass substrate by one shot of the laser beam.

The main morphological parameters after laser ablation, such as depth, width and roughness for different number of pulses have been analyzed using a confocal microscope SENSOFAR 2300 PL μ and an optical microscope Nikon MM-400.

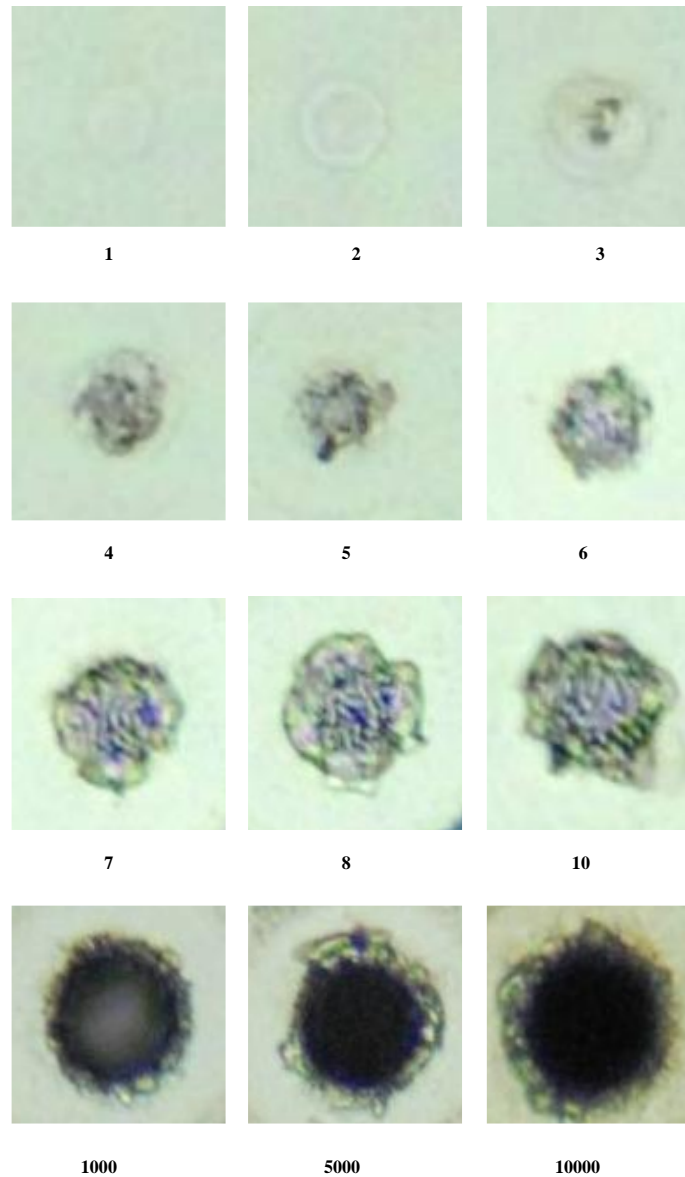
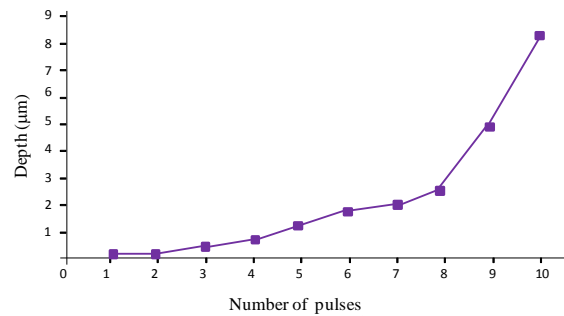
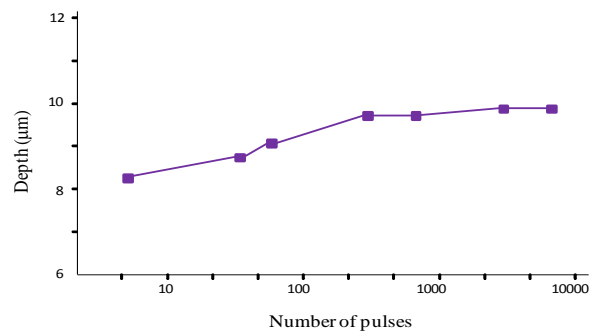


Figure 4.11 Evolution of damage at surface of soda-lime glass with the number of pulses.

Figure 4.11 shows images of the evolution of the damage at the substrate surface with the number of pulses. Measurements of the depth, roughness and diameter of the ablated holes can also provide important information about the material response to the nanosecond laser. This is illustrated in figure 4.12 and 4.13.



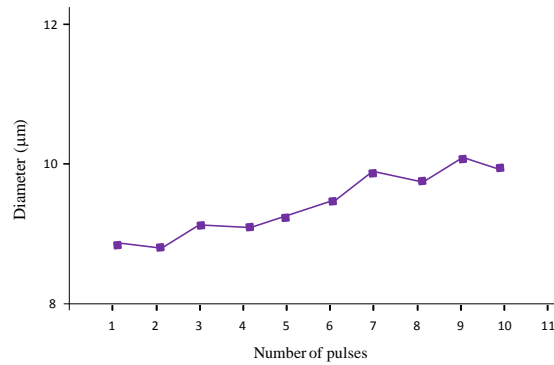
a)



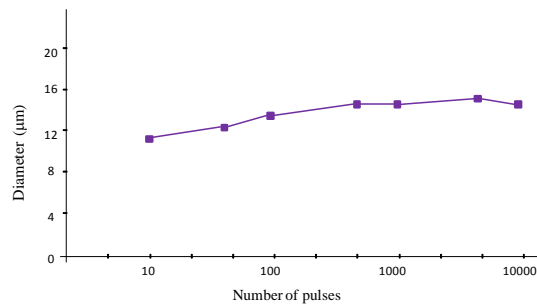
b)

Figure 4.12 Evolution of depth vs number of pulses for a) 1-10 pulses and b) 10-10000 pulses).

As it can be appreciate in figure 4.12a , the depth increases with the first pulses, reaching a depth value of 8 microns after 10 pulses, however after 10 pulses (figure 4.12b), the depth increase slowly, varying only 2 microns after 500 pulses and maintain almost constant till 10000 pulses. That behavior is due to the fact that the ablation plume has not energy enough to take out the material detached on the ablation process.



a)



b)

Figure 4.13 Evolution for diameter versus number of pulses a) 1-10 pulses and b) 10-10000 pulses).

From the slope obtained on figure 4.13 it can be observed the evolution of diameter with the number of pulses. The mark diameter increases slowly with the number of pulses, reaching a maximum value of depth $10\mu\text{m}$ after 500 pulses, after this value (fig. 4.13b), an increasing of the number of pulses does not become in a increasing of the mark diameter.

For fabricating a microchannel on glass, the optimization of the pulse overlap, which determines the pulse per area, is crucial to obtain high quality scribes. If the pulse overlap is too high then it will be significant cracking due to the stress built up from too much heat deposited in a small area. The pulse overlap, O_d , is calculated from the following relation [Thawari2005].

$$O_d = \left(1 - \frac{v}{2\omega_0 f}\right) \quad (4.4)$$

where v is the galvo scanner speed, $2\omega_0$ is the focused spot diameter and f is the laser repetition rate.

The first experimental approach for obtaining uniform channels was checked at different scan speed for getting the optimal pulses overlapping (Fig. 4.14). It was used the same laser parameters (10 kHz, 8W) for fabricating all the lines varying only the scan speed.

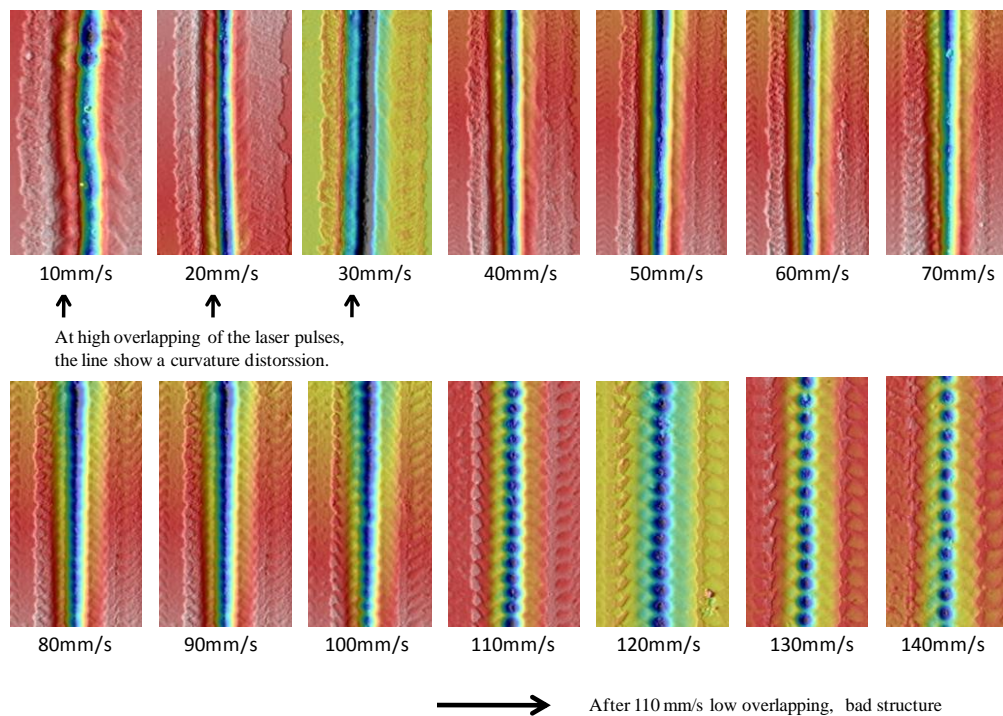


Figure 4.14 Uniformity of channels fabricated at different speeds.

As it can be appreciate in figure 4.14, the best results were obtained for the lines fabricated in the range of 40-100 mm/s. At high speed the low overlapping of the

pulses make irregular the line (the surface profile for 150 mm/s shows this structure, created for each pulse). At low speed the high overlapping creates a distortion on the lines and increases the roughness average (Ra) too.

To corroborate these results, it was analyzed the quality of the lines in terms of roughness by measuring the Ra at the bottom of the channels. Table 4.1 shows the results.

Table 4.1 Ra values obtained for different scan speeds.

Scand speed	Roughness
10 mm/s	176.86 nm
40 mm/s	56.16 nm
50 mm/s	54.40 nm
60 mm/s	62.14 nm
100 mm/s	74.83 nm
150 mm/s	174 nm

We can observe that the best results are obtained with scan speeds of 40, 50 and 60 mm/s.

4.5.3 Debris deposition.

Since the debris generated change the Ra and are crucial for obtaining good micro-optical and micro-fluidics elements, a study of debris deposition near to the laser machined channel was undertaken at mark depth of 4.5 μm , which is the result of fabricating the line at a laser fluence above the ablation threshold of glass. That ensures enough energy to propel the debris far from the ablation region and so, let us undertake the investigations of debris deposition at considerable distance from the center of the line. The results are shown in figures 4.15

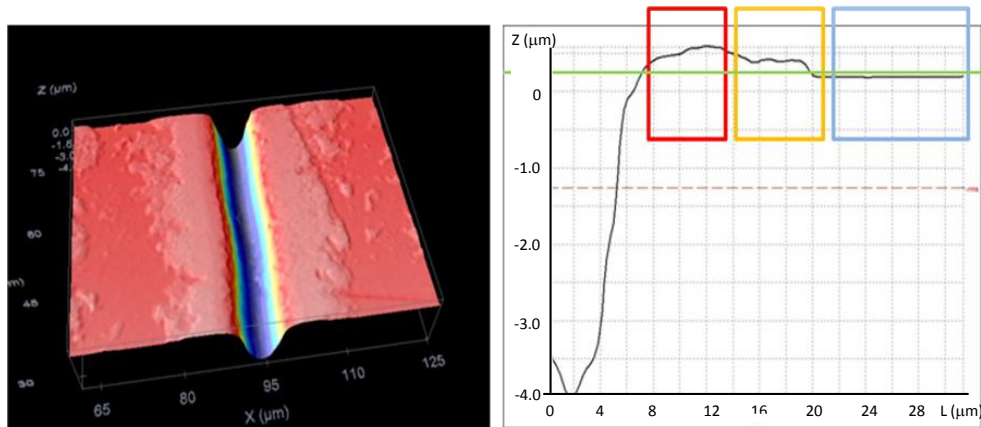


Figure 4.15 a) confocal image of a 4.5 μm channel and b) half transverse profile of a channel with debris deposition at different distances from the center represented by different regions using colored squares.

In figure 4.15, square 1 (blue) shows the portion of the surface measured for determining the roughness average over the glass without debris. The roughness is estimated to be 6.2 nm for a distance greater than 20 microns. Square 2 (yellow) shows the portion of the surface measured for determining the roughness average over the glass with debris, far from the line. The average roughness is estimated to be 12.3 nm in the region defined by a distance from 14 to 20 microns from the centre of the laser ablated line. Square 3 (red) shows the portion of the surface measured for determining the roughness average over the glass with debris near the line. The average roughness is estimated to be 12.3 nm in the region defined by a distance from 8 to 14 microns from the centre of the laser ablated line. The line (green) across the profile shows the difference on depth of the glass surface and the part in which the debris was deposited after ablation. From this data we can obtain information about the quantity of debris removed and the deposition when we fabricate shallow and deep channels. In addition, it was appreciated the need of use a cleaning process after laser exposure, that involves a chemical etching process (see section 5.4 of Chapter 5).

4.6 Enhancement of the ablative process using a thin absorber layer.

Considering laser-matter interaction, an attempt is made to identify the mechanism that leads to the ablation of the transparent materials using a thin film coating at different pulse durations, so three factors affecting the ablation region were identified on literature and considered in this work. The first one is related with **structural defects** in the aluminum thin film (roughness) which enhances absorption in dielectric. The second one is related with **impurity incorporation** which increases the absorption of laser energy, during later part of the pulse or for subsequent pulse. The last one is related to the **charge transfer** from the thin film into dielectric which leads to avalanche absorption mechanism. The use of a solid thin film as an absorber layer of the laser irradiation was used in this work to aid the ablation process. To this purpose a 15 nm thin aluminum layer was deposited over different glass materials using a physical vapour deposition machine (Balzers BAE 250 coating system). All of these factors are related with the coupling of light at the glass surface and the transmission of energy from the laser to the aluminum that interacts with the glass. Some experiments were developed for trying to get the first approach to our hypothesis. Figure 4.16 shows a diagram of the process involved in these hypotheses.

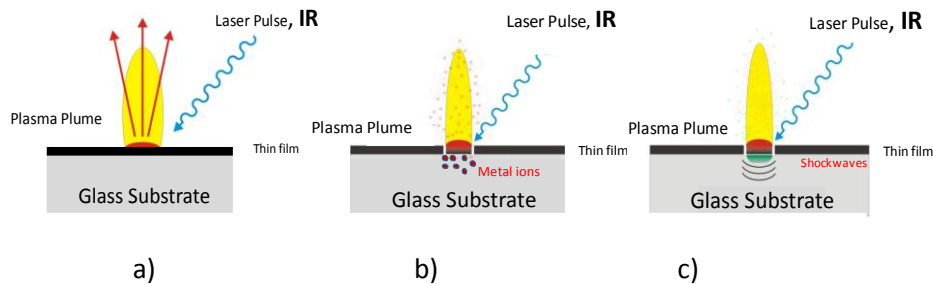


Figure 4.16 Sketch of the mechanism that leads to the laser ablation of glass using the aluminum thin film, a) structural defects (roughness), b) impurity incorporation and c) charge transfer

Figure 4.17, shows the ablation threshold data obtained for coated and uncoated different glass samples, for nanosecond, picosecond and femtosecond laser pulses.

	0	100	1000	J/cm ²
Nanosecond	33.62 Fused silica 27.63 Sapphire 9.34 Borosilicate 7.32 Soda-lime (Side without Sn) 6.96 Soda-lime (Side with Sn)			⇒ Fused silica ⇒ Sapphire 954.85 Borosilicate 923.23 Soda-lime (Side without Sn)
		112.68 Soda-lime (Side with Sn)		
Picosecond	9.58 Sapphire 9.96 Fused silica 9.40 Borosilicate 9.46 Soda-lime (Side without Sn) 7.05 Soda-lime (Side with Sn)	11.02 Fused silica 10.53 Borosilicate 9.54 Soda-lime (Side without Sn) 8.57 Soda-lime (Side with Sn)		⇒ Sapphire
Femtosecond	3.60 Fused silica 4.18 Sapphire 2.98 Borosilicate 2.90 Soda-lime (Side without Sn) 1.98 Soda-lime (Side with Sn)	5.12 Fused silica 6.34 Sapphire 8.12 Borosilicate 4.21 Soda-lime (Side without Sn) 4.52 Soda-lime (Side with Sn)		

Figure 4.17 Ablation thresholds for different glass materials at different pulse duration. Black text relates the ablation threshold for unprocessed glass and blue text refers to the ablation threshold for glass covered with the absorber layer.

It is clear that the best result is obtained for nanosecond pulses. In this case the ablation threshold is reduced by two orders of magnitude for borosilicate, fused silica and sapphire and one order of magnitude for soda-lime glass. In case of picosecond pulses it is slightly reduced in some glasses, less in borosilicate in which the overall value for ablation threshold is a little bit higher. For femtosecond pulses there is no significant reduction in the ablation threshold and the enhancement is minor.

The best enhancement in terms of energy reduction was obtained for nanosecond laser and the glass covered with the aluminum layer, presenting low ablation threshold, which is very important since most of the glasses do not absorb IR wavelengths well and so, in order to ablate the glass, it is necessary to use high

energy levels, which is provided by femtosecond and picosecond lasers. Besides, most of the micromachining nanosecond IR lasers do not have enough power for machining the glass, or work just in the limits, so the important reduction in terms of energy that offer this technique is very useful for machining the glass. Although, the picosecond and femtosecond pulses do not present important results regarding energy reduction, the data obtained is very useful for developing the understanding of the ablation process developed in this work, which will be analyzed in next section.

4.6.1 Factors affecting ablation region: Role of roughness

The incoming light can be scattered by microscopic surface roughness and defects, this makes it possible for the light to interact at the surface of transparent materials which leads to an enhanced ablative process. After testing some samples we can assert that the roughness has a very important role in the mechanism of the process. In order to probe that, a line was fabricated over an absorptive aluminum layer and a glass surface pre-treated in a polishing machine for generating a rough surface. The roughness average (*Ra*) of aluminum layer was estimated to be 30 nm, the roughness average of pre-treated glass surface, 600 nm and the *Ra* of soda-lime unprocessed glass was 2.1 nm. The objective is to relate the size of the particles of aluminum layer with the size of the particles created in the glass using the polishing process and so related both with roughness. The size of aluminum nanoparticles was determined with a scanning electron microscope, obtaining values diameter around 20 nm for aluminum. The polishing treatment generates structures at surface of glass in the range of diameter 100-300nm and height 100-600 nm. The morphological data is shown in figure 4.18 and 4.19 respectively.

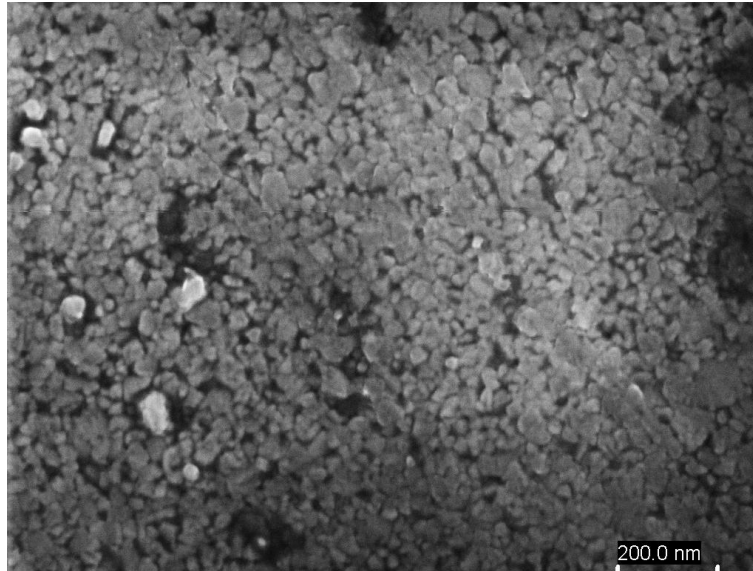


Figure 4.18 SEM image of aluminum layer; it is found to consist of an aggregate of nanoparticles for the 15nm – 40nm thickness range used in this study.

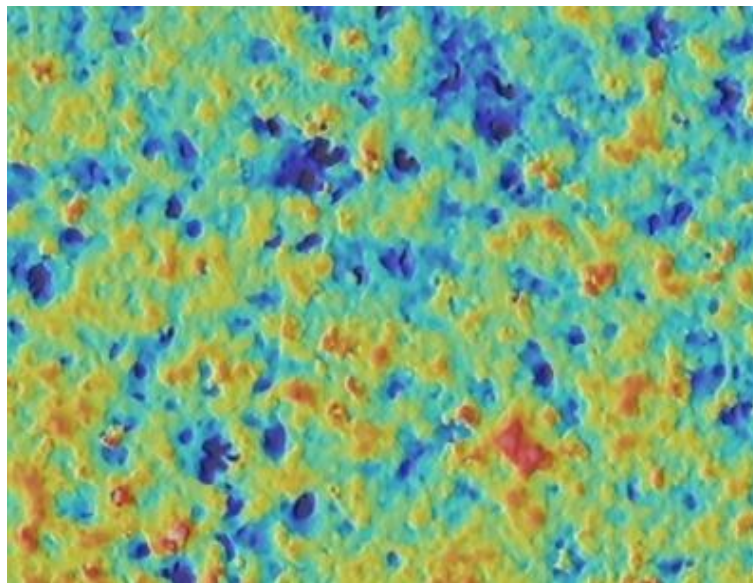


Figure 4.19 Confocal image of roughness generated at the glass surface. It is found to consist of craters from polishing of the glass in the range of diameter 100-300 nm and height 100-600 nm.

The line was fabricated below the ablation threshold for uncoated glass 15.66 J/cm^2 , the results obtained demonstrate that both the aluminum layer and the roughened glass surface are significant for reducing the ablation threshold. In order to get more data, the depth of the line as a function of number of passes is plotted in figure 4.20

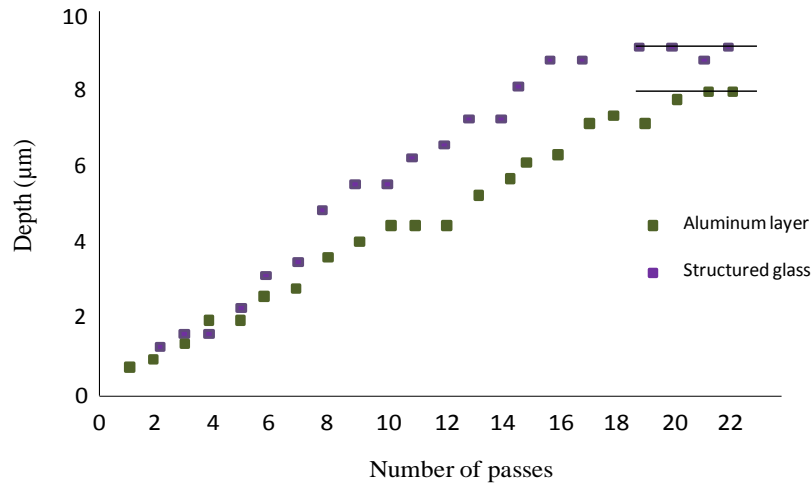


Figure 4.20 Depth as a function of number of passes for (red line) glass covered with aluminum layer and (green line) roughened glass substrate using IR laser parameters, pulse width of 20ns, repetition rate 1 kHz and fluence 15.66 J/cm^2 .

The data suggests that the evolution with the number of pulses saturates after a specific depth (10 µm for aluminum layer and 8.5 µm for pre-treated glass). This saturation on depth is related with the defocusing of laser beam over the substrate by increasing the depth of the channel, leading to less energy per area, which means that there is not enough energy to take out the material detached on the ablation process.

So in summary the first factor try to relate the roughness at the surface as a scattering centre that improves the coupling of light into the material enabling the subsequent transfer of energy from the light to the substrate. Light reflected from

a smooth metallic surface is confined to a specularly reflected beam. The intensity of this reflected beam is given by Fresnel's equations and it depends on the polarization state of the incident light, the angle of incidence, and the optical properties of the metal. Typically this is an ideal situation as for thin metals deposited on glass substrates the coatings are not smooth. So when light is reflected from rough surfaces, two new phenomena occur.

Firstly, the specular reflection does not occur; the reflected scattered light is directed away from the direction defined by the specularly reflected beam resulting in a reduction in the specularly reflected intensity.

Secondly, additional excitations or currents may be generated across the pits and bumps on the roughened surface. These excitations, known as surface plasmons, can give rise to additional fields which mix with the specular and scattered intensities forming surface plasmon polaritons.

The study of the surface plasmon polaritons are outside the scope of this study, but it is proposed that the scope for generating plasmonic excitations at the interface of a dielectric material with a random array of aluminium particles is likely to form part of the enhanced mechanism [Villesen2012]. As yet there is no firm evidence to support this hypothesis, the following points are made however to justify further investigations:

- The enhancement mechanism only works for thin metal coatings consisting of a random arrangement of nanoparticles.
- The nanoparticle sizes are smaller than the wavelength of light indicating that plasmonic behavior is likely to occur.

- The coatings have a reduced reflectivity that evidences possible plasmonic absorption.
- The optical penetration depth of the thin aluminium layer indicates that there is scope for the incident electromagnetic field and the laser to interact at the metal dielectric interface.
- The surface plasmon polariton mode decays non-radiatively although the different decay routes have not been investigated.

4.6.2 Factors affecting ablation region: Role of diffusion

The diffusion of metal ions into the glass is of relevance to the manufacture of glass-based optical materials which is expected to maintain the same properties before and after laser machining. Because of this, the structural changes of the glass during the covering process and after laser exposure have been analyzed, in order to know if the aluminum diffuses into the glass. In this case the diffusion will contaminate the sample yielding to a reduction of our technique capabilities.

4.6.2.1 Diffusion at covering the glass

To investigate the diffusion of metal ions into the glass during the process of covering the glass with a thin aluminum layer, the glass is covered with an aluminum layer of 15-20 nm thickness, which is then removed using a mixture of acids, composed by nitric acid and hydrochloric acid, in a volume ratio of 1:3. Then the etched surface is analyzed with the EDX technique. Table 4.2 shows the composition of soda-lime glass before and after the treatment explained above.

Table 4.2 Composition of soda-lime glass before and after the treatment.

Before treatment		After treatment	
<i>Element</i>	<i>Weight%</i>	<i>Element</i>	<i>Weight%</i>
O	50.58	O	50.25
Na	7.22	Na	8.08
Mg	2.27	Mg	2.19
Al	0.47	Al	0.49
Si	30.70	Si	32.08
Ca	4.44	Ca	4.87

Since the variations of aluminum percentage measured at different points of the glass previous to deposition of aluminum layer was in the order of 0.03 %. From table 4.2, it can be appreciated no significant additional aluminum is observed in the glass, so we can say that the coating process do not contaminate the glass.

4.6.2.2 Diffusion during ablation.

Next the diffusion of aluminum ions into the glass during the ablation of the glass was investigated. In order to get information about the diffusion of metal ions into the glass, a channel was fabricated over the glass using the aluminum layer; after this the aluminum layer was etched and then analyzed using EDX.

Figure 4.21 shows a top view of the soda-lime glass and the points selected for obtaining the composition data using EDX. Spectrums 1, 2 and 3 were obtained in the bottom of the channel and spectrum 4, 5 6 and 7 were obtained out of channels and over the surface of unprocessed glass.

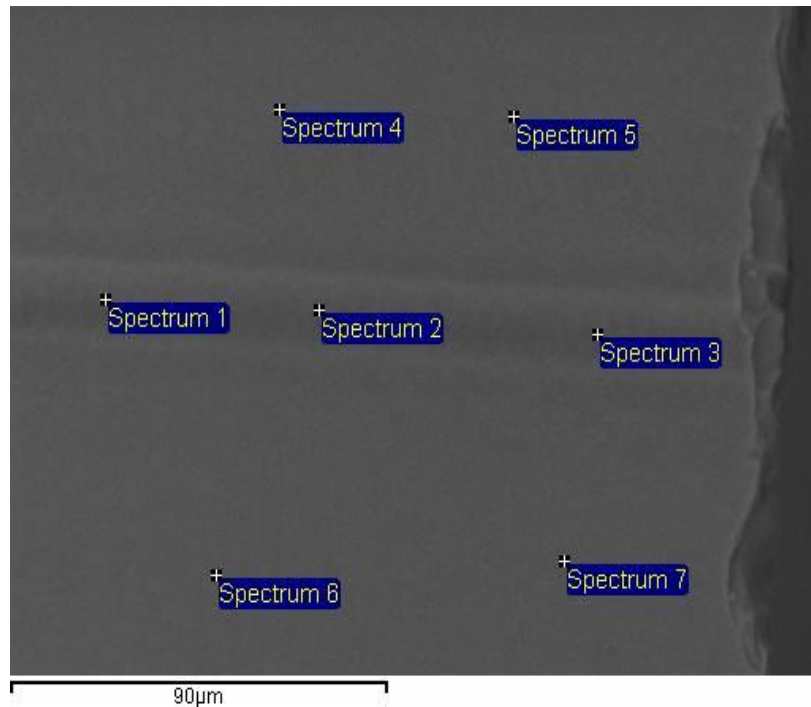


Figure 4.23 SEM picture of soda-lime glass and the points selected for analyzing the variations in composition after laser ablation.

Table 4.3 shows the relative compositions obtained in different places of the laser etched glass, locations 1,2, and 3 shows the EDX analysis at the bottom of the channels where laser –aluminum interactions occurred , locations 4,5,6,7 shows EDX analysis outside of the channels where no laser-aluminum interaction occurs.

Table 4.3 Spectrums obtained for different places of the glass substrate using EDX.

Element	Spectrum 1	Spectrum 2	Spectrum 3	Spectrum 4	Spectrum 5	Spectrum 6	Spectrum 7	Glass
O	49.22	50.54	50.04	49.69	49.35	49.22	50.21	50.58
Na	7.52	8.46	7.05	8.12	7.55	7.52	8.02	7.22
Mg	2.34	2.53	2.25	2.03	2.14	2.34	2.38	2.27
Al	0.41	0.54	0.52	0.46	0.59	0.41	0.45	0.47
Si	30.66	32.13	30.35	28.27	28.22	30.66	30.60	30.70
Ca	4.72	4.75	4.34	3.98	3.94	4.72	4.71	4.44

Comparing those results, and within the sensitivity of EDX technique, we can conclude that “little or no diffusion” occurred in the laser treated glass.

This initial result is in agreement with a simple model for diffusion. The diffusion of the metal ions in a glass matrix is governed by Fick’s second law. In one dimension into the depth of the material, the profile metallic impurities are given by equation (4.5).

$$\frac{\partial N}{\partial t} = D \frac{\partial^2 N}{\partial x^2} \quad (4.5)$$

where N is the concentration of the metal ions, D is the diffusion coefficient, t is the time variable and x represent the depth magnitude.

The solution of this differential equation requires consideration of the appropriate boundary and initial conditions. The solution provides an estimation of the impurity distribution, in depth and time, for the metal ions in the glass material. We consider the initial case of a constant surface concentration, where a metal layer deposited on the glass acts like an unlimited source of metal dopants, providing metallic ions into the glass materials. In this case the solution is given by the complementary error function Eq.(4.7)[Sze2001] where,

$$N(x, t) = N_0 \operatorname{erfc}\left(\frac{x}{2\sqrt{Dt}}\right) \quad (4.7)$$

Equation (4.7) describes the distribution of metal ions in the glass material with depth and time following exposure of the thin film / glass matrix to an initial laser pulse. N_0 is the initial metal ion concentration at the surface. N_0 can be either represented by the solid solubility of aluminum in the glass material or by the

concentration of aluminum atoms at the surface. If it is assumed that the initial concentration of aluminum at the glass surface is given by the solid solubility, estimated to be 10^{19} - 10^{20} atoms / cm^3 , the diffused profile of these atoms with depth in the material can be estimated by making the following assumptions: a diffusion coefficient of Al atoms in glass of $10^{-12}\text{cm}^2\text{s}^{-1}$; this value is representative of impurity atoms in crystals but this value is regarded as being reasonable for the case of amorphous glass also; the time for appreciable diffusion takes place after a single pulse, it is estimated to be around 4 times the pulse duration. Using these values an estimation of the diffusion profile is obtained. This is shown in figure 4.22.

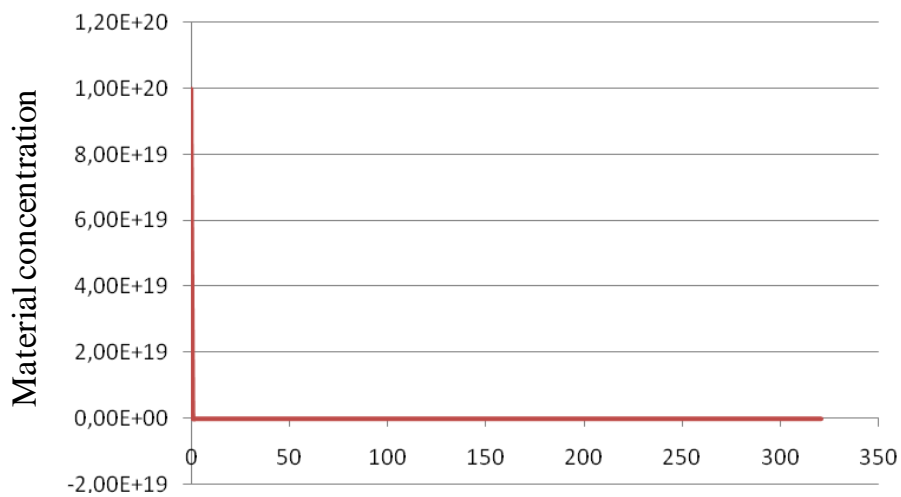


Figure 4.22 Diffusion profile estimated.

This figure confirms the experimental results where diffusion is unlikely to take place in the material.

4.6.3 Factors affecting ablation region: Role of charge transfer.

At short pulse duration, using the absorber layer, sub-surface damage appears in the glass. The initial damage potentially acts as a seed that can initiate further sub-surface damage. It is assumed to be a thermal mechanism which leads to micro-crack formation inside the glass and near to the surface through a thermal shock process. One factor that needs to be considered is related to how the heat is generated during the laser-layer interaction with the sub-surface thermally damaged region. This amorphous region is significantly larger than the associated with the surface damage features and extends through several microns below the laser mark. This initial structure interacts with the laser and results in further enhanced damage created by the laser beam both within a single pulse and between successive pulses. Figure 4.23 shows a comparison between thermal damage and surface damage. Each image correspond to the interaction of one laser shot with the aluminum layer-glass sample, showing the part of aluminum layer removed from glass, and the subsequent damage generated over the glass.

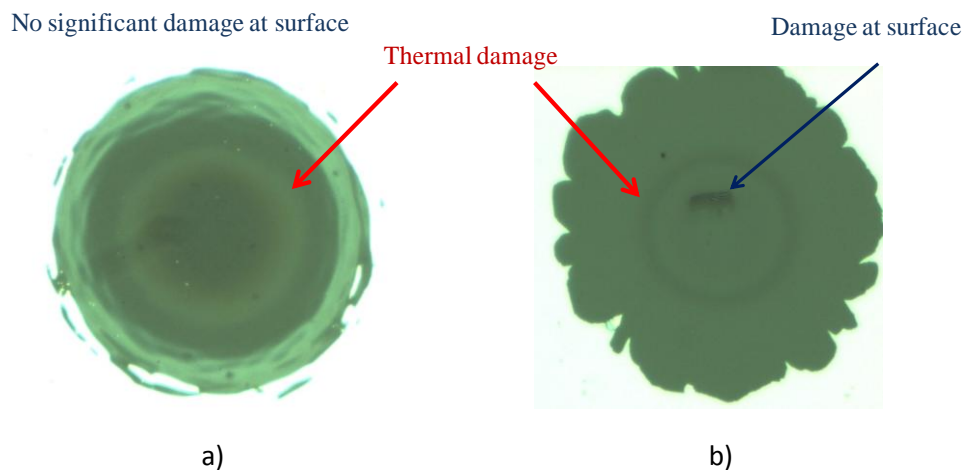


Figure 4.23 Microscopic images showing a comparison of a) sub-surface damage and b) on surface damage Figure 4.24 shows the evolution of damage with the number of

pulses. The red line shows the ring generated below the surface. Damage at surface is indicated using black arrows

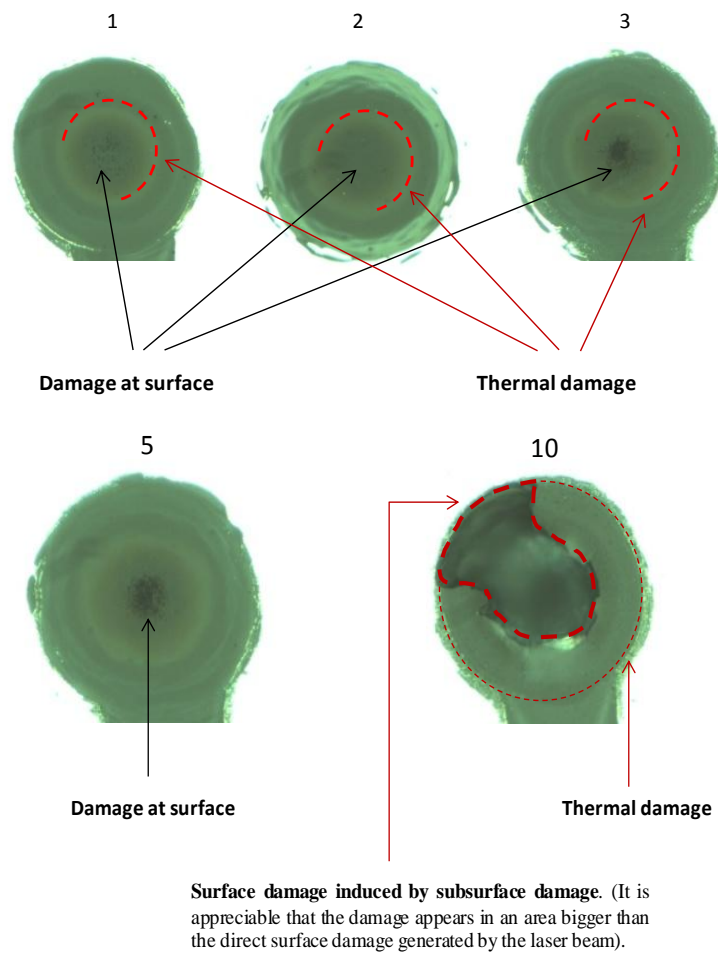


Figure 4.24 Evolution of damage with number of pulses.

After repeated application of laser pulses in the same position, the micro-crack propagates to finally define the size of the mark; the feature appears to originate from the thermal damage. As it was expected after 10 pulses, the size of the crater is bigger than the size of the laser induced damage generated at surface.

These images indicate that the damage is initiated in the sub-surface but propagates towards the surface with subsequent pulses.

The third factor to be considered assumes that the aluminum layer transfers energy to the glass. This creates a gradient of temperature inside the glass. While no significant damage is expected at surface initially, the internal damage contributes to the ablation at the surface within a long pulse or for subsequent pulses.

Ideally a thin film metal layer deposited over glass substrate should allow a highly excited electronic charge distribution to diffuse between the metal and the glass. When a metal layer and a glass substrate are in contact, an electrical potential difference arises at the interface. This corresponds to the energy that must be provided in order to excite an electron from the conduction band in the metal to a free electron state in the vacuum; this is defined as work function. For aluminum the values are estimated to be 4.0-4.41 eV. The potential difference to transfer an electron from an aluminum metal and a glass material is similar and has been estimated to be 4.19 eV [Jiang2003, Chen2012]. Therefore the temperature for electrons in a continuous metal film would need to be increased by 5×10^4 K to enable them to be transported from the metal to the glass dielectric. It is noted that work function cited here may not be relevant as the electrons are confined to small nanoparticles which impacts their dynamics [Villesen2012]. If the transfer of electronic energy from the metal to the glass was possible, the free electrons in the glass could readily absorb energy from a long laser pulse and thereby lead to enhanced absorption and avalanche ionization within the glass material.

CHAPTER 5

MICROSTRUCTURING OF GLASS: FABRICATION AND CHARACTERIZATION

A direct-write technique for fabricating plano-convex microlenses and microchannels based on the laser ablation of a soda-lime glass is reported. A wet chemical etching technique (HF) was used successfully to carry out smoothing of surfaces fabricated on the soda-lime glass. The mechanism to modify the surface roughness and shape through etching time and the temperature of the etching solution are also studied. By applying a thermal treatment, it was able to modify the shape of the elements. The influence of temperature, heating time and the mechanism of thermal displacement are described here. Finally, a morphological and optical characterization of the elements fabricated is given.

5.1 Introduction.

A direct-write technique for fabricating plano-convex microlenses and microchannels based on the ablation of a soda-lime glass substrate with a laser beam of circular Gaussian profile is presented. The laser setup consists of a nanosecond Q-Switch Nd:YVO₄ laser operating at the fundamental wavelength of 1064 nm combined with a galvanometer system. Laser parameters selected as suitable from results obtained in chapter 4, were an average power of 7 W and a repetition rate of 10 kHz.

A wet chemical etching technique (HF) was used successfully to carry out smoothing and cleaning of surfaces fabricated on the soda-lime glass. Following cleaning processing a thermal treatment in an oven was used for reflowing the glass surface. By applying the thermal treatment a modification of the shape of the elements occurs, as well as an improvement of the morphology in terms of roughness and elimination of micro crack defects generated during laser ablation. The thermal treatment was applied using a Heraeus Mufla furnace, equipped with a thermal ramp that allows us to control the heating speed of the glass.

5.2 Laser microstructuring of glass

The laser setup consists of a nanosecond Q-Switch Nd:YVO₄ laser operating at a wavelength of 1064 nm combined with a galvanometer system for addressing the output laser beam. The laser is focalized onto the sample with a flat-field lens, with effective focal length 100 mm, that provides a uniform irradiance distribution on glass substrate over an area of 80x80mm² (Figure 5.1).

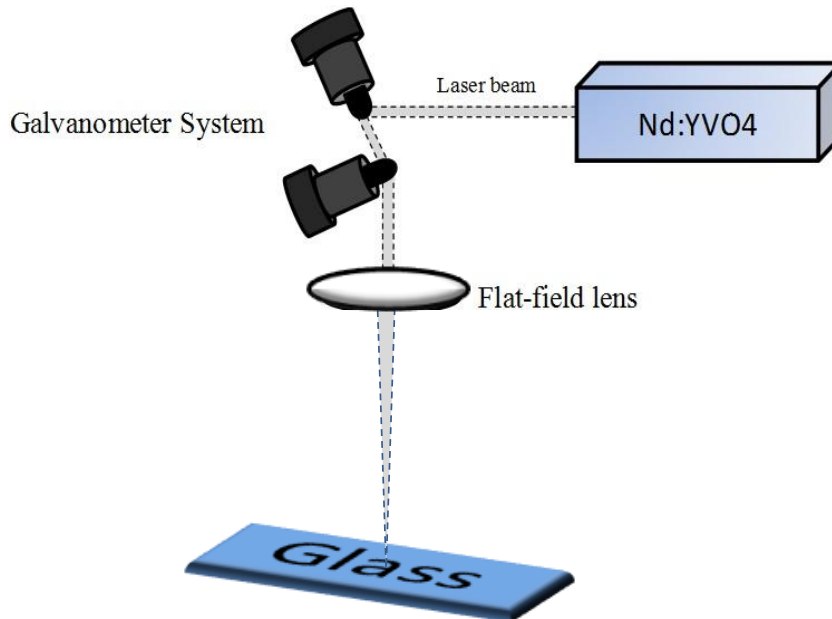


Figure 5.1. Laser set-up for microstructuring glass.

In order to design and fabricate microlenses and microchannels a previous study was made by focusing one laser shot on the glass substrate [section 4.5.2 of chapter 4]. The mark obtained was analyzed with a confocal microscope SENSOFAR 2300 P μ . The initial characterization was used to determine the appropriate laser parameters needed for the fabrication of the microlens arrays and microchannels on the soda lime glass substrate.

For fabricating microlens, each cylindrical structure that will lead to microlens after a thermal treatment is obtained by the ablation of a circular trench formed by moving the laser beam, using the galvanometer mirror system, relatively to a stationary glass sample (Figure 5.2c). A time of 10 seconds is required to expose an area of 2x2 mm². Figure 5.2a and 5.2b show the scheme of the hexagonal packed array designed for fabricating the microlens array.

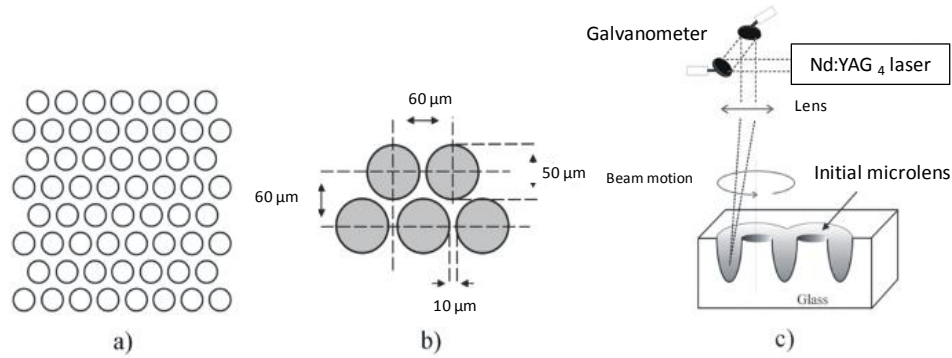


Figure 5.2 a) Hexagonal close packed pattern, b) Microlens array arrangements: diameter and pitch. c) Lateral view of the cylindrical trench formation.

In the case of microchannels, each structure is obtained by the ablation of individual lines on different configurations on soda-lime glass substrate using a galvanometer system.

Figure 5.3 shows the cylindrical structures that will lead to microlens and the microchannels obtained by laser direct write. The samples were characterized by a confocal microscope SENSO FAR 2300 PLμ.

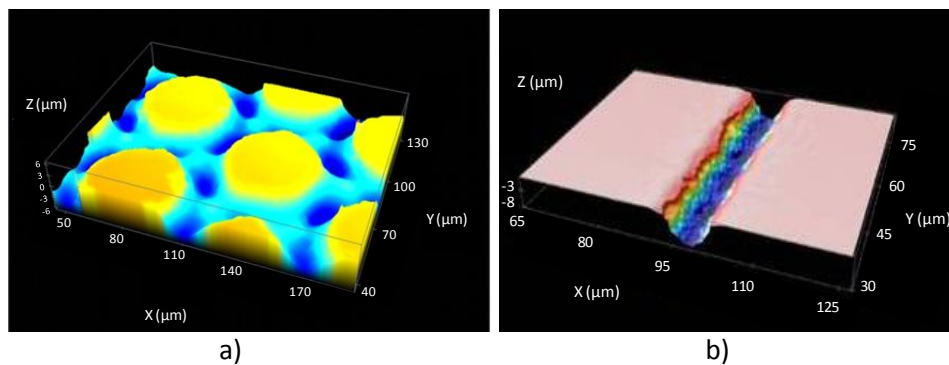


Figure 5.3. 3D confocal image of a) cylindrical post b) microchannel fabricated on soda-lime glass by laser-direct write.

The first experimental approach for obtaining uniform channels and cylindrical structures was to check different scan speed for getting the optimal pulses

overlapping and laser parameters. Section 4.5.2 of chapter 4 describes the previous experiments performed for obtaining the optimal laser parameters. After laser processing, in order to obtaining microlens and microchannels, a chemical etching and a thermal treatment in an oven was applied to the elements to reflow the glass surface and improve the topography in terms of roughness. The chemical etching and thermal treatment mechanism are studied in the next sections.

5.3 Thermal treatment.

The cylindrical structures and microchannels fabricated by direct laser write were subjected to thermal treatment into a mufla oven Heraeus and a Vita Vacumat 6000M (for specifications see section 3.3 of chapter 3).

Regarding the mechanism of thermal reflow for microlens fabrication, the displacement of material from the upper surface and the consequential accumulation at the bottom surface of the feature leads to a reduction in height of the island structure generated by the laser. The approximate diameter is maintained because of the confluence of the material reflowed from the top of adjacent microlens to the bottom of the crater. This effect permits to fill the irregular structure of surface leading to an improvement of the optical and morphological qualities of the glass structures.

Figure 5.4 shows the mechanisms involved in the process, which leads to morphological shape modification from the initial cylindrical post to a microlens formation. The black line shows the profile of the initial post obtained by laser ablation and dot lines the profile of resulting microlens after thermal treatment.

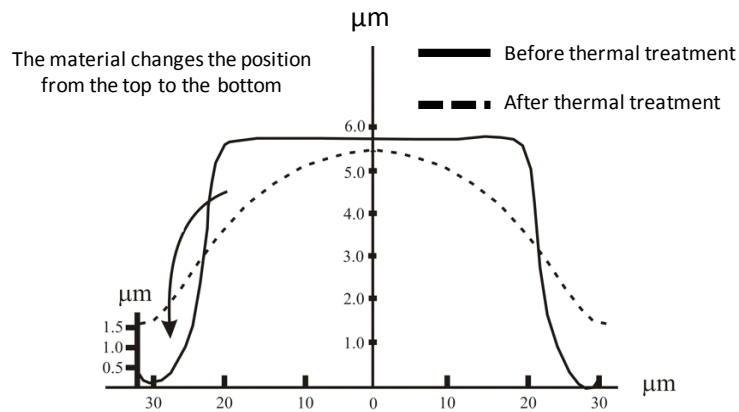


Figure 5.4 Material displacement mechanisms for fabricating microlenses.

It can be observed in Figure 5.4 that the laser ablation creates cylindrical posts with a flat top surface without any refracting power. The profile of the initial laser etched microlens is similar to a cylindrical shape with the corners of the features being partially rounded. The conversion of the initial pattern of glass posts fabricated by laser ablation into the appropriate shape for the microlens starts above the glass transitions temperature ($T_g = 564^\circ\text{C}$), where the viscosity of the glass is reduced and thus the surface tension of the melted material induces the modification of the surfaces shape through the redistribution of the material from the top sides of the trench to the bottom of the crater. Based on this, it was decided to apply the thermal treatment for temperatures above T_g , (620°C , 630°C , 640°C , 650°C , 660°C , 670°C , 680°C) during 2 hours. The morphology in terms of shape was analyzed with confocal microscope SENSOFAR 3200 P1 μ .

For a temperature of 620°C or lower, there was almost no change in the microlens shape. But at temperatures higher than 670°C , the initial cylindrical surface profile becomes increasingly flattened, so microlenses were not obtained. Figure 5.5 shows the cylindrical posts obtained by laser ablation and the same element after the oven treatment at 670°C for 2 hours.

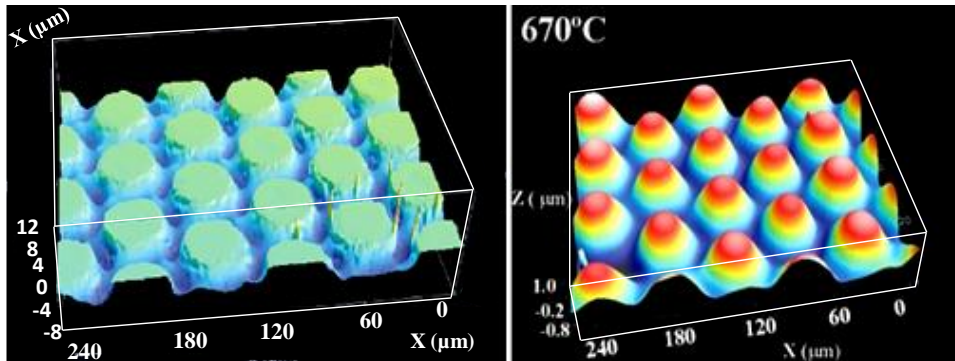


Figure 5.5 a) Confocal image of the cylindrical posts obtained by laser ablation and b) after 2 hours of thermal treatment at 670°C.

The material displacement mechanism for microchannel fabrications is similar to that for fabricating microlens. Figure 5.6 shows the material displacement mechanisms for fabricating microchannels. The black line shows the profile of the initial channel obtained by laser ablation and dot lines the profile of resulting microchannels after thermal treatment.

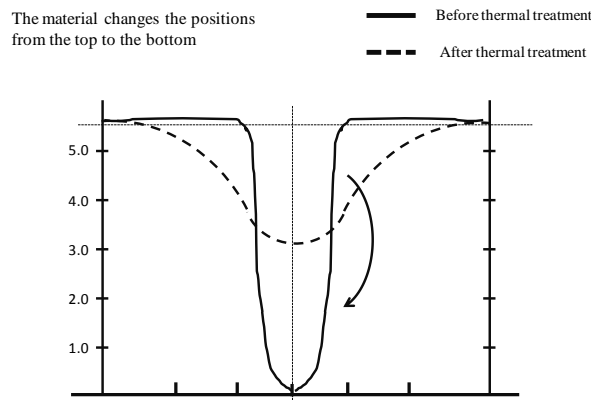


Figure 5.6 Material displacement mechanisms for fabricating microchannels.

Figure 5.7a and 5.7b shows a microchannel after thermal treatment for 2 hours at 620°C and 670°C, respectively.

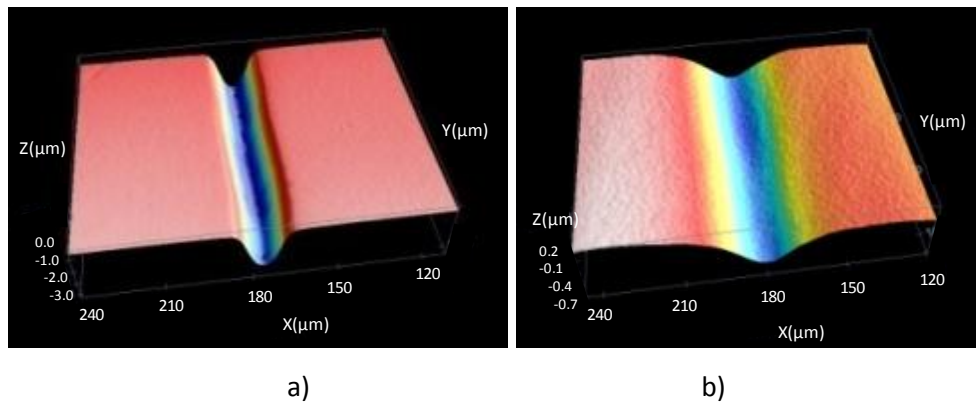


Figure 5.7 Confocal images of the microchannels when into the oven at a) 620°C and b) 670°C.

Since the purpose of thermal treatment in the case of microchannels is to reduce the roughness generated during laser ablation, it is important to find a compromise between shape modification and roughness reduction. Ideally the shape should be maintained while the thermal reflow should reduce the surface roughness. By applying the thermal treatment at 620°C (during 2 hours) it was able to obtain high quality microchannels maintaining the initial shape but reducing the roughness. At 670°C the roughness obtaining is similar to the unprocessed glass but the shape changes considerably.

In terms of roughness, the thermal treatment permits us to obtain values of roughness in the range of unprocessed glass. Table 5.1 shows the Ra of microchannels obtained at different temperatures.

Table 5.1 Roughness average determined bottom of the channels

Ra Glass	3.6 nm
Ra Glass after laser	2480 nm
Ra 620°C	125.1 nm
Ra 670°C	7.3 nm

5.4 Chemical Etching.

In order to reduce the rough surface produced directly through laser ablation, a wet chemical etching technique (HF) was performed and analyzed for microlens diameters of 20 μm , 40 μm , 60 μm and 140 μm .

The mechanism to modify the surface roughness and the shape depends on the concentration of the acid, on the etching time and on the temperature of the process. Hydrofluoric acid is an etchant which attacks glasses at significant high etch rate. However, HF is not only a strong corrosive, but also highly toxic towards higher concentrations, so the etching process was performed at 10% HF concentration, which in terms of security, means that there is not dangerous percentages of toxic vapor that contaminate the work space. Besides, HF etching was performed with at least one other person in the clean room and was handled in a laminar flow bench, using two pairs of nitrile gloves and eye protection.

The purpose of using HF etching was to eliminate the debris deposited over the glass after laser ablation and the secondary post unablated (see figure 5.8) due to the nature process and design configuration.

Figure 5.8 shows the results of exposing the initial structures obtained by laser ablation to a 10% HF etching during 5, 10 and 15 minutes. Figure 5.8a shows a 3D confocal image of one microlens before HF etching. Figure 5.8b shows the microlens arrays after HF etching for 5 minutes, 5.8c) for 10 minutes and 5.8d) for 15 minutes. Debris can be observed at the top of the microlens deposited during the laser ablation, secondary post unablated due to the hexagonal packagemnt of microlens arrays are also observed.

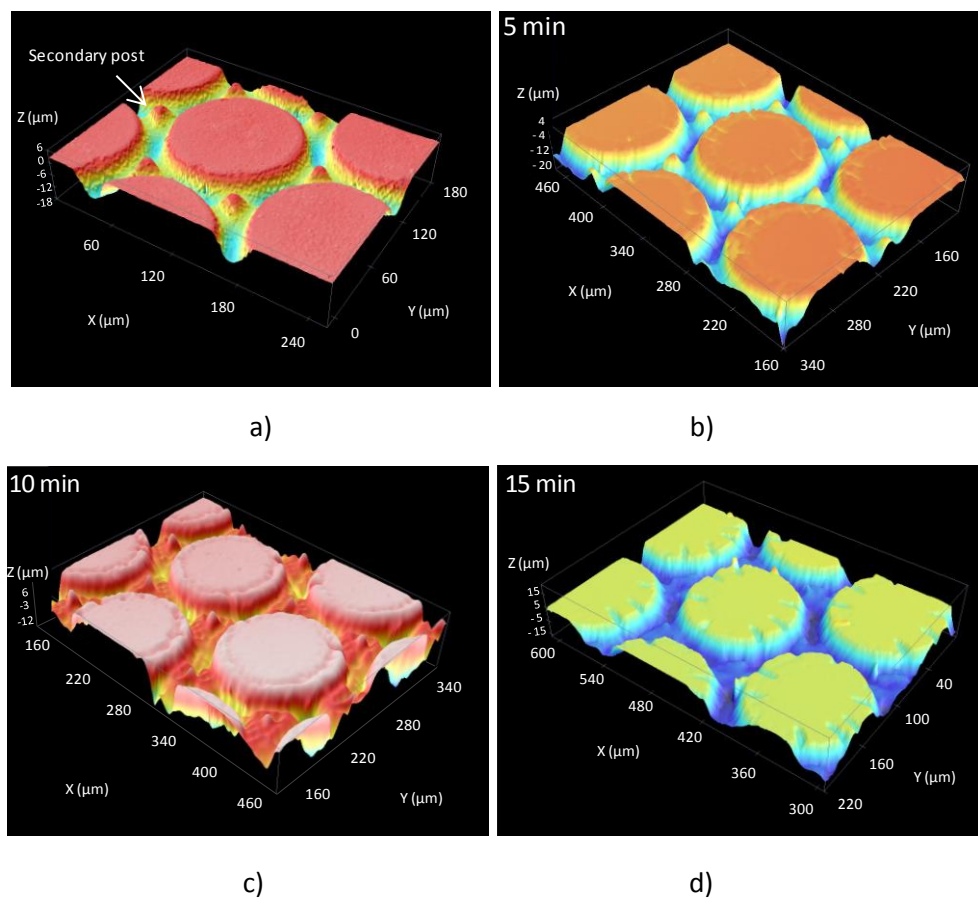


Figure 5.8 3D Confocal image of one microlens a) before HF etching and with b) HF etching during 5 minutes, c) 10 minutes and d) 15 minutes.

As it can be appreciated in figure 5.8, the chemical etching eliminates the debris deposited at surfaces of microlens during laser ablation and the secondary post. A FESEM ultra plus and a confocal microscope SENSOFAR 2300 PL μ were used for depth measurement and 3D mapping of the structures.

Figure 5.9 shows a SEM top view image of one microlens before HF etching. Debris deposited at the top of the microlens during the laser ablation can be observed. In figure 5.10 we can see that after chemical etching, they were successful eliminated.

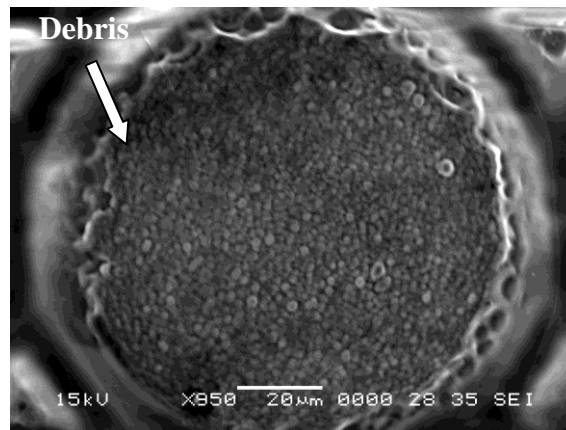


Figure 5.9 SEM image of the microlens top surface before chemical etching

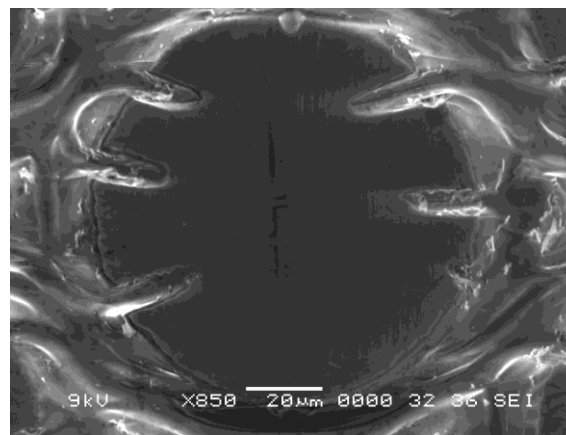


Figure 5.10 SEM image of the microlens top surface after 10 minutes in 10% HF aqueous solution.

The elimination of debris will improve the optical quality of the microlens, while if maintained at the top of microlens they would be mixed with the glass material during the thermal treatment resulting in bad optical quality. Figure 5.11 shows a wider top view SEM image of the microlens arrays before HF etching where it is possible to see the secondary posts surrounding the microlens, which are related with the hexagonal packaging of the microlens arrays.

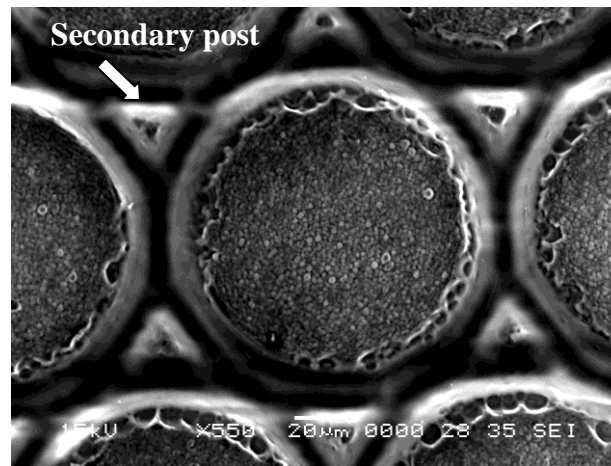


Figure 5.11 SEM image of the microlens array surface after chemical etching.

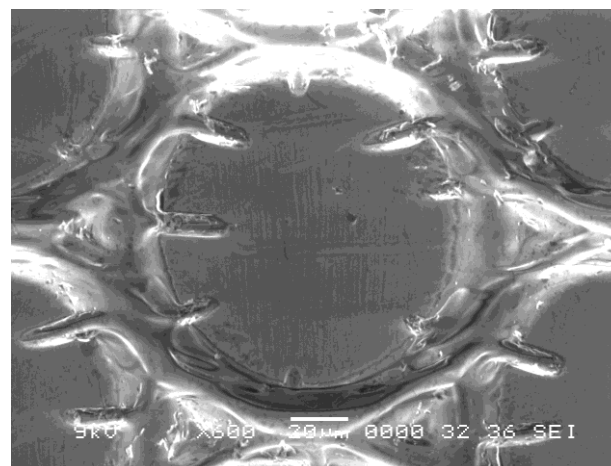


Figure 5.12 SEM image of the microlens array surface after 10 minutes in 10% HF aqueous solution.

It can be appreciated in figure 5.12 that with the chemical etching, the secondary posts were reduced in size. The elimination of the secondary post let the material to flow during the thermal treatment, leading to good material distribution and resulting in microlens formation. Figure 5.13 shows the profile of microlens arrays after 10% HF etching at different times. At this moment we pay attention to the shape of the secondary posts.

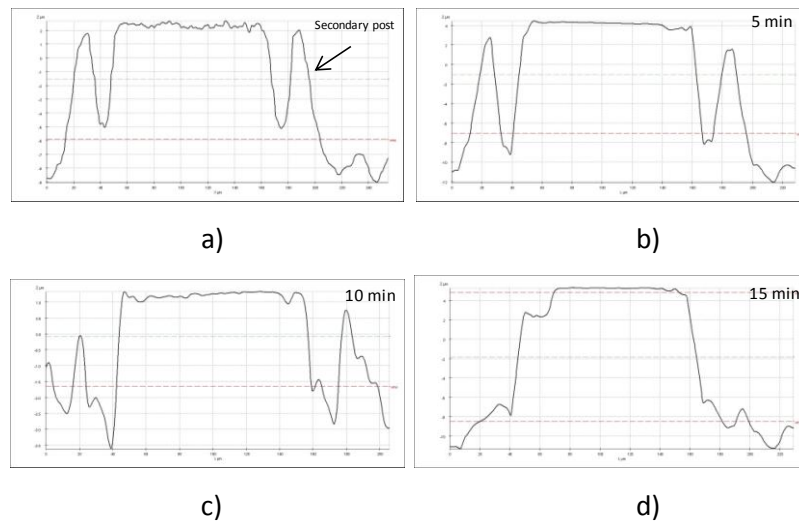


Figure 5.13 Profile of principal and secondary post after applying a 10% HF etching at different times, a) non chemical etching, b) 5 minutes, c) 10 minutes and d) 15 minutes.

In figure 5.14 it is possible to see in more detail the evolution of the shape by superimposing the profiles of the posts obtained at the different etching times.

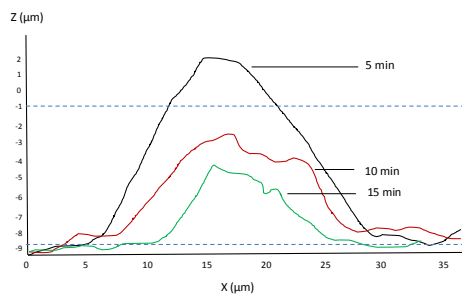


Figure 5.14 Secondary posts profile of microlens of 140 μm diameter.

It can be appreciated in figure 5.13 and Figure 5.14, that the chemical etching nearly eliminate the secondary post, but also cause some damage over the microlens. Since the damage generated at the top of microlens, for the case of 10 minutes, can be eliminated by the thermal treatment, a time of 10 minutes for the acid process was selected.

Additionally, it was study the role of the HF etching over the diameter of the microlens. To this purpose, arrays of microlens of diameter 20 μm , 40 μm , 60 μm and 140 μm were fabricated and subjected to the HF and thermal treatment. Figures 5.15 - 5.18 shows 3D confocal images of the microlens arrays for diameters of 20 μm , 40 μm , 60 μm and 140 μm , respectively.

Figure 5.15 shows 3D confocal images of the initial cylindrical structures of diameter 20 μm subjected to a different process, 5.15a) the post generated by laser ablation, 5.15b) the same element after being introduced in a 10% HF bath for 10 minutes, 5.15c) the initial sample after a thermal treatment into an oven for 2 hours at 670 $^{\circ}$ C and 5.15d) the initial post with a chemical etching of 10%HF bath for 10 minutes and a thermal treatment into an oven for 2 hours at 670 $^{\circ}$ C.

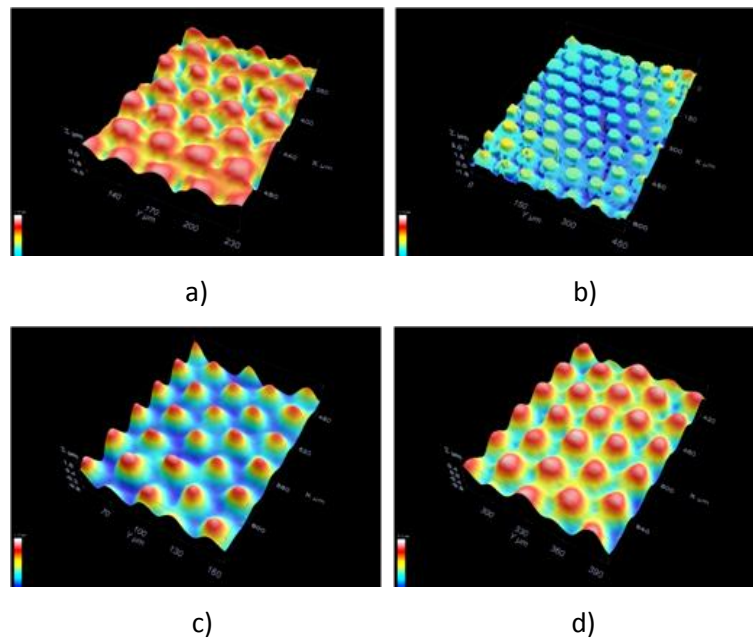


Figure 5.15 3D confocal images of a) initial structures fabricated by laser ablation, b) after chemical etching c) after thermal treatment and d) after a combination of chemical etching and thermal treatment.

It can be appreciate in figure 5.15b, that the chemical etching makes the initial structures more defined by eliminating the unwanted structure between the

cylindrical posts caused by laser ablation, so the material displacement caused by the thermal treatment is more regular, leading to a better microlens. Although without using the chemical etching it was possible to obtaining microlens (figure 5.15c), for diameter of 20 μm the combination of laser ablation, chemical etching and thermal treatment improve the quality of the final microlens (figure 5.15d).

Figure 5.16 shows 3D confocal images of the initial cylindrical structures of diameter 40 μm subjected to a different process: fig. 5.16a) posts generated by laser ablation; fig. 5.16b) the same element after being introduced in a 10% HF bath for 10 minutes; fig. 5.16c) the initial sample after a thermal treatment into an oven for 2 hours at 670° C; and fig. 5.16d) the initial cylindrical structure with a chemical etching of 10%HF bath for 10 minutes and a thermal treatment into an oven for 2 hours at 670° C.

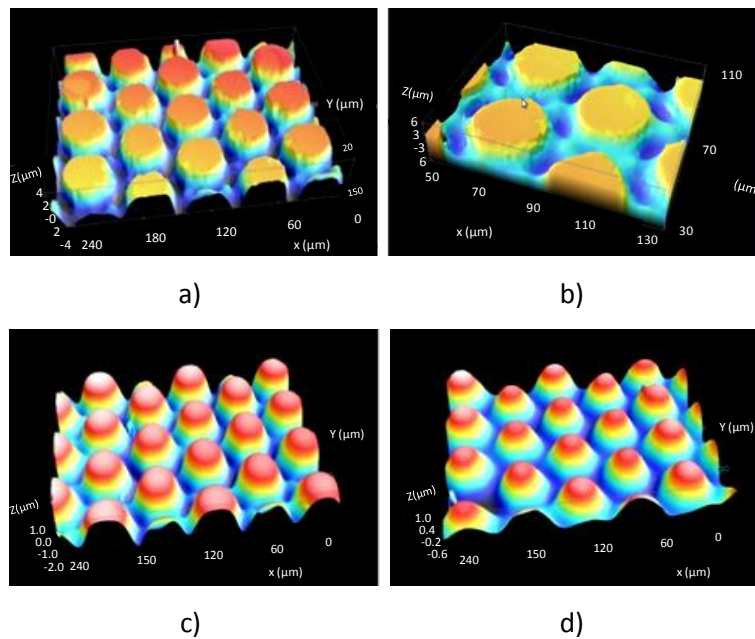


Figure 5.16 3D confocal images of a) initial structures fabricated by laser ablation, b) with chemical etching c) with thermal treatment and d) a combination of chemical etching and thermal treatment.

It can be appreciate in figure 5.16b, that the chemical etching does not improve the initial structure. It can be related with the packaging of microlens and with the size of laser mark at substrate for 40 μm designs, which makes an initial structure more regular than other diameters. Without using the chemical etching it was possible to obtaining good microlens (figure 5.16c), so for diameter of 40 μm the chemical etching does not present significant improvements (figure 5.16d).

Figure 5.17 shows 3D confocal images the initial cylindrical structures of diameter 60 μm subjected to the different processes: fig. 5.17a) the post generated by laser ablation; fig. 5.17b) the same element after being introduced in a 10% HF bath for 10 minutes; fig. 5.17c) the initial cylindrical sample after a thermal treatment into an oven for 2 hours at 670° C; and fig. 5.17d) the initial post with a chemical etching and a post thermal treatment.

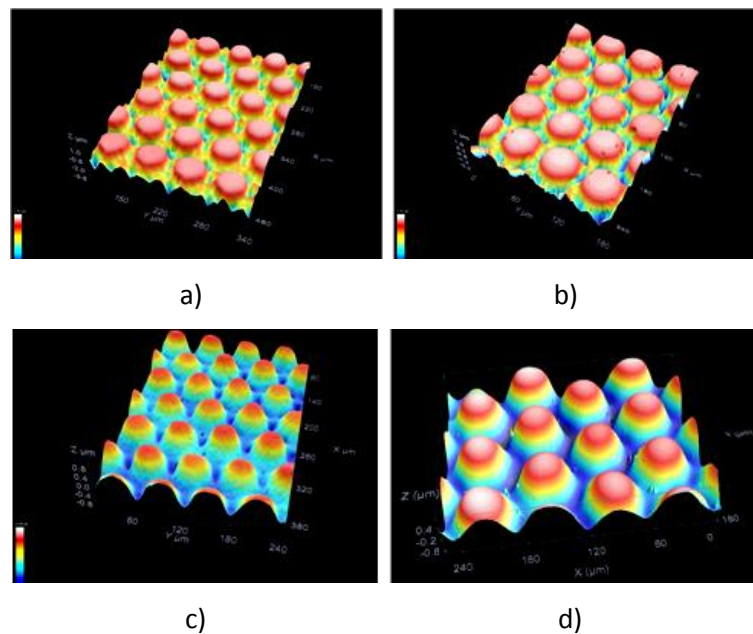


Figure 5.17 3D confocal images of a) initial structures fabricated by laser ablation, b) after chemical etching c) after thermal treatment and d) after a combination of chemical etching and thermal treatment.

As can be appreciate in figure 5.17b, the chemical etching makes the initial cylindrical elements more defined by eliminating the bad structure between the cylindrical elements, so the material displacement caused by the thermal treatment is more regular, leading to a better microlens. Although without using the chemical etching it was possible to obtaining microlens (figure 5.17c), for diameter of 60 μm , the combination of laser ablation, chemical etching and thermal treatment improve the quality of the final microlens (figure 5.17d).

Figure 5.18 shows 3D confocal images of the initial cylindrical structures of diameter 140 μm subjected to a different process; fig. 5.18a) the post generated by laser ablation; fig. 5.18b) the same element after being introduced in a 10% HF bath for 10 minutes; fig 5.18c) the initial sample after a thermal treatment into an oven for 2 hours at 670°C; fig. 5.18d) the initial post with a chemical etching of 10%HF bath for 10 minutes and a thermal treatment into an oven for 2 hours at 670°C.

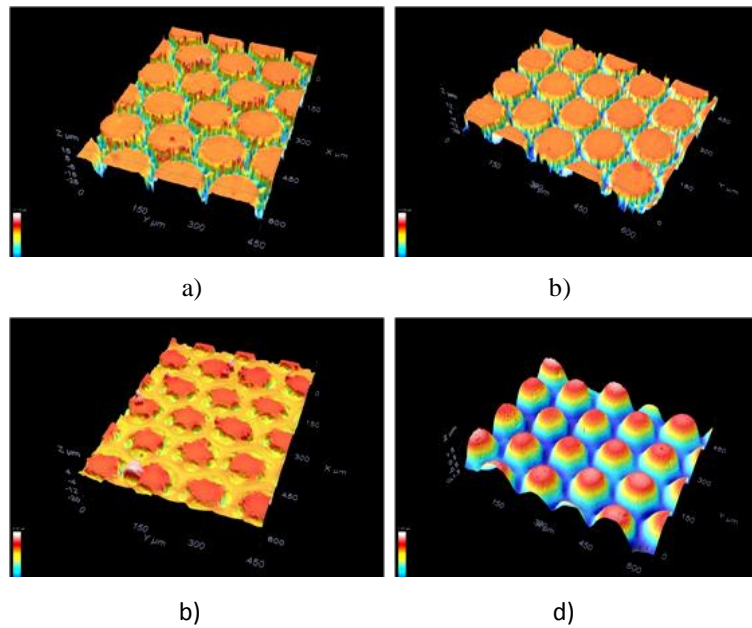


Figure 5.18 3D confocal images of a) initial structures fabricated by laser ablation, b) after chemical etching c) after thermal treatment and d) after a combination of chemical etching and thermal treatment.

It can be appreciate in figure 5.18b, the chemical etching makes the initial structures more defined by eliminating bad structures generated and the secondary post generated by the laser ablation process. The secondary post are bigger at diameter 140 μm and interact with material of cylindrical post during material displacement of thermal treatment, so without using the chemical etching it was not possible to obtaining microlens (figure 5.18c). So for obtaining microlens of diameter 140 μm we need to use a combination of laser ablation, chemical etching and thermal treatment. For diameter of 60 μm and 140 μm it were obtained focal length values of 1.180 mm +/- 40 μm and 5.100 mm +/- 200 μm , respectively.

5.5 Morphological and optical characterization.

In this section we present the morphological and optical characterization of microchannels and microlens. It can be appreciate how the shape of microlens is modified with the thermal treatment and the consequent improvement of the optical properties. It is also presented the evolution of roughness with the thermal treatment.

5.5.1 Microlens.

In this section we present the fabrication of arrays of microlenses of diameter 40 μm in a lattice with hexagonal symmetry. We present only the characterization of these microlens because in their fabrication is not necessary the use of the chemical etching process. Figure 5.19 presents 3D images of microlens obtained after the thermal treatment at different temperatures. The images were obtained with a SENSOFAR PL μ 2300 confocal. The change in the shape of the microlenses, as well as the filling of the holes between consecutive microlenses is observed.

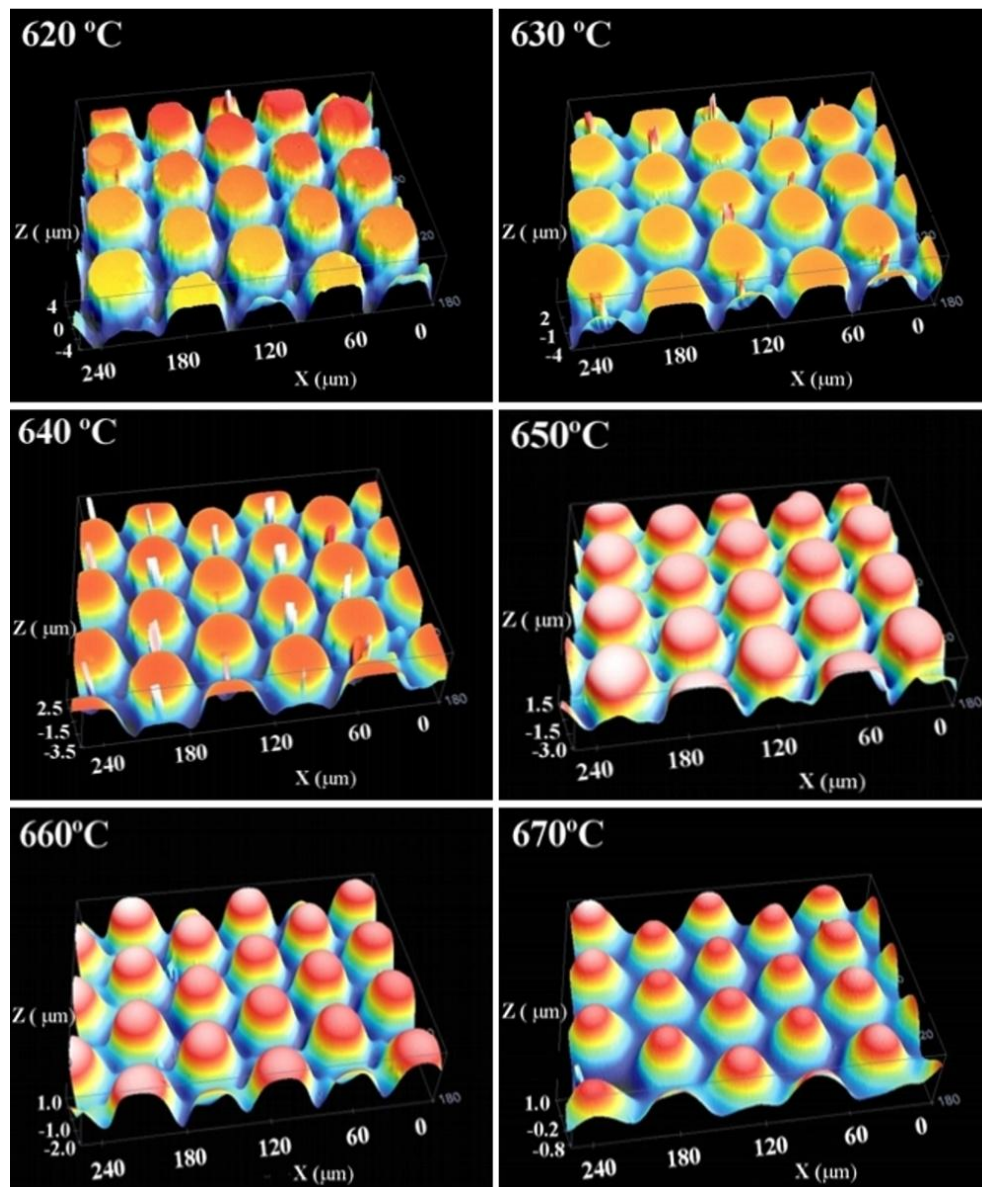


Figure 5.19 3D confocal images of microlenses (Diameter: $40\ \mu\text{m}$) obtained for different temperatures of the thermal process.

Figure 5.20 presents, for comparison, the profile of one microlens randomly chosen from one of the arrays fabricated at different temperatures. The shape of the microlens evolves from a flat-top post to a quasi-parabolic profile as the

temperature treatment increases. In the case of 620°C some irregularities in the surface generated by the laser ablation step were observed. For temperatures of 630°C and higher these irregularities disappear. The diameter of the microlenses is maintained almost constant over the range of temperatures tested, while the sag decreases due to the redistribution of the material from the top sides of the trench to the bottom of the crater. Temperatures out of this range were also analyzed; it was found that for values lower than 620°C there were almost no significant changes in the surface shape. By contrast, for temperatures higher than 670°C and 2 hours of thermal treatment, the initial array of cylindrical surface profile becomes flat, so the microlenses obtained by laser direct-write disappear.

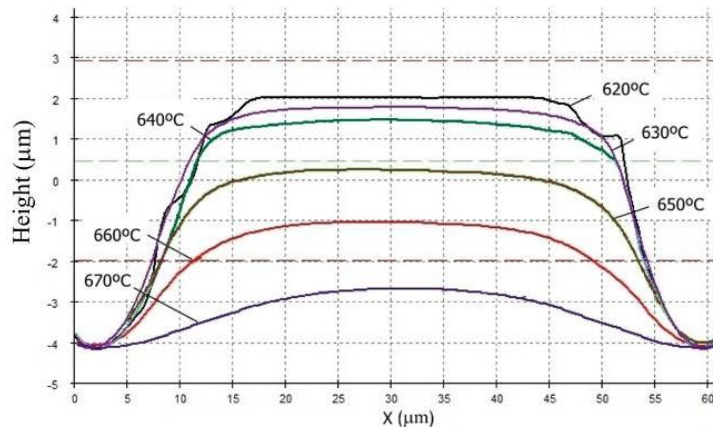


Figure 5.20 Cross-sectional profile of the microlens at different thermal reflow temperature.

Moreover, the initial irregular structure observed in Figure 5.20 for 620°C is improved by increasing the temperature, leading to a hexagonal shape for temperatures of 660°C and 670°C. This hexagonal profile was generated by enabling the material to reflow, which is related with the initial hexagonal packaging of microlens arrays. The refilling of the interstitial space also contributes to the reduction of the stray-light presented at the focal plane of the microlenses (see Figure 5.21 for details).

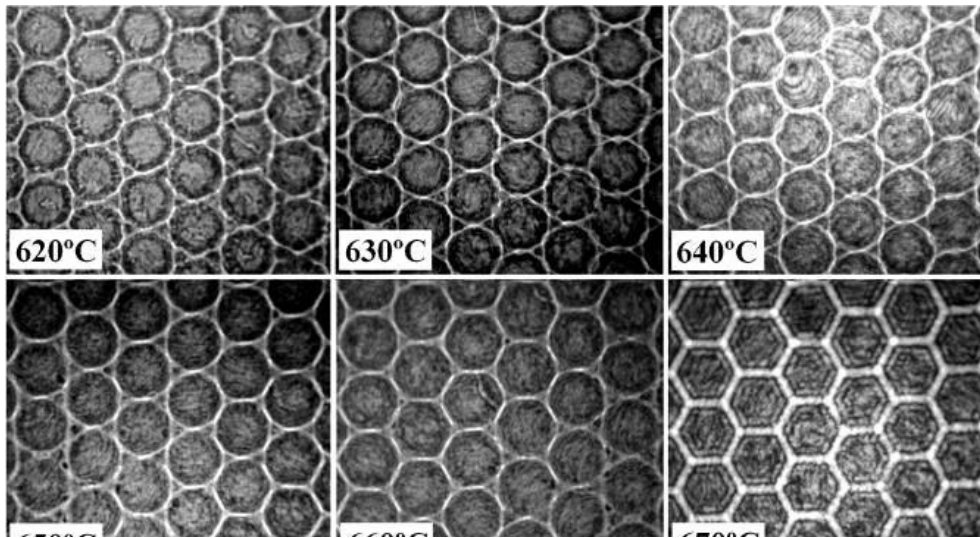


Figure 5.21 Pattern image of the microlens arrays at different temperatures. Images are generated by an optical microscope.

The properties of the fabricated microlenses were characterized in terms of its focal length and spot size. The experimental setup for measuring the focal length of the microlenses consisted of a He-Ne laser (632.8 nm), a 40x objective lens and a camera (fig.5.22).

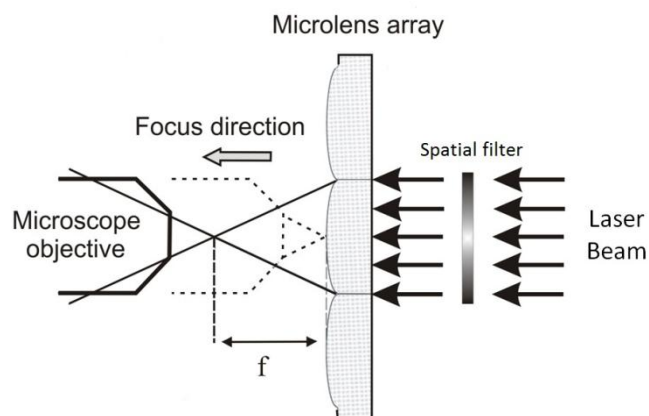


Figure 5.22 Experimental setup for measuring the focal length of the microlenses.

The microscope objective was focused on the surface of the microlenses, this location is recorded, and then the microlenses array is moved along z axis until the image of an arbitrary object is observed. The image is located at the focal plane of the microlenses. The difference between these positions is a measure of the focal distance of the tested microlens arrays. The accuracy of the data acquisition for this setup is $\pm 5 \mu\text{m}$. For determining the quality of the focus we used the beam profiler BP109-VIS of Thorlabs. The focus spot size is determined calculating the width at $1/e^2$.

The geometrical - morphological characterization of the microlenses was performed with the confocal microscope. The topographical data provided was used to measure their diameter, roughness and sag, defined as the distance from the top of the microlens to the bottom of the interstitial channel between two adjacent microlens. In table 5.2 we present de results obtained for all this parameters.

Table 5.2 Optical and geometrical parameters of the microlenses fabricated at different reflowing temperatures.

	Reflowing Temperature					
	620°C	630°C	640°C	650°C	660°C	670°C
Focal length (μm)	570 \pm 10	510 \pm 10	450 \pm 10	430 \pm 10	330 \pm 10	510 \pm 10
Focal Spot size (μm)	21.71 \pm 1.50	17.14 \pm 0.98	8.10 \pm 0.15	2.83 \pm 0.55	2.82 \pm 0.02	2.82 \pm 0.02
Diameter (μm)	42.08 \pm 4.91	45.77 \pm 3.49	46.15 \pm 3.39	46.63 \pm 3.78	46.48 \pm 3.05	47.89 \pm 6.65
Sag(μm)	6.58 \pm 0.57	5.69 \pm 0.18	5.52 \pm 0.41	4.39 \pm 0.22	3.41 \pm 0.28	1.32 \pm 0.11
Interstitial Roughness(nm)	3000.0 \pm 82.0	2950.0 \pm 83.0	1540.0 \pm 64.0	486.6 \pm 13.6	193.0 \pm 23.2	54.9 \pm 6.0
Lens Roughness(μm)	7.60 \pm 0.93	7.18 \pm 0.18	7.11 \pm 0.46	5.81 \pm 0.75	2.30 \pm 0.15	2.18 \pm 0.34

We observe in table 5.2 that the diameter is maintained almost constant over the range of temperatures tested, while the sag, decreases as temperature increases due to the displacement of the melted material. Regarding the interstitial roughness it was observed a significant reduction as the temperature increases. These two last parameters (sag and roughness) are related and respond to the material displacement from the top to the base of the microlenses during the reflowing treatment. While changes in microlenses sag modify the focusing capabilities, the surface mellowing contributes to the reduction of the stray-light typical of microlens arrays fabricated with laser direct-writing techniques.

Table 5.2 also shows a decrease of the focal length of the microlens from 620°C to 660°C. This behaviour is related with the reduction of the flatness of the microlens top. At 670°C it was observed a significant increase in the focal length with respect to that obtained at 660°C because of the reduction of the spherical aberration of the microlens obtained at 670°C. In relation to the spot size we observe a decrease as the temperature increases, what confirms the improvement in the microlens focusing power and optical quality.

Figure 5.23 shows different images of the focal plane of the microlens arrays reflowed at different temperatures which allows for a visual evaluation of the focusing properties of the fabricated microlens arrays. We observe how the focal spot sizes become significantly smaller and there is a better distribution of irradiance as the reflow temperature increases, providing a significant improvement in their focusing capability. It was also observed how the stray-light reduces as the reflowing temperature increases due to the roughness surface mellowing (see table 5.2), which leads to well-defined spots. Besides, the foci irradiance distribution of the microlens array becomes more regular.

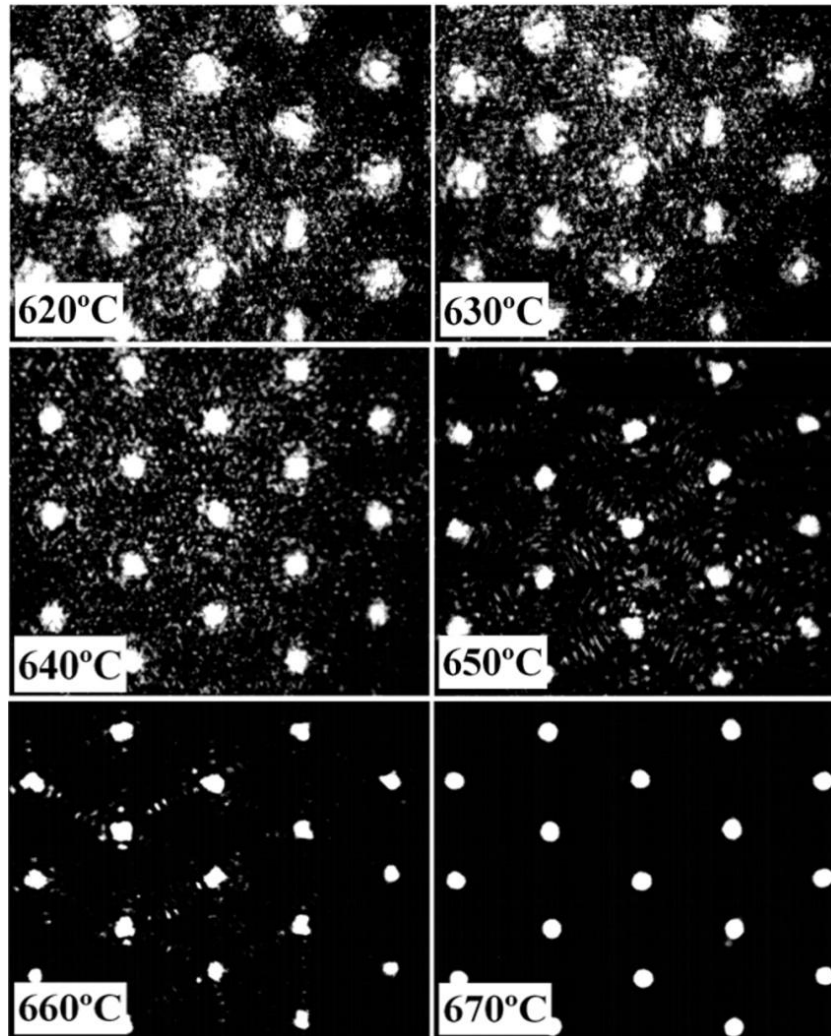


Figure 5.23 Images at focal plane of the microlens array after thermal treatment at different temperatures.

Figure 5.24 shows the variation on the focal irradiance distribution measured with the Thorlabs e-beam profiler, for the microlenses fabricated at different temperatures. This picture gives a visual perspective of the spot size and an approximate impression of the optical aberrations of the microlenses. Comparing the spots it is observed that they become narrower as the temperature increases, resembling the diffraction limited spot in case of 670°C.

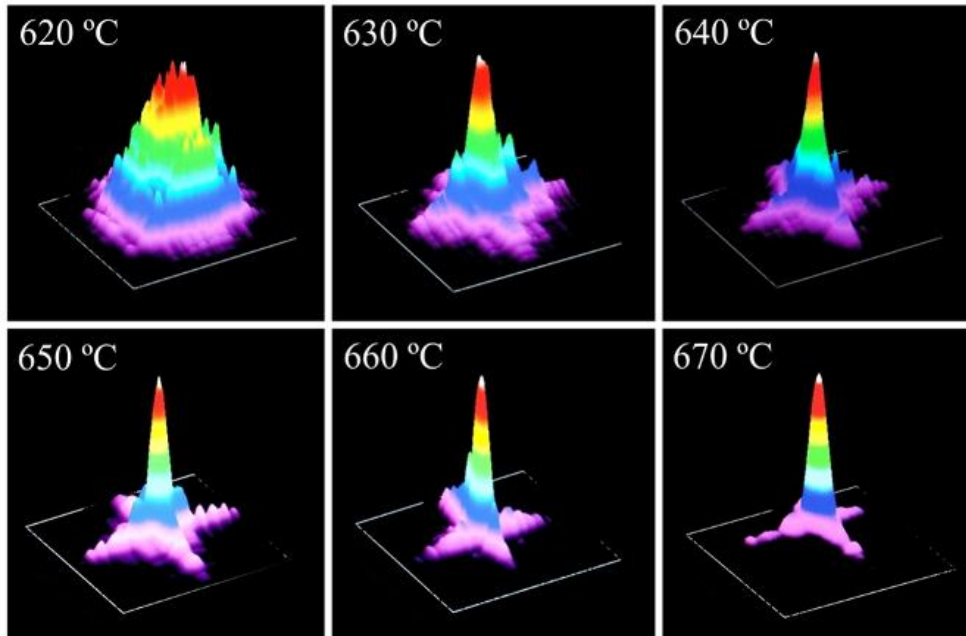


Figure 5.24 Measured intensity distributions at focal plane for microlens at different temperatures

5.5.2 Optical aberrations:

In this subsection it is going to be determined the optical aberrations of the microlens arrays fabricated at 650°C, 660°C and 670°C. We choose these elements because those obtained between 620°C-640°C were not significantly influenced by the reflowing process and present poor focusing capabilities.

3D Profiles of the microlens array were obtained with a confocal microscope SENSOFAR 2300 P|μ. The data were used not only for visualization purposes but also for analyzing the optical aberrations of the microlens array by calculating the modal coefficients of the expansion of the height data in terms of the orthogonal

Zernike polynomial basis. The first step for obtaining the Zernike coefficients is the identification of the pixels that belongs to the different microlenses in the 2D image. The procedure is as follows. First it was built the 2D confocal image. Then it was selected one of the microlenses and correlated with the microlens array image. The resulting image was thresholded in order to select those pixels with a high degree of correlation (which are close to the microlens centre) and then dilated to include most of the pixels that belongs to the microlens. Next we computed the centroid of these pixels in order to locate the centre of the microlens. Figure 5.25 represents the steps described above from the selection of the template to the identification of the microlenses.

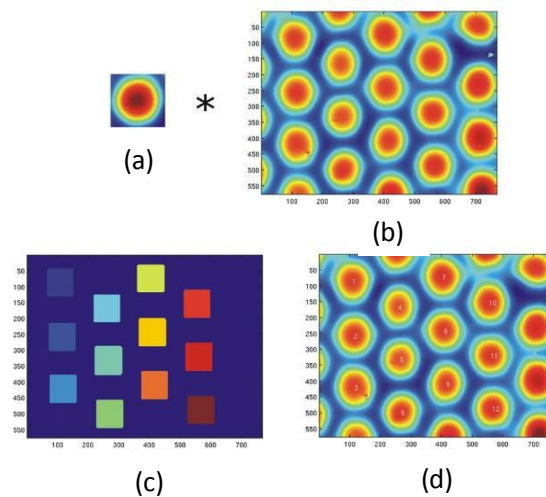


Figure 5.25 Image processing steps for microlens identification: a) template, b) actual microlens arrays, c) labeled masks and d) identified microlenses. * indicates image correlation.

After identifying the microlens it was measured their radius. To do that it was computed the gradient of the 2D microlens array image. By doing this it was enhanced the microlens border (Fig. 5.26). The radius was measured as the distance from the centre to the microlens border. This value was used to define the microlens pupil, inside which the wavefront analysis would be performed.

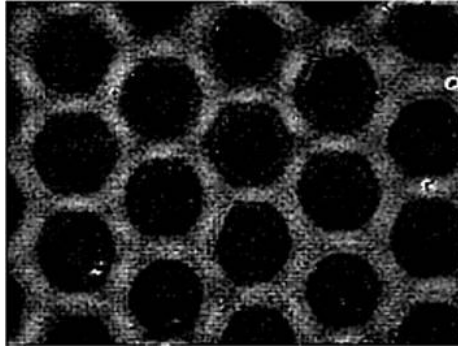


Figure 5.26 Border enhanced microlens array image.

The surface data inside each microlens pupil was expanded in a series of Zernike polynomials (defined according to the standard OSA-VSIA). We used this base of polynomials because it is orthogonal and some of the terms can be directly identified with common optical aberrations (Z_1 and Z_2 are prismatic terms, Z_3 and Z_5 are primary astigmatic terms, Z_4 is defocus, Z_7 and Z_8 primary comatic terms, and Z_{12} primary spherical (see refs. Malacara2007 and Thibos2002 for the identification of more Zernike terms). The modal coefficients were obtained through the common modal least squares estimation approach (see Eq. 5.1).

$$\mathbf{S} = \mathbf{Z}\mathbf{a} \quad \mathbf{b} = \left[\mathbf{Z}'\mathbf{Z}^{-1}\mathbf{Z}' \right] \mathbf{S} \quad \hat{\mathbf{S}} = \mathbf{Z}\mathbf{b} \quad (5.1)$$

where \mathbf{a} and \mathbf{b} are the column vector of actual and estimated modal coefficients, \mathbf{Z} is a $M \times N_s$ matrix (being M the number estimated modes and N_s the number of pixels inside the microlens pupil, with $N_s > 14000$ points in all cases), \mathbf{S} is the height data and $\hat{\mathbf{S}}$ is the estimated height.

Once we obtain the modal coefficients that allow us to express the surface data in terms of Zernike polynomials we are able to compute different magnitudes

currently used to evaluate the performance of optical elements. In particular we computed the Optical Path Difference (OPD), total root mean square error (RMS), the Strehl ratio (Sr), and the Depth of Focus (DOF).

$$\begin{aligned} \mathbf{OPD} &= (n-1)\hat{\mathbf{S}} & \mathbf{RMS} &= \sqrt{\sum \mathbf{b} \cdot \langle b_4 \rangle^2} \\ \mathbf{Sr} &= \exp - 2\pi(\mathbf{RMS})^2 & \mathbf{DOF} &= \mathbf{RMS} \frac{R}{\sqrt{3}b_4} \end{aligned} \quad (5.2)$$

where, R is the pupil radius, $\langle b_4 \rangle$ is the mean value of the defocus term over all the microlenses identified in the sample, and n is the refractive index of the soda-lime glass substrate ($n=1.523$). The modal coefficients are expressed in microns.

The optical aberrations were computed with respect to the microlens array mean parabolic optical path difference (which is related with the paraxial mean focus $\langle b_4 \rangle$). This procedure allows for analyzing the **OPD** aberration, Sr , and DOF variability among microlenses, and evaluating the performance of the complete microlens array.

Table 5.3 Mean root square difference between the microlens height data and the reconstructed surface (nm).

Number of Modes	Reflowing temperature		
	650°C	660°C	670°C
37	9.5	12.8	5.3
45	7.7	7.4	4.7
55	7.1	6.4	4.4
120	4.2	3.9	3.5

We reconstructed the surface of the microlenses in terms of the different number of Zernike polynomials (see table 5.3) observing that the difference between the

actual and estimated surfaces is smaller as the number of modes increases. This behavior is more noticeable for 650°C and 660°C. At these temperatures the microlenses experienced less deformation than at 670°C, what keeps more high order spatial frequency content in their surface, this is why we need more Zernike terms of higher order to describe properly the surface data of these elements. In all the cases the surface data estimated with 120 modes provides a residue of the order of the surface roughness of soda-lime glasses (~ 5 nm) see table 5.2, being this level of accuracy achieved with just 37 modes for the element reflowed at 670°C. This behaviour shows the effectiveness of the reflowing process at this temperature.

In figure 5.27 (a) and (b) we show a 3D representation of the actual and estimated height data of one of the microlenses fabricated at 670°C, respectively. The reconstructed surface was obtained with 120 Zernike polynomials. Fig. 5.27(c) shows the difference between them.

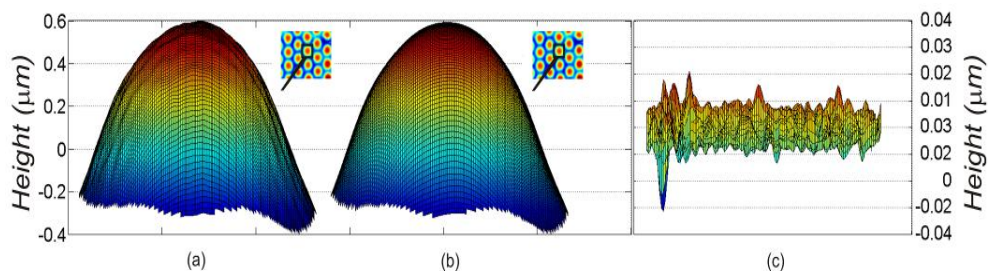


Figure 5.27 (a) Confocal image, (b) Zernike reconstructed image, and (c) surface difference at one microlens. Data extracted from the microlens array reflowed at 670°C.

Figure 5.28 depicts the profiles of the original and reconstructed surfaces of one microlens for the arrays manufactured at the different temperatures. The degree of agreement between both profiles remarks that 120 Zernike polynomials are enough for representing the surface of the analyzed microlenses.

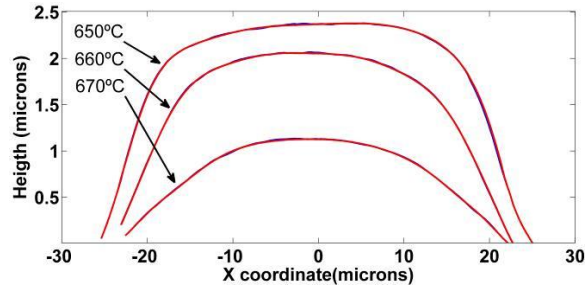


Figure 5.28 Original (– blue) and reconstructed (– red) profiles of one microlens of the arrays reflowed at 650°C, 660°C and 670 °C.

Fig. 5.29 reflects the absolute value of the mean value (Fig. 5.29a) and the standard deviation (Fig. 5.29b) of the estimated modal coefficients obtained for the surface reconstruction of the microlens arrays fabricated at the different temperatures. The mean value and standard deviation were computed over the microlenses identified on each array. We present only the coefficients from $j=1$ to $j=45$ (up to 8th order excluding piston term), for a better visualization of the figure.

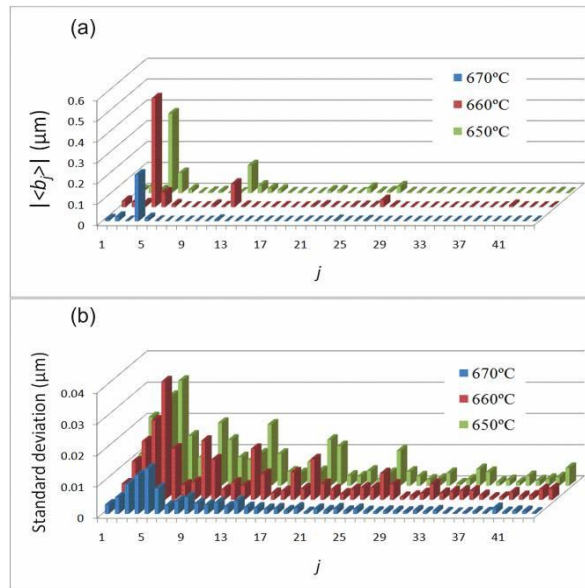


Figure 5.29 Absolute mean value and standard deviation of the estimated modal coefficients for temperatures 650°C, 660°C, 670 °C. j is the coefficient index.

Fig. 5.29(a) reveals how the shape of the microlenses evolves from a significantly aberrated shape with important amounts of primary astigmatism (Z_3 and Z_5) and spherical aberrations (Z_{12}) at 650°C to a parabolic shape at 670°C. Besides, we see in Fig. 5.29(b) a reduction in the standard deviation of all the Zernike coefficients as the reflowing temperature increases. So, we got two remarkable results: (1) thermal treatment contributes to the reduction of the microlens optical aberrations; (2) and to the homogeneity or similarity of the microlenses shapes, two important questions for microlens array fabrication.

The optical aberrations are computed with respect to the mean microlenses defocus term. We show in Fig. 5.30 the 2D images of the computed aberrations in wavelength units. We observe that at 650°C and 660°C the dominant aberration is the primary spherical aberration, being at 650°C two times higher than at 660°C (notice the difference on the image colormaps). However at 670°C the spherical aberration (although present) is of the order of the astigmatic terms, what makes the OPD maps more elongated.

Clearly, this fact is consequence of the cylindrical shape of the laser-ablated posts which becomes more parabolic thanks to the surface tension of the melted element as the reflowing temperature increases.

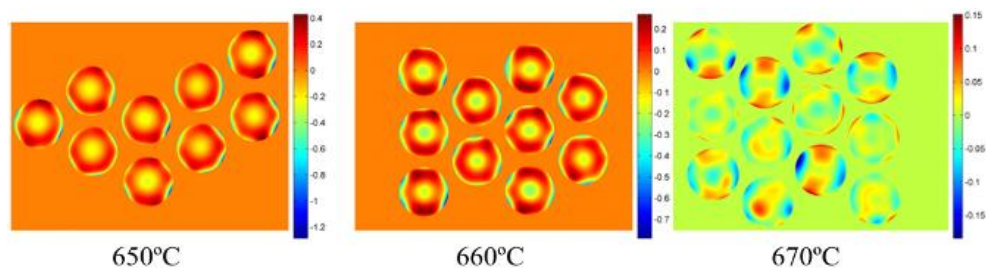


Figure 5.30 OPD of the microlens arrays obtained at different reflow temperatures. The maps are in wavelength units.

In Table 5.4 we present the mean value and standard deviation of the parameters, defined in Eq. 5.2, used to characterize the optical quality of the fabricated microlens arrays: *RMS*, *Sr*, and *DOF*. The mean value and standard deviation were computed over all the microlenses identified on each microlens array.

Table 5.4 Mean value and standard deviation of the optical parameters.

Reflowing Temperature	RMS (waves)		Strehl		DOF(μm)	
	mean	Std	mean	std	mean	std
650°C	$\lambda/5$	$\lambda/56$	0.2183	0.0606	43.1145	7.9932
660°C	$\lambda/7$	$\lambda/73$	0.4406	0.0664	20.5214	3.0115
670°C	$\lambda/28$	$\lambda/77$	0.9475	0.0352	16.4387	5.7627

It can be observed in table 5.4 the influence of the reflowing temperature on the quality of the fabricated microlens array. Again 670°C provides the best results with an RMS of the total aberration of the order of $\lambda/28$ and variability between microlens of $\lambda/77$, $Sr=0.9475$ with a variability of 0.0352 (notice that $Sr=1$ corresponds to the diffraction limited case), and $DOF = 16.44 \mu\text{m}$ with a variability of $5.76 \mu\text{m}$. The results presented in table 5.4 are comparable to those obtained by other researchers and fabricating methods [Gomez2008, Albero2009].

One question to remark is the regularity of the fabricated arrays. Focusing our attention on the standard deviation of the different parameters, we notice that their change from 650°C to 670°C is small in comparison to the change of their absolute value. This tells us that the microlenses of the array are very similar between them and this resemblance is almost independent of the reflowing temperature. This fact remarks the goodness of the laser-direct ablation

procedure used to obtain all the initial cylindrical posts that promote the microlens array.

Both Sr and DOF are magnitudes related with the focusing capabilities of the array. The similarity between foci shape (size and maximum irradiance) and DOF is very important in many applications of microlens arrays (for example in those applications based on lateral displacements of foci centroid determination as Hartmann-Shack wavefront sensors), and our fabricated arrays present this characteristic. Notice the small standard deviation of the Sr and DOF . This question can be also observed in Fig 5.23 where we present an image of the focal plane of the microlens arrays.

5.5.3 Microchannels.

Microfluidics has experienced the rapid development of new methods of fabrication, and of the components, the microchannels that serve as pipes, and other structures that form valves, mixers and pumps, that are essential elements of microchemical lab-on-a-chip devices. In this context, the developed fabrication process is used to demonstrate its capability for the fabrication of microfluidic microchannels.

The experiment were carry out at a commercial soda-lime glass using a Nd:YVO₄ laser. The power, repetition rate, wavelength and pulse width of the ns laser were 4 W, 10 kHz, 1064nm and 20 ns, respectively. Scan speed of 50mm/s were used. Figure 5.31 shows the microchannel obtained by laser direct write.

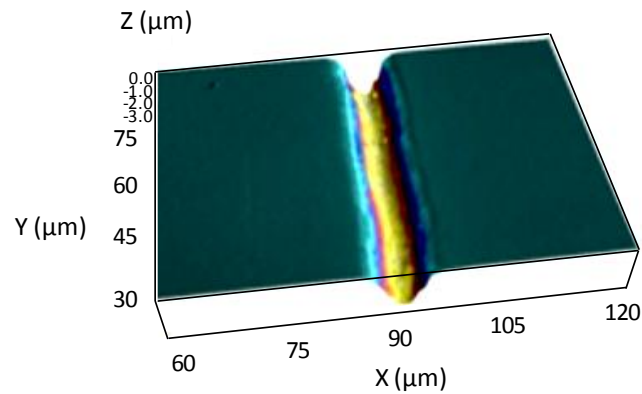


Figure 5.31 3D confocal image of a microchannel fabricated by direct laser write.

The depth and the surface roughness of the etched glass substrates were measured using a Confocal microscope SENSOFAR 2300 PL μ . The resulting channel exhibit a roughness of 640 nm, diameter of 8 μm and height of 3 μm . After laser direct write a thermal treatment in Heraeus mufla oven was applied at different heating times. Figure 5.32 shows the evolution of the topographic profile of the fabricated microchannels at different temperatures.

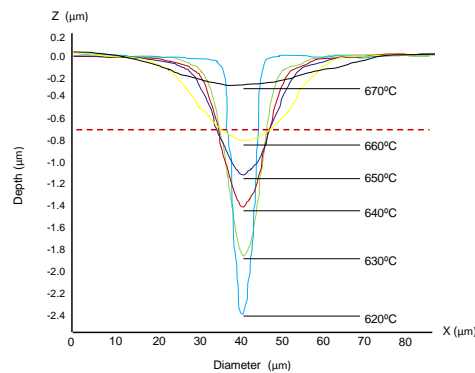


Figure 5.32 Cross-sectional profile of the microchannels obtained at different thermal reflow temperature (620 $^{\circ}\text{C}$, 630 $^{\circ}\text{C}$, 640 $^{\circ}\text{C}$, 650 $^{\circ}\text{C}$, 660 $^{\circ}\text{C}$ and 670 $^{\circ}\text{C}$).

It can be appreciated in figure 5.32 that for temperatures of 620 $^{\circ}\text{C}$ or lower, there was almost no change in the surface shape and for reflowing temperature higher

than 670°C, the initial shape surface profile becomes flat, so microchannels obtained by laser direct-write tend to disappear. Figure 5.3 shows 3D confocal images of microchannels fabricated at different reflow temperatures.

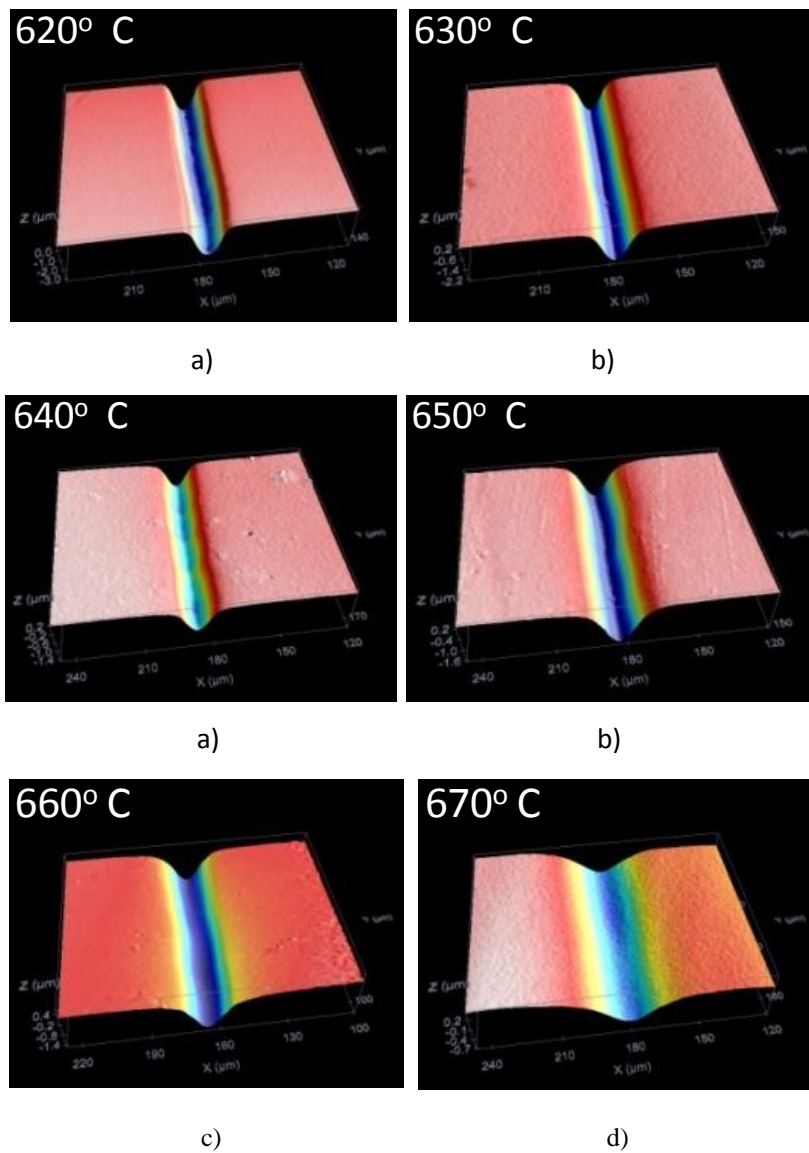


Figure 5.3 Confocal images of microchannels obtained after thermal treatment at different temperatures

It can be appreciate in figure 5.33, that the diameter increase and the height decrease with the temperature. For a temperature of 630°C there is a smooth variation on shape, which is in concordance with the initial design, but the roughness is modified considerably, which is of great interest for microfluidics applications. The surface roughness is understood as an irregularity from a smooth surface caused during a fabrication process. These irregularities appear as microscopic holes and bulges from the expected (smooth) surface. The surface roughness can be defined as a vertical deviation between the highest bulge and deepest hole within a certain area (Fig. 5.34).

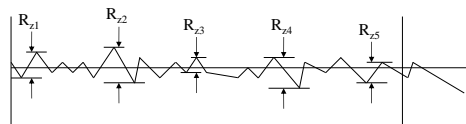


Figure 5.34 Surface Roughness can be defined as an average vertical deviation between the highest bulges and lowest holes.

An average surface roughness (for now on just surface roughness) can be specified with Eq. (5.3).

$$R_z = \frac{1}{n} (R_{z1} + R_{z2} + R_{z3} + \dots + R_{zn}) \quad (5.3)$$

A smooth, optimal microfluidic channel has the specific resistance related to the geometry. The surface roughness on the wall of the channel increases by decreasing the flow rate, so the change of hydraulic resistance is proportional to the change of surface roughness. For determining the quality of the microchannels fabricated, we determine the roughness at the bottom of the channels. Table 5.4 shows the evolution of roughness with temperatures between 620°C and 670°C.

Table 5.4 Comparative of roughness evolution with thermal reflow.

Temperature	Ra
Ra Glass surfaces	3.68 nm
Ra laser ablation	640 nm
620°C	125.14 nm
630°C	57.15 nm
640°C	39.45 nm
650°C	29.40 nm
660°C	16.43 nm
670°C	7.35 nm

The initial roughness for unprocessed glass was 3.68 nm, after thermal process at 670°C its decrease till 7.35nm, this value is near to optimal value for unprocessed glass although there is an important morphological change. The best result was obtained for 630°C, it maintains the initial shape and a roughness of 57.15nm, which is a very good value for microfluidics applications on glass [Malalahalli2004]. Moreover the roughness average (Ra) at the bottom of the microchannels before thermal treatment was $Ra = 640$ nm and after thermal treatment at 670°C was $Ra = 7.35$ nm, this is in the order of the unprocessed soda-lime glass surface, which means that the quality of surface is much better after thermal treatment.

In order to fabricate different devices configurations, a study of the evolution of depth and diameter with the number of laser pass over the same place was done. To assess the evolution of the depth of the channels versus number of passes N, the edge of the trench is extracted using image processing after each pass, with successive passes super- posed onto a composite image to study the influence of N while keeping the other laser parameters constant.

Figure 5.35 show the evolution of depth and diameter varying the number of laser passes.

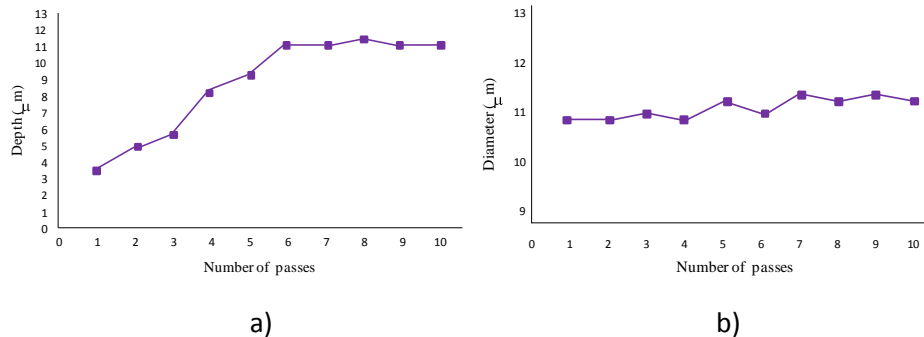


Figure 5.35 Evolution of a) depth and b) diameter varying the number of laser passes.

It is evident from figures 5.35 that the channel aspect ratio $\alpha = h/d$ varies with the number of pass. The channel width d reaches its saturation value after 5 laser passes, increasing just around 200 nm per laser pass and varying only 1 micron after 5 passes, then is maintained almost constant. In contrast, the ablation height h changes dramatically with increasing number of pulses, reaching a saturation value after 6 pass, presenting an increase of 1 micron per laser pass, till it reach a height of 12 microns , after it maintains constant. This behavior can be related with the non-evacuation of debris generated during laser ablation from the bottom of the channel.

For studying the microfluidics capabilities of our technique, including the capability to form complex cross- sectional shapes,we center our study on the fabrication of microchannels with different configurations. The main inconvenient of using a laser direct write technique for fabricating microchannels are in the junctions since the propelled material of the subsequent channels. is deposited on the existing microchannel. Figure 5.36 shows different examples of microstructures fabricated for microfluidic purposes.

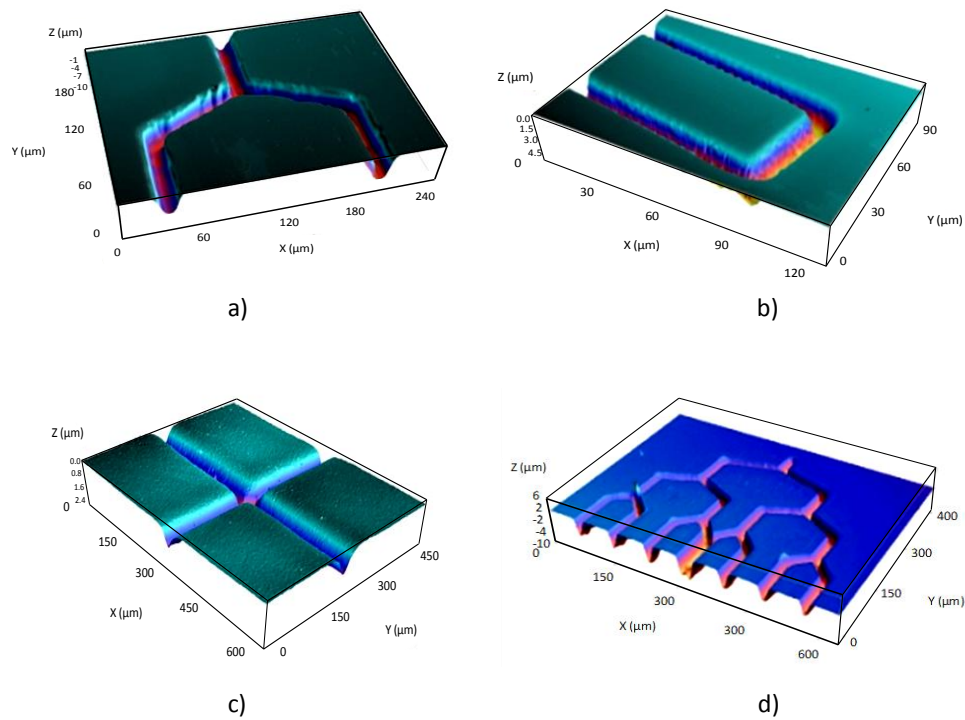


Figure 5.36 3D Confocal images microchannels at different configurations.

Microfluidics deals with the precise control and manipulation of fluids that are geometrically constrained to a small scale. These devices are used in microanalytical systems such as in capillary electrophoresis for DNA and protein separations [Khandurina2000, Liu2001, Bousse2003], as miniaturized channels for microfluidics [Stone2001, Whitesides2001], and as biochemical reactors and sensors [McCreedy2000]; future applications include cell biology and tissue engineering [Chiu2000]. Typical methods for microstructuring glass includes electron beam lithography, photolithography, and wet and dry etching [Chen2001]. Although these techniques provides robust and high-quality microfluidic systems, the techniques used for fabrication are often time consuming and requires sophisticated equipment located in clean rooms.

Fabrication of complex microfluidic devices on glass quickly, easily and inexpensively is a topic of great interest. In this context, the advantage of the process we propose comes from the simplicity and speed of the pattern transfer into the substrate, even in the production of more complex structures as demonstrated in figure 5.36. The ability to fabricate glass microfluidic systems using the technique presented in thesis makes glass attractive for many applications in which speed and economy of production are desired.

CHAPTER 6

APPLICATIONS ON SURFACES MICROSTRUCTURING

In this chapter the structuring capabilities of microlens arrays for micro-patterning surfaces is presented. Consequences of the material processing over the microlens such as damage produced by the spelled material will be analyzed. Solutions to avoid the damage will be done, in particular the Talbot effect as a tool to overcome this problem will be presented.

6.1 Introduction and motivation.

The modification of surfaces at micrometer and sub-micrometer scales is considered to be a key future technology. This has led in recent years to a huge interest in the generation of micro and nanometer structures on surfaces. Various forms and techniques of surface texturing were developed over the years [Ming-Hsien2003, Sandip2009, Etsion2005, Duarte2008, Razzaque2008]. Among them, laser ablation has the advantage of great versatility, since it can be adapted to produce a wide range of structures. Lasers have also demonstrated utilization in rapid surface microstructuring and modification of materials to generate the textured surface features without significantly affecting or altering the properties of the bulk material. These lasers can therefore handle surface microfabrication on material substrates reliably, easily, and at high throughput.

Most of the laser-assisted microstructuring studies deal with the selective ablation of material to produce micrometer and sub-micrometer features for diverse applications. Laser texturing of surfaces for enhancing tribological performance has demonstrated significant improvements in load capacity, wear resistance, friction coefficients, etc. In such tribological applications laser textured grooves or pockets act as lubricant reservoirs and increase the lubricant film thickness on the sliding surfaces [Dumitru2000, Eskin2005].

Recently, laser-assisted surface microstructuring of porous ceramic materials have attracted significant interests from the viewpoint of improving the surface properties by generating geometric surface features [Hao2003, Hao2004, Hao2004b, Hao2004c, Harimar2004]. To realize the full potential of the laser-assisted surface microstructuring of ceramics for applications necessitating rapid and precision control of geometric features, the efforts have to be focused on the implementation of rapid manufacturing techniques

In this context, micro-optics plays an important role in various industrial production processes, like micro-electronics, laser micro-machining and materials processing. Microlens arrays offer a unique enabling technology in critical domains such as sensors, communications, metrology, and medical imaging, often providing solutions where other technologies prove unsuitable, unwieldy or cost prohibitive. The use of microlenses is particularly well suited for manufacturing, optimization of laser beam delivery and improvement of production efficiency with the intention of cost reduction. Is in this framework where we propose the use of microlens arrays for surfaces micro-patterning of materials.

6.2 Structuring capabilities of microlens arrays.

In the work presented in this thesis it was demonstrated the influence of Sn impurities over the ablation process of soda-lime glass. These impurities led to a reduction of the ablation threshold of glass, which makes the soda-lime glass suitable for fabricating elements using relatively nanosecond low power lasers. On the other hand, when we use the microlens for microstructuring surfaces materials the main disadvantage arises also from the impurities since it is possible to damage the glass using not very high fluences. Another damage mechanism comes from any imperfection or debris generated during the surface texturization performed with the microlens array, which may impinge and be deposited at the microlens surface, and acts as absorbing center leading to the ablation of microlens array and its subsequent deterioration.

In order to avoid the damage of the microlens the optimum laser parameters have been selected. Low energies per pulse ($\approx 60 \mu\text{J}$) and high repetition rates (50 kHz) have been used, increasing the interaction time and the number of pulses needed to generate the hole. Although this can be improved by using low absorption and high quality optical materials, as the microlens work well at low

energies, the low cost of the material and fabrication process make this technique attractive compared with other ones.

6.2.1 Surface microstructuring.

The experimental setup for testing the structuring capabilities of surfaces materials of microlens array is shown in figure 6.1. The microlenses used have a diameter of 40 μm , and focal length of 510 μm . The microlens array is placed on a precision stage, which is moved until the focus spot is located over the material that we want microstructure. The targets were irradiated with Nd:YVO₄ lasers operating at 1064 nm and 532 nm, and at the suitable laser parameters chosen in each case and exposure time determined as function of the material (see below). A spatial filter is placed between the laser and the microlens array to select the appropriate part of laser beam to be used. The working distances 510 μm .

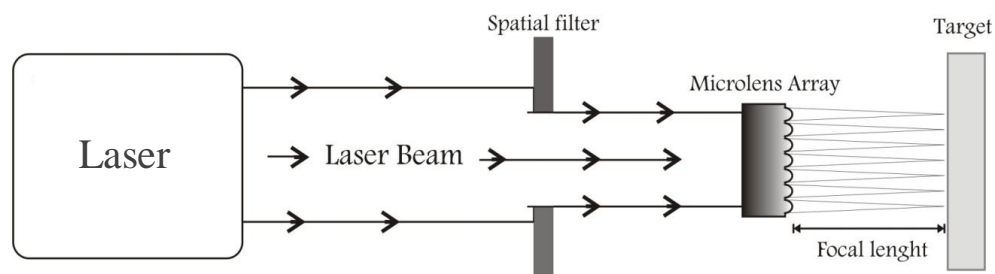


Figure 6.1 Setup for microstructuring of surfaces material using microlens arrays.

Using the experimental setup described in figure 6.1, a 200x200 array of holes is obtained on stainless steel, copper, aluminum and plastic materials. Each hole corresponds to the interaction of the light at the focal plane of the microlens over the target. The choice of each material and laser wavelength combination has

been made in terms of the optimal optical absorption of each material. The main advantage of this kind of direct laser technique is that a large number of identical structures can be produced simultaneously, leading to a highly efficient process. The topography of the holes fabricated was analyzed using a confocal microscope and scanning electron microscope. Figure 6.2 presents the results obtained by exposing a polymer sheet of PMMA to 532 nm laser wavelength using the microlens arrays. The laser parameters used were 50 kHz, 1.2 W and exposing time of 2 seconds.

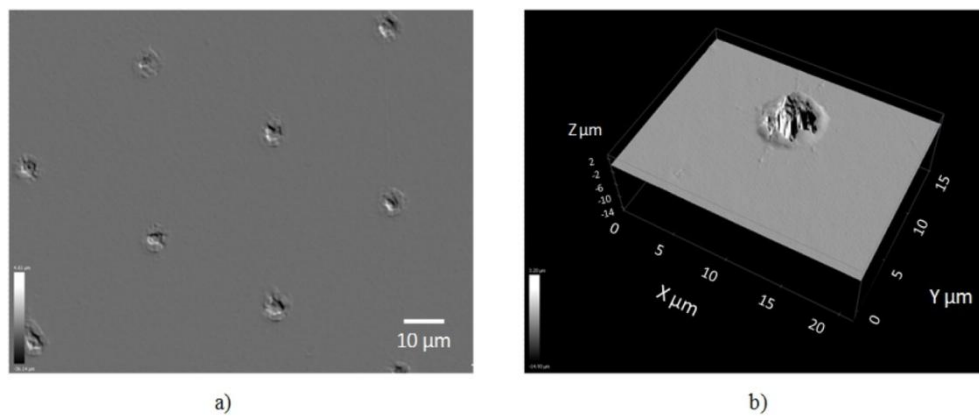


Figure 6.2 a) Confocal image of the array of holes fabricated over polymer and b) detail of one hole of depth $1.4\mu\text{m}$ and diameter $5\mu\text{m}$.

As it can be appreciate in figure 6.2, an array of holes was obtained by exposing a polymer sheet of PMMA to 532 nm laser wavelength using the microlens arrays. The diameter of each hole was $5\mu\text{m}$ and the height $1.4\mu\text{m}$.

In figure 6.3a) and 6.3b) we present and array of holes fabricated by exposing a sheet of stainless steel to 1064 nm laser wavelength using the microlens array. The laser parameters were 50 kHz, 8 W and 2 second exposing time. Figure 6.3c) and 6.3d) shows the array of holes fabricated over aluminum and figure 6.3e) and

6.3f) over copper using the same procedure and laser parameters. An array of holes and a detail of one hole are presented for each material.

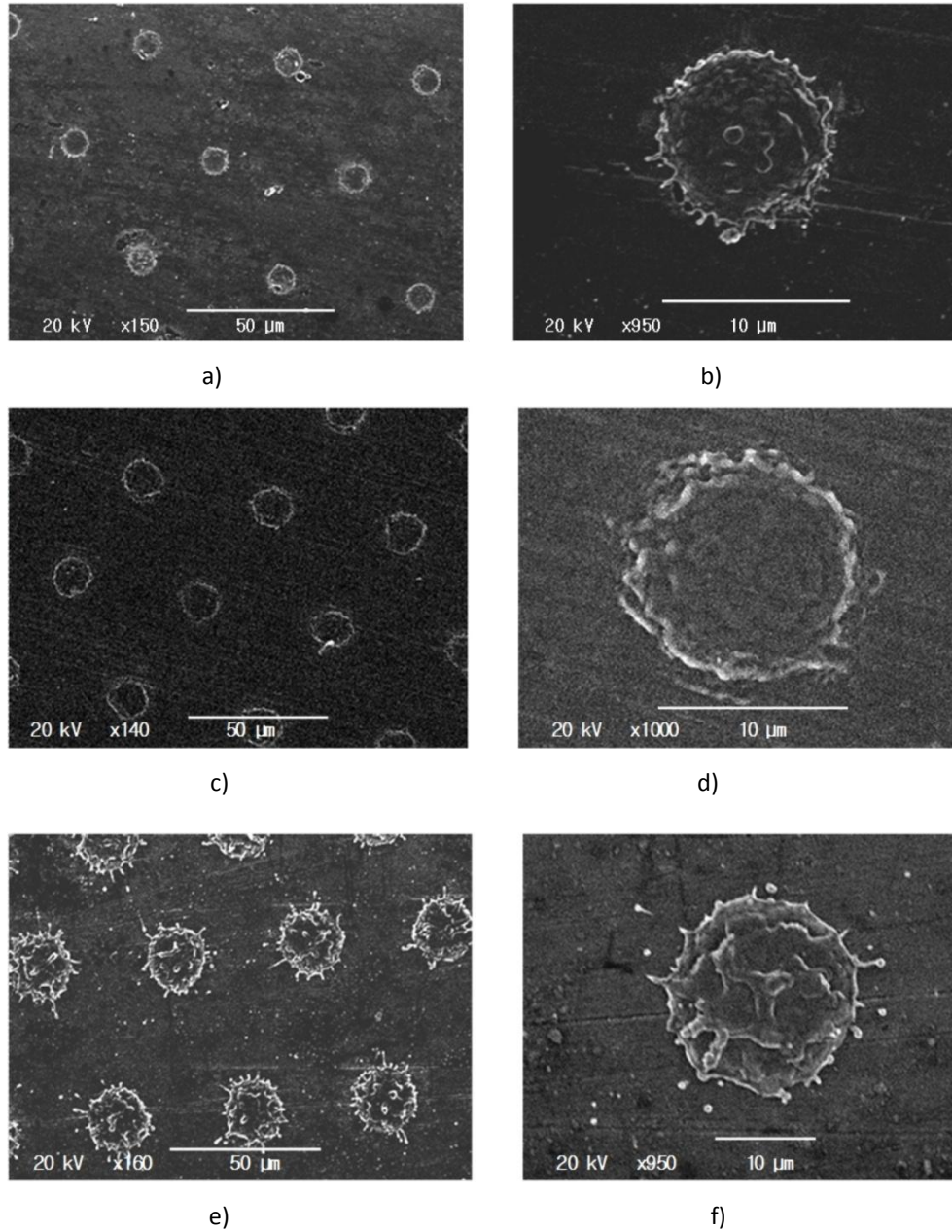


Figure 6.3 a) SEM image of the array of holes fabricated over a) and b) stainless steel, c) and d) aluminum and e) and f) copper.

Since the absorption of the material to a specific wavelength determines the final mark in the material, different results have been obtained. The smallest diameter of 8 μm and height of 2.2 μm was obtained for stainless steel. The diameter of the hole fabricated on copper was 17 μm and the height 4.1 μm . In the case of aluminum values of diameter 13 μm and height 2.4 μm were obtained. Although the laser parameters and material absorption determine the final mark, it was also realized that of crucial importance is the fact of placing the samples just at focus of the microlens. This is particularly important due to the short depth of focus of the microlens array.

6.2.2 Selective removing of thin films.

The use of microlens arrays to selective elimination of thin films is demonstrated in this section. To this purpose, a soda-lime glass is covered with aluminum thin film of thickness 100 nm, after the microlens arrays have been irradiated by an IR laser with the sample placed at different distances from the focal length of microlens. The laser parameters used were 4 W, 50 kHz, 1064 nm and exposing time 2 seconds

Figure 6.4 shows an image of patterns obtained by eliminating thin metal film on glass. In figure 6.4a, an array of holes generated by placing the sample just at the focus of the microlens is shown. Figure 6.4b depicts the pattern when the samples were placed out of focus. By separating the sample far from the focus, the interaction zone is enlarged and it is possible to eliminate all the thin film from the glass (see figure 6.4c); the fluence in the area covered per each microlens at this height is under the fluence threshold for the glass which results in the elimination of the metal film without damaging the glass.

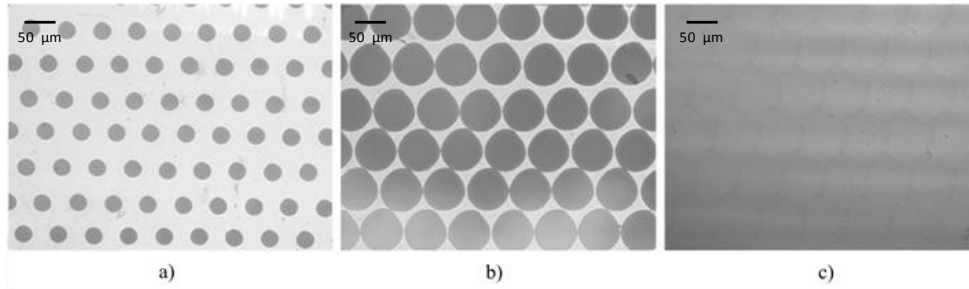


Figure 6.4 Images of selective elimination of aluminum layer over glass for a) the sampled placed at focus of microlens array, b) out of focus and c) far from the focus.

6.2.3 Removing of contamination layers.

Additionally, to the fabrication of micro-holes and selective thin metal film removing, using the microlens array and the suitable laser parameters (1064 nm, 4 W, 50 kHz and exposing time 2 seconds) it was possible to clean rusty layers without affecting the bulk of the sample. Figure 6.5 shows the rust iron sample before and after laser exposure.

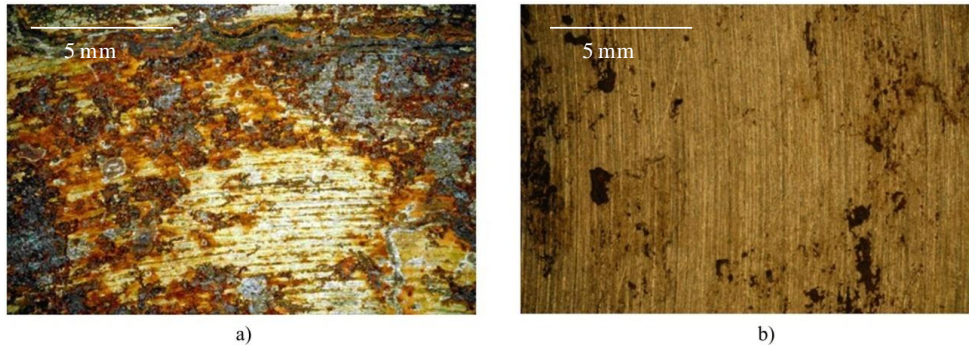


Figure 6.5 a) Rusty iron sample and b) the sample piece of iron after laser exposure using the microlens arrays.

The sample of iron contaminated with rust was placed in a positioning platform, located out before the focus of the microlens array, and exposed during 2 seconds

while the platform was moved in circles in the X and Y plane. Since small quantities of waste material were generated during laser exposure, the cleaning process was assisted with an evacuation air system. As we can see in figure 6.5b, the rust was eliminated over the surface, but not in some parts where the iron was previously damaged by oxidation.

6.3 Talbot effect.

It has been demonstrated the structuring capabilities of microlens arrays over a variety of different material, such as stainless steel, aluminum, copper and polymer. The microlenses present a problem of durability due to their interaction with the material expelled from the substrate during the ablative process. To avoid the rapid contamination and deterioration of microlens, it was realized that the best option is to separate the substrate as much as possible from the microlens array, which is conditioned by the short focal length of microlens array. To overcome this, we propose the use of the Talbot effect, which consists in the formation of self-images of periodic functions at planes depending on the wavelength and the period of the structure [Patorski1989, Berry1996]. This effect has a big number of applications on metrology [Cvavel1984, Leger1984], spectrometry [Ozakas2006], nanolithography [Solak2006] among others.

When the periodic structure is an array of microlenses, illumination causes the appearance of foci. We can consider these foci as the periodic object in the Talbot effect. Talbot images have different period and magnification [Belsod1997, Stuerzebecher2010] depending on the distance to the original periodic object. When an array of microlenses is used as periodic object, Talbot planes are found at distances z from the matrix defined by Eq. (6.1) [Besold1997]:

$$z = f + n \cdot z_T \quad \text{being} \quad z_T = \frac{2a^2}{\lambda} \quad (6.1)$$

where f is the focal length of the microlenses, n the order of Talbot plane, z_T is the Talbot distance, a is the period of the microlenses, and λ the wavelength of the incident light. Figure 6.6 shows several the Talbot planes obtained at different distances from microlenses when illuminating the microlens array with a laser ($\lambda=630$ nm).

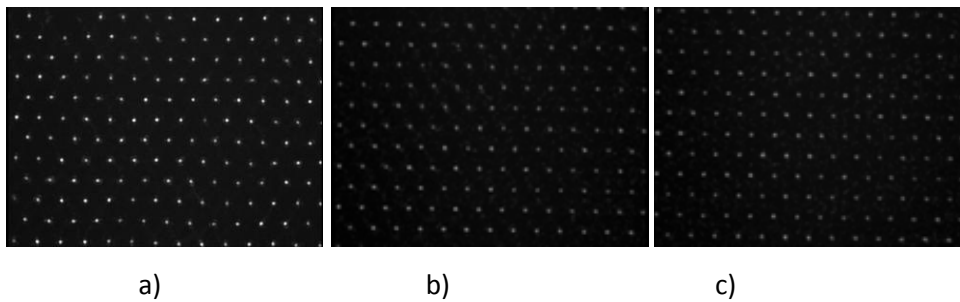


Figure 6.6 Image obtained at different distance from microlens arrays a) 510 μm , (focus of microlens), b) at 15,14 mm (first talbot image, c) 31.65 mm (second talbot image). Laser wavelength 630 nm.

By illuminating the microlens array with a laser beam, we can use the resulting Talbot images to structure surfaces with the advantage of creating a multi-structuring with great versatility in design (due to the dependence of the pattern replicated with the Talbot plane being exploited) and increasing the working distance (distance between microlens array and substrate) in order to avoid deterioration of the microlenses caused by the particles spelled from the substrate, and therefore increasing its useful life.

To this purpose we have developed a system for surface multi-structuring (presented in Fig.6.7). It consists of a Nd: YVO₄ Q-switch that works with the

following parameters ($\lambda = 1064 \text{ nm}$, pulse width 20 ns at 10 kHz, $M^2 < 1.2$) in combination with a galvanometer and a flat field lens of focal length 120 mm., The microlenses array is placed between the laser and the substrate. In this case we used microlens with diameter 60 μm to have a distance enough between the Talbot plane and the microlens array for avoiding array damage. The substrate, on which we perform the microstructure, is placed in the focal plane of the field lens, whereas the microlens array is positioned such that one of the Talbot planes matches on the substrate (see the setup in fig.6.7).

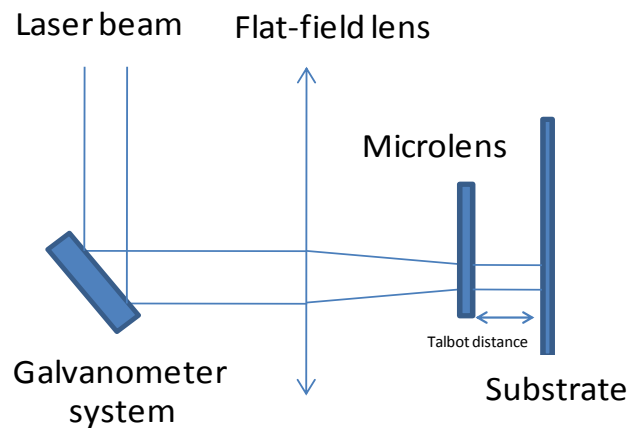


Figure 6.7 Experimental setup for microstructuring a material using the Talbot effect.

The laser parameters used in this case were: pulse repetition rate of 15 kHz and energy per pulse of 450 μJ (this energy level does not damage the microlens array).

The Talbot plane selected for microstructuring (considering that in this case the laser wavelength is 1064 nm) corresponds to the second Talbot image, corresponding to a length of 14.70 mm from the microlenses.

Figure 6.8a and 6.8b shows one of the multistructuring results obtained on a Cr foil, placing the microlens array substrate at 14.70 mm of the sample, which corresponds to the second Talbot image. Figure 6.8c and 6.8d shows the microstructuring results by placing the Cr foil at the focal length of the microlens arrays (1.180 mm). The targets were irradiated with Nd:YVO₄ lasers operating at 1064 nm. The laser parameters used were 30 kHz, 5 W and exposing time of 5 seconds.

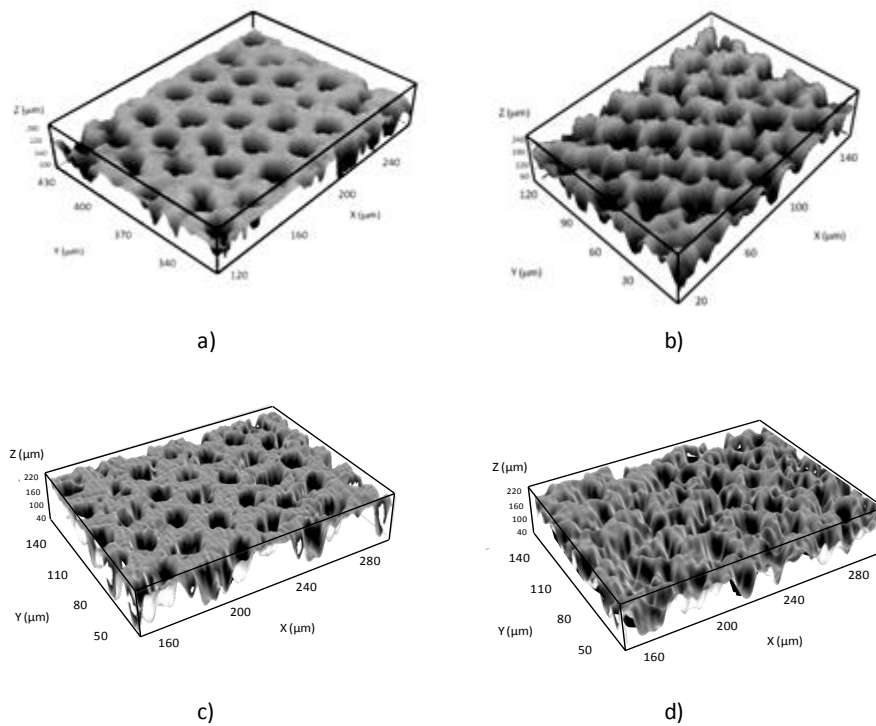


Figure 6.8 Cr foil microstructured using the microlens array by a) Talbot effect and 1 pass of laser beam, b) Talbot effect and 2 passes of laser beam, c) placing the CR at focal plane of microlens and 1 pass and c) at focal plane and 2 passes.

It can be appreciate in figure 6.8b and 6.8d that by applying two times the laser treatment, the structure obtained at surface of Cr foil makes more irregular due

to the increase of holes diameter with the second pass. The Talbot effect allows us to increase the working distance of around 1 cm respect to the length used for microstructuring if we did not use a Talbot plane, thus avoiding any damage of the microlenses by material generated during the ablation process.

Figure 6.9a shows a 3D confocal image of the microlens array after microstructuring materials using the Talbot effect and figure 6.7b a microlens array after microstructuring materials at the focal plane of microlens.

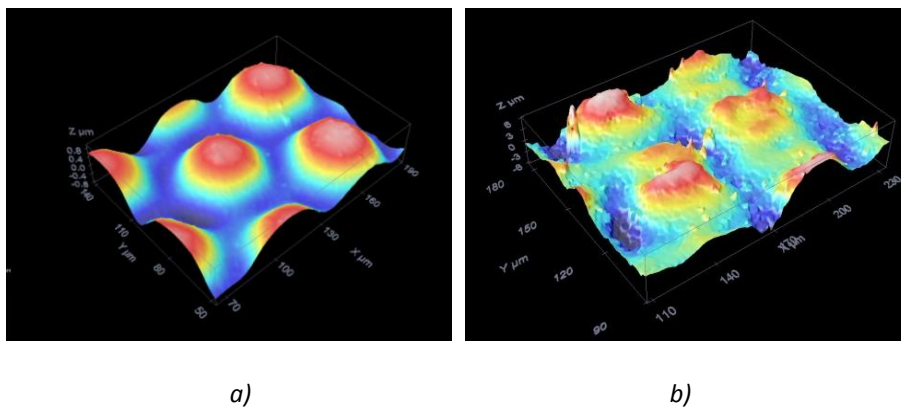


Figure 6.9 a) 3D confocal image of the microlens array after microstructuring materials using the Talbot effect and b) a microlens array after microstructuring materials at the focal plane of microlens.

It can be appreciate in figure 6.9a that using the Talbot effect the microlenses do not suffer damage at surface. On the other hand, working at focal plane (fig. 6.9b), the particles spelled from the target are deposited at surface of microlens, leading to the damage of microlens arrays.

CONCLUSIONS

In this chapter the conclusion emerged from the works presented in this thesis are presented.

Conclusions

From the work realized in this thesis it has been emerged the next conclusions:

- A new method for fabricating microlens and microfluidic microchannels on soda-lime glass has been developed. It consists of a combination of the laser direct write technique for fabricating the promoting glass structures, a wet chemical etching to remove the roughness generated during laser ablation and a thermal treatment for reshaping and or improving of the optical and morphological qualities of the generated microlens and microfluidic microchannels.
- It has been showed the suitability of the developed method for glass microstructuring.. The use of pulsed nanoseconds lasers for the laser direct write, includes the benefits of using lasers commonly implemented for laser processing of materials applications, which makes the technique presented in this thesis highly competitive compared with other techniques commonly used on glass microstructuring.
- It has been demonstrated the use of IR nanosecond lasers as a tool for microstructuring glass materials, which due to the low absorption at IR, are typically machined with excimer laser or solid state lasers working in the UV wavelength.
- Related with the chemical etching process, it has been revealed as a suitable process for removing the debris deposited over the glass after laser ablation, reducing the roughness and eliminating the secondary

postunablated due to the microlens packaging. Although the chemical etching has been analyzed for different microlens diameters, the best results were obtained for microlens of diameter 140 μm . In this case, the secondary posts generated during laser ablation, which are bigger in the case of microlens of diameter 140 μm , interact with the material of the main cylindrical post during the material displacement produced during the thermal treatment, leading to an irregular distribution. It has been showed that without using the chemical etching it was not possible to obtaining microlens of diameters higher than 140 μm . For diameters below 140 μm does not present any significant result that justify the use of acid fluorhidric.

- The influence of the thermal treatment, which was applied at a range of temperatures between 620°C and 670°C, revealed two different ways to proceed, at high temperature it reduces the roughness up to the same level presented by the glass before being processed, increasing the optical quality but with a significant change of shape (interesting for obtaining good microlens). At low temperature it keeps the shape and decrease the roughness (appropriate for fabricating microchannels).
- It has been showed that when the thermal treatment was applied, the shape of the microlens evolves from a flat-top post to a quasi-parabolic profile as the temperature treatment increases. In the case of 620°C some irregularities in the surface generated by the laser ablation step were observed. For temperatures of 630°C and higher these irregularities disappear. The diameter of the microlenses is maintained almost constant over the range of temperatures tested, while the sag decreases due to the redistribution of the material from the top sides of the trench to the

bottom of the crater. Temperatures out of this range were also analyzed; it was found that for values lower than 620°C there were almost no significant changes in the surface shape. By contrast, for temperatures higher than 670°C and 2 hours of thermal treatment, the initial array of cylindrical surface profile becomes flat, so the microlenses obtained by laser direct-write disappear.

- Using the laser-direct write technique, the chemical etching and the thermal treatment it was possible to fabricate microlens of diameters 40 μm , 60 μm and 140 μm with focal lengths of $510\mu\text{m} \pm 5\mu\text{m}$, $1.180 \text{ mm} \pm 0.050\text{mm}$ and $5.100 \text{ mm} \pm 0.050\text{mm}$. We also fabricated microlens of 20 μm but in this case the focal length was not analyzed since the focus distribution were not uniform.
- It has been showed how the optical quality improves by increasing the reflowing temperature. This improvement is manifested in the reduction of the focal spot sizes, their homogeneity and the better irradiance distribution.
- The optical aberrations of the microlens arrays fabricated at 650°C, 660°C and 670°C have been also determined. The topographic data obtained with confocal microscope have been used for analyzing the optical aberrations of the microlens array by calculating the modal coefficients of the expansion of the height data in terms of the orthogonal Zernike polynomial basis. The best result has been obtained for the microlens generated at 670°C, which present a wavefront root mean square error of $\lambda/28$ and a variability of $\lambda/77$

- Concerning microchannel fabrication the proposed techniques allowed us to obtain microchannels of a minimum diameter of $8\mu\text{m}$ and depth of $1.5\mu\text{m}$. A decrease of the roughness average generated after laser ablation, of two orders of magnitude reaching values of the order of the unprocessed glass, has been obtained thanks to the thermal treatment.
- The laser-matter interaction process using different pulse widths, covering the nanosecond, picosecond and femtosecond regimes has been investigated. The data obtained have provided useful information for a better understanding of the laser-matter interaction process, which was analyzed as a sequence of simpler interconnected problems: the absorption of laser light, the ionization and energy transfer from electrons to ions, the heat conduction and hydrodynamic expansion resulting in the ablation process.
- It has been shown that the ablative process in glasses can be promoted by: 1) impurities presented in soda-lime glass; 2) surface roughness; 3) pulse width; and 4) defects at surfaces (that acts like scattering center for the incoming light promoting its interaction with the surface of transparent materials).
- It has been identified, using EDX analysis, different percentages of Sn impurities on each side of the soda-lime glass. In order to evaluate the influence of these impurities as seed electrons for initiating the ablation process, the ablation threshold was identified independently over each side. The laser used was an IR nanosecond laser operating at 1064nm . The ablation thresholds identified correspond to 112 J/cm^2 for the side A

(with Sn impurities) and 920 J/cm^2 in side B (with non Sn impurities), which means a reduction nearly of one order of magnitude.

- Considering laser-matter interaction, an attempt was made to identify the mechanism that leads to the ablation of the transparent materials using a thin film coating at different pulse durations, so three factors affecting the ablation region were identified on literature and considered in this work. The first one is related with structural defects in the aluminum thin film (roughness) which enhances absorption in dielectric. The second one is related with impurity incorporation which increases the absorption of laser energy, during later part of the pulse or for subsequent pulse. The last one is related to the charge transfer from the thin film into dielectric which leads to avalanche absorption mechanism.
- It has been investigated the influence of the pulse width in the nanosecond, picosecond and femtosecond regimes in combination with the deposition of an absorbent aluminum layer of 15nm thickness, by determining the ablation threshold over different glass materials (soda-lime, borosilicate, fused silica and sapphire) Comparison with non covered surfaces has been made. In the nanosecond regime an ablation threshold reduction of two orders of magnitude has been obtained for borosilicate, fused silica and sapphire and one order of magnitude for soda-lime glass. In case of picosecond pulses it is slightly reduced in some glasses, less in borosilicate in which the overall value for ablation threshold is a little bit higher. For femtosecond pulses there is no significant reduction in the ablation threshold and the enhancement is minor. The best enhancement in terms of energy reduction was obtained for nanosecond laser and the glass covered with the aluminum layer, presenting low ablation threshold,

which is very important since most of the glasses do not absorb IR wavelengths

- It has been demonstrated the structuring capabilities of microlens arrays over a variety of different material, such as stainless steel, aluminum, copper and polymer. Surface multidrilling, debris removing and surface texturing were faced.
- Improvement in microlens durability has been obtained by separating the microlens from the target thanks to the exploitation of the Talbot effect. Demonstration of this procedure for multidrilling chrome targets with a IR laser ($\lambda = 1064 \text{ nm}$) and a microlens array of $60 \mu\text{m}$ diameter and $1,180 \text{ mm}$ focal length, placing the substrate at $14,700 \text{ mm}$ (in the second Talbot plane) has been presented. Significant reduction in the debris content after laser ablation has been also reported.

REFERENCES

- [Akashi2006] "Deep reactive ion etching of borosilicate glass using bonded silicon wafer as an etching mask", Akashi T and Yoshimura Y, *J. Micromech. Microeng.* **16**, 1051 (2006)
- [Albero2009] "Fabrication of spherical microlenses by a combination of isotropic wet etching of silicon and molding techniques" Jorge Albero, Lukasz Nieradko, Christophe Gorecki, Heidi Ottevaere, Virginia Gomez, Hugo Thienpont, Juha Pietarinen, Birgit Päivänranta, and Nicolas Passilly, *Optics Express*, **17** (8) 6283-6292 (2009)
- [Arkipov2000] "Is there avalanche multiplication in amorphous semiconductors? V.I. Arkipov, S.O. Kasap, *Journal of Non-Crystalline Solids* 266-269 (2000)
- [Alexander1979] "Laser induced damage in optical materials: tenth ASTM symposium" Alexander J. Glass and Arthur H. Guenther, *Applied Optics*, **18**, (13), 2112-2129 (1979)
- [Berry1996] M.V. Berry and S. Klein, "Integer, fractional and fractal Talbot effects" *J. Mod. Opt.* **43** 2139 (1996)
- [Besold1997] B. Besold, N. Lindlein, "Fractional Talbot effect for periodic microlens arrays", *Opt. Eng.* **36**, 1099-1105 (1997).
- [Ben-Yakar2004] "Femtosecond laser ablation properties of borosilicate glass" Adela Ben-Yakar, Robert L. Byer, *Journal of Applied Physics*, **96**, (9), 5317-5323 (2004)
- [Bousse2001] "Protein sizing on a microchip" L. Bousse, S. Mouradian, A. Minalla, H. Yee, K. Williams, R. Dubrow, *Anal. Chem.* **73**, 1207(2001)
- [Ben-Yakar2004] "Femtosecond laser ablation properties of borosilicate glass" Adela Ben -Yakar, Robert L. Byer, *Journal of Applied Physics*, **96**, 5316-5323 (2004)
- [Bityurin2003] "Use of harmonics for femtosecond micromachining in pure dielectrics" , N. Bityurin and A. Kuznetsov, *J. Appl. Phys.* **93**, 1567 (2003)
- [Cvavel1984] P. Chavel and T.C. Strand. "Range measurement using Talbot diffraction imaging of gratings"*Appl. Opt.*, **23**, 862, (1984).
- [Cheng2004] "Microfluidic laser embedded in glass by three-dimensional femtosecond laser microprocessing" Ya Cheng, Koji Sugioka, and Katsumi Midorikawa, *OPTICS LETTERS* **29**, (17), 2007 – 2009 (2004)
- [Cheng2004] "Direct-write laser micromachining and universal surface modification of PMMA for device development" Ji-Yen Cheng, Cheng-Wey Wei, Kai-Hsiung Hsu, Tai-Horng Young, *Sensors and Actuators B: Chemical*, **99**, (1), 186–196(2004)

- [Coughlan2008] “Antibacterial coatings for medical devices based on glass polyalkenoate cement chemistry” Coughlan A., Boyd D., Douglas CW., Towler MR., *J Mater Sci Mater Med.* **19** (12) 3555-60 (2008)
- [Chiu2000] Patterned deposition of cells and proteins onto surfaces by using three-dimensional microfluidics system” D.T. Chiu, N.L. Jeon, S. Huang, R.S. Kane, C.J. Wargo, I.S. Choi, D.E. Ingber, G.M. Whitesides, *Proc. Natl. Acad. Sci. U.S.A.* **97**, 2408 (2000).
- [Chen2001] “*Nanofabrication: conventional and non-conventional methods* “ Y. Chen, A. Pepin, *Electrophoresis* **22** 187 (2001).
- [Ching-Hua2001] “Modeling optical breakdown in dielectrics during ultrafast laser processing” Ching-Hua Fan and Jon P. Longtin, *APPLIED OPTICS*, **40**, (18), 3124-3131, (2001)
- [Duarte2008] “Increasing Lubricant Film Lifetime by Grooving Periodical Patterns Using Laser Interference Metallurgy”, M. Duarte, A. Lasagni, R. Giovanelli, J. Narciso, E. Louis, F. Mücklich, *Advanced Engineering Materials* **10** (6), 554-558, (2008)
- [Dumitru2000] “Laser microstructuring of steel surfaces for tribological applications” Dumitru, G., Romano, V., Weber, H.P., Haefke, H., Gerbig, Y., Pflüger, E. *Appl. Phys. A* **70**, 485–487 (2000)
- [Etsion2005] “State of the art in laser surface texturing Etsion”, I., 2005.. *J. Tribol.* **127**, 248–253.
- [Eskin2005] “Experimental study of structure formation in binary Al–Cu alloys at different cooling rates” Eskin, D., Du, Q., Ruvalcaba, D., Katgerman, L *Mater. Sci. Eng. A* **405**, 1–10 (2005)
- [Erickson2004] “Integrated microfluidic devices” David Erickson, Dongqing Li, *Analytica Chimica Acta* **507**, 11–26 (2004)
- [Flores-Arias2009] “Phase diffractive optical gratings on glass substrates by laser ablation” M.T. Flores-Arias a, A. Castelo, C. Gomez-Reino, G.F. de la Fuente, *Optics Communications* **282**, 1175–1178 (2009)
- [Grosse2001] “Deep wet-etching of fused silica glass for hollow capillary optical leaky waveguides in microfluidic devices” Grosse A, Grewe M and Fouckhardt H
J. Micromech Microeng. **11** 257–62 (2001)
- [Gomez2008] “ Characterization of Refractive Index Distribution in Spherical Microlenses Fabricated by Deep Proton Writing” Gomez, V. ; Pakula, A. Ottevaere, H. ; Kujawinska, M. ; Thienpont, H. *Photonics Technology Letters*, [2008]

- [Gamaly2006] "Laser-matter interaction in the bulk of a transparent solid: Confined microexplosion and void formation" Eugene G. Gamaly, Saulius Juodkazis, Koichi Nishimura, and Hiroaki Misawa, Barry Luther-Davies, *PHYSICAL REVIEW*, **73**, 214101 (2006)
- [Gamaly2001] "Ablation of solids by femtosecond lasers: ablation mechanism and ablation thresholds for metals and dielectrics" E. G. Gamaly, A. V. Rode, V. T. Tikhonchuk, and B. Luther-Davies, *Phys. Rev. A* (2001)
- [Hao2003] "CO₂ laser modification of the wettability characteristics of a magnesia partially stabilized zirconia bioceramic" Hao, L., Lawrence, J. J. *Phys. D: Appl. Phys.* **36**, 1292–1299 (2003)
- [Hao2004] "CO₂ laser induced microstructure features in magnesia partially stabilised zirconia bioceramic and effects thereof on the wettability characteristics", Hao, L., Lawrence, J. *Mat. Sci. Eng. A* **364**, 171–181 (2004)
- [Hao2004b] "The adsorption of human serum albumin (HSA) on CO₂ laser modified magnesia partially stabilised zirconia" (MgO-PSZ). Hao, L., Lawrence, J., *Colloids Surf. B* **34**, 87–94, (2004),
- [Hao2004c] "Examination of CO₂ laser-induced rapid solidification structures on magnesia partially stabilised zirconia and the effects thereof on wettability characteristics. "Hao, L., Lawrence, J., Lim, G.C., Zheng, H.Y. *Opt. Laser. Eng.* **42**, 355–374. (2004)
- [Harimar2004] "Crystallographic and morphological textures in laser surface modified alumina ceramic" "Harimkar, S.P., Dahotre, N.B, *J. Appl. Phys.* **100**, 024901. (2004)
- [Hopp2009] "Laser-induced backside dry and wet etching of transparent materials using solid and molten tin as absorbers" B. Hopp, T. Smausz, C. Vass, G. Szabó, R. Böhme, D. Hirsch and K. Zimmer, *Applied Physics A: Materials Science & Processing* **94**, (4), 899-904 (2009) DOI: 10.1007/s00339-009-5078-5
- [Hanada2004] "Development of practical system for laser-induced plasma-assisted ablation (LIPAA) for micromachining of glass materials" Y. Hanada, K. Sugioka, Y. Gomi, H. Yamaoka, O. Otsuki, I. Miyamoto and K. Midorikawa, *Applied Physics A: Materials Science & Processing* **79**, (4-6), 1001-1003 (2004) DOI: 10.1007/s00339-004-2614-1
- [Hong] "Laser-induced-plasma-assisted ablation for glass microfabrication" Minghui Hong; Koji Sugioka; Ding J. Wu; L. L. Wong; Yongfeng Lu; Katsumi Midorikawa; Tow Chong Chong, *Photonic Systems and Applications Proceedings of SPIE* 4595

- [Hopp2004] "Laser induced backside dry etching of transparent materials" , Hopp B., Vass Cs., Smausz T., Photon-Assisted Synthesis and Processing of Functional Materials. E-MRS Symposium H, Nice, FRANCE , **253**, (19) , 7922-7925 (2007)
- [Huang2007] " Quality glass processing by laser induced backside wet etching" Z. Q. Huang, M. H. Hong, K. S. Tiaw, and Q. Y. Lin, Journal of Laser Micro/Nanoengineering **2**, (3) (2007)
- [Haixin2009] "Characterization of deep wet etching of fused silica glass for single cell and optical sensor deposition" Haixin Zhu¹, Mark Holl, Tathagata Ray, Shivani Bhushan and Deirdre R Meldrum, J. Micromech. Microeng. **19** (2009) 065013
- [Hirai2003] "Fine pattern fabrication on glass surface by imprint lithography" Y. Hirai, K. Kanakugi, T. Yamaguchi, K. Yao , S. Kitagawa, Y. Tanaka Microelectronic Engineering, **67–68**, 237–244 (2003)
- [Huang2010] "Energy transmissivity of high-power nanosecond laser pulse focused on glass" Yongzhon Huang, Jinghua Han, Guoying Feng, Liming Yang, Qihui Zhang, Yaguo Li, Qihua Zhu, Opt. Int. J. Light Electron. Opt. (2010)
- [Ihlemann2008] "Micro patterning of fused silica by laser ablation mediated by solid coating absorption" Jürgen Ihlemann, Applied Physics A: Materials Science & Processing **93**, (1), 65-68 (2008) DOI: 10.1007/s00339-008-4663-3
- [Issa2008] "3D transient thermal modelling of laser microchannel fabrication in lime-soda glass" A. Issa, D. Brabazon, M.S.J. Hashmi, journal of materials processing technology, 307–314 (2008)
- [Kopitkovas2007] "Laser Induced Backside Wet Etching: Mechanisms and Fabrication of Micro-Optical Elements", G. Kopitkovas, T. Lippert, J. Venturini, C. David and A. Wokaun , Journal of Physics: Conference Series **59**, 526–532 (2007) DOI:10.1088/1742-6596/59/1/113
- [Kopitcovas2003] "Fabrication of micro-optical elements in quartz by laser induced backside wet etching" G. Kopitkovasa, T. Lipperta ,*, C. Davidb, A. Wokauna, J. Gobrechtb Microelectronic Engineering **67–68**, 438–444 (2003)
- [Kumar2002] "A study on the grinding of glass using electrolythic in-process dressing", Senthil Kumar A, Lim H.S, Rahman M, Fathima K, journal of eletronic materials, **31**, (10), 1039-1046 (2002)

- [Karthe1995] "Micro- and integrated optical devices in glasses and polymers for hybride integration into microsystems" W. Karthe, R. Göring, A. Bräuer, E. B. Kley, Ch. Wächter, P. Dannberg and T. Poßner *Microsystem Technologies* **1**, (2) 59-67, (1995)
- [Khandurina2000] "Integrated System for Rapid PCR-Based DNA Analysis in Microfluidic Devices," J. Khandurina, T.E. McKnight, S.C. Jacobson, L.C. Waters, R.S. Foote, J.M. Ramsey, *Anal. Chem.* **72** (2000) 2995.
- [Kasaai2003] "The interaction of femtosecond and nanosecond laser pulses with the surface of glass" Mohammad R. Kasaai *, Vijayalakshmi Kacham, Francis Theberge, See Leang Chin, *Journal of Non-Crystalline Solids* **319** 129–135 (2003)
- [Keldish1965] "Ionization in the field of a strong electromagnetic wave" L. V. Keldysh, *Sov. Phys. JETP* **20**, 1307 (1965)
- [Keldish1965] "Kinetic theory of impact ionization in semiconductors" LV Keldysh - *Sov. Phys. JETP* (1960)
- [Krol2008] "Femtosecond laser modification of glass", D.M. Krol, *Journal of Non-Crystalline Solids* **354**, 416–424, (2008)
- [Lee2004] "Nonresonant Laser-Matter Interaction", Lee; Chong, Tow Chong, (NLMI-11). Edited by Libenson, Mikhail N. *Proceedings of the SPIE*, **5506**, 1-10 (2004)
- [Leger1984] J.R. Leger and M.A. Snyder." Real-time depth measurement and display using resnel diffraction and white-light processing" *Appl. Opt.*, **23** 1655, (1984).
- [Liu1997] "Laser Ablation and Micromachining with Ultrashort Laser Pulses" X. Liu, D. Du, and G. Mourou , *Journal of Quantun electronics*, **33**, (10), 1706-171 (1997)
- [Li2001] "Deep reactive ion etching of Pyrex glass using SF6 plasma" Li X, *Sensors and actuators A:Physical* (2001)
- [Luo2006]"Studies on cut-off grinding of BK7 optical glass using thin diamond wheels" Luo S.Y, Tsai Y.Y, and Chen C.H, *journal of materials processing technology*, **173**, (3), 321-329 (2006)
- [Liu2001] " Microfabricated polycarbonate CE devices for DNA analysis" Y. Liu, D. Ganser, A. Schneider, R. Liu, P. Grodzinski, N. Krutchinina, *Anal. Chem.* **73** 4196(2001)
- [Li2001] "A quality study on the excimer laser micromachining of electro-thermal-compliant micro devices", Jun Li and G K Ananthasuresh 2001 *J. Micromech. Microeng.* **11**, 38, (2001)

- [Liu1997] "Laser Ablation and Micromachining with Ultrashort Laser Pulses" X.Liu, D. Du, and G. Mourou, *Journal of Quantum Electronics*, **33**, (10), October 1997, 1706-1716
- [Ming-Hsien2003] "Generation of submicrometer structures by photolithography using arrays of spherical microlenses" Ming-Hsien Wu, Cheolmin Park, and George M. Whitesides, *Journal of Colloid and Interface Science* **265**, 304–309 (2003)
- [Malalahalli 2004] "Femtosecond pulsed laser micromachining of glass substrates with application to microfluidic devices" Malalahalli S. Giridhar, Kibyoung Seong, Axel Schu" Izgen, Pramod Khulbe, Nasser Peyghambarian, and Masud Mansuripur, *4584 APPLIED OPTICS* **43**, (23), 4584-4589 (2004)
- [Malek2007] "Deep microstructuring in glass for microfluidic applications" Chantal Khan Malek, Laurent Robert Jean-Jacques Boy, Pascal Blind, *Microsyst Technol* **13**: 447–453 (2007)
- [Mannion2004] "The effect of damage accumulation behaviour on ablation thresholds and damage morphology in ultrafast laser micro-machining of common metals in air", P.T Mannion, J Magee, E Coyne, G.M O'Connor, T.J Glynn, *Applied Surface Science*, **233**, (1–4), 30, 275–287 (2004)
- [McCredy2000] Fabrication techniques and materials commonly used for the production of microreactors and micro total analytical systems, T. McCredy, *Trac-Trends Anal. Chem.*, 2000, 19, 396-401. (2000)
- [Martin2003] "Spot-size dependence of the ablation threshold in dielectrics for femtosecond laser pulses" S. Martin, A. Hertwig., Lenzner, J. Kruger, W. Kautek, *Applied Physics*, **77**, 883–884 (2003)
- [Manenkov1986] "Laser-induced damage in solids", A. A. Manenkov and A. M. Prokhorov, *Sov. Phys. Usp.* **29**, 4 (1986)
- [Ozakas2006] H.M. Ozaktas, D. Mendlovic, "Fourier transforms of fractional order and their optical interpretation" *Opt. Comm.***101**, 163-169 (1993)
- [Patorski1989] K. Patorski, "The self-imaging phenomenon and its applications", in *Progress in Optics XXVII*, E. Wolf, ed., Elsevier Science, Amsterdam, The Netherlands, (1989)
- [Piqué2006] "Embedding electronic circuits by laser direct-write" A. Piqué, S.A. Mathews, B. Pratap, R.C.Y. Auyeung, B.J. Karns, S. Lakeou, *Microelectronic Engineering*, **83**, (11–12), 2527–2533 (2006)

- [Philips1977] "On the mechanism of material removal by free abrasive grinding of glass and fused silica" Philips K, Crimes G.M, Wilshaw T.R, *Wear*, **41**, 327-350 (1977)
- [Pronko1995] "Thermophysical effects in laser processing of materials with picoseconds and femtosecond pulses" P. P. Pronko, S. K. Dutta, D. Du, and R. K. Singh, *J. Appl. Phys.* **78**, 6233–6240 (1995)
- [Pronko2008] "Avalanche ionization and dielectric breakdown in silicon with ultrafast laser pulses" P. P. Pronko, P. A. VanRompay, C. Horvath, F. Loesel, T. Juhasz, X. Liu, and G. Mourou, *Physical review B*, **58**, 5 (1998)
- [Rabia2007] "IR Laser Plasma Interaction With Glass" Rabia Qindeel, Noriah Bidin and Yaacob Mat Daud, *American Journal of Applied Sciences* **4** (12): 1009-1015, (2007)
- [Razzaque2008] "Performance of Mechanical Face Seals with Surface Micropores", M. Mahbubur Razzaque, M. Tanvir Rahman Faisal, *Journal of Mechanical Engineering* **37** (2008)
- [Rethfeld2004] "Unified model for the free-electron avalanche in laser-irradiated dielectrics" B. Rethfeld, *Phys. Rev. Lett.* **92**, 187401 (2004)
- [Righini1991] "Characterization of reactive ion etching of glass and its applications in integrated optics" Shen Ronggui and Giancarlo C. Righini, *J. Vac. Sci. Technol. A* **9**, 2709 (1991)
- [Rudolph1999] "Femtosecond- and nanosecond-pulse laser ablation of bariumaluminumborosilicate glass" P. Rudolph, J. Bonse, J. Krüger, W. Kautek, *Appl. Phys.*, **69**, S763–S766 (1999)
- [Sandip2009] "Rapid surface microstructuring of porous alumina ceramic using continuous wave Nd:YAG laser" Sandip P. Harimkar, Narendra B. Dahotre *Journal of Materials Processing Technology* **209**, 4744–4749 (2009)
- [Scafffer2001] "Micromachining bulk glass by use of femtosecond laser pulses with nanojoule energy", Chris B. Schaffer, André Brodeur, José F. García, and Eric Mazur, *Optics Letters*, **26**, 2 (2001)
- [Siiman2009] "Nonlinear photoionization and laser-induced damage in silicate glasses by infrared ultrashort laser pulses" L.A. Siiman J. Lumeau L.B. Glebov, *Appl Phys B*, **96**, 127–134 (2009)
- [Smausz2007] "Influence on the laser induced backside dry etching of thickness and material of the absorber, laser spot size and multipulse irradiation", T. Smausz, T. Csizmadia, N. Kresz, Cs. Vass, Zs. Márton, B. Hopp, *Applied Surface Science*, **254**, (4), 1091-1095 (2007)

- [Stuart1995] "Laser-Induced damage in Dielectrics with Nanosecond to Subpicosecond Pulses" B.C.Stuart, M.D. Feeit, A.M. Rubenchik, B.W.Shore, and M.D. Perry, Physical review letters, **74**, (12), 20, (1995)
- [Stuart 1996] "Nanosecond-to-femtosecond laser-induced breakdown in dielectrics" B. C. Stuart, M. D. Feit, S. Herman, A. M. Rubenchik, B. W. Shore, and M. D. Perry, Phys. Rev. **53**, (1996)
- [Solak2006] H.H. Solak. "Nanolithography with coherent extreme ultraviolet light", J. Phys. D: Appl. Phys, **39**, (2006).
- [Sohn2005] "Fabrication of photonic devices directly written within glass using a femtosecond laser" Ik-Bu Sohn, Man-Seop Lee, Jeong-Sik Woo, Sang-Man Lee, Jeong-Yong Chung, OPTICS EXPRESS **13**, (11) / 4224-4229 (2005)
- [Steingoetter2005] "Deep fused silica wet etching using an Au-free and stress-reduced sputterdeposited Cr hard mask" Steingoetter I and Fouckhardt H. J. Micromech. Microeng. **15** 2130–5 (2005)
- [Stone2001] "Microfluidics: Basic issues, applications, and challenges", H.A. Stone, S. Kim, ALChE J. **47** (2001) 1250.
- [Stuerzebecher2010] L. Stuerzebecher, T. Harzendorf, U. Vogler, U. D. Zeitner, and R. Voelke "Advanced mask aligner lithography: Fabrication of periodic patterns using pinhole array mask and Talbot effect", Opt.Express, **18**, 19485-19494, (2010)
- [Su2008] "Refractive index variation in compression molding of precision glass optical components" Lijuan Su, Yang Chen, Allen Y. Yi, Fritz Klocke, and Guido Pongs, Applied Optics, **47**, (10), 1662-1667 (2008)
- [Sudrie2002] "Femtosecond Laser-Induced Damage and Filamentary Propagation in Fused Silica" Sudrie, A. Couairon, M. Franco, B. Lamouroux, B. Prade, S.Tzortzakis, and A. Mysyrowicz, Phys. Rev. Lett. **89**, 186601 (2002)
- [Sugioka2004] "Glass microprocessing by laser-induced plasma-assisted ablation: fundamental to industrial applications" Sugioka, Koji; Midorikawa, Katsumi; Yamaoka, Hiroshi; Gomi, Yutaka; Otsuki, Masayoshi; Hong, Ming Hui; Wu, Dong Jiang; Wong, Lai [Sze2001] "Semiconductors devices: physics and technology" S.M Sze, ISBN 0-471-33372-7
- [Thawari2005] "Influence of process parameters during pulsed Nd:YAG laser cutting of nickel-base superalloys" G. Thawari , J.K. Sarin Sundar , G. Sundararajan, S.V. Joshi, Journal of Materials Processing Technology **170**, 229–239 (2005)
- [Thienot2006] "Reactive ion etching of glass for biochip applications: Composition effects and surface damages" Edouard Thienot, Florian Domingo,

- Edmond Cambuil, Charlie Gosse, *Microelectronic Engineering*, **83**, 1155-1158 (2006)
- [Torrissi2007] "Study on the ablation threshold induced by pulsed lasers at different wavelengths" L. Torrissi, A. Borrielli, D. Margarone, *Nuclear Instruments and Methods in Physics Research B*, 255–379 (2007)
- [Vatsya 2002] "Modeling of laser-induced avalanche in dielectrics" S. R. Vatsya and S. K. Nikumb, *J. Appl. Phys.* **91**, 344 (2002)
- [Whitesides2001] "Flexible methods for microfluidics" G.M. Whitesides, A.D. Stroock, *Phys.* **51**, 42 (2001)
- [Weng2002] "A material removal model for polishing glass-ceramic and aluminum magnesium storage disk" Chih-Cheng Wang, Shih-Chieh Lin and Hong Hochen, *International Journal of Machine Tools and Manufacture*, **42**, (8), 979-984(2002)
- [Wensink2000] "High resolution powder blast micromachining" Wensink, H. Berenschot, J.W.; Jansen, H.V.; Elwenspoek, M.C. *Micro Electro Mechanical Systems, MEMS 2000*. 10.1109/MEMSYS.2000.838615 (2000)
- [Xuchuan2010] "Analysis of avalanche mechanisms in short-pulses laser-induced damage" Xuchuan Shang, Rongzhu Zhang, Ping Mab Optics & Laser Technology **42**, 243–246 (2010)
- [Yamamoto2010] "Influence of thermal expansion coefficient in laser scribing of glass" Koji Yamamoto, Noboru Hasaka, Hideki Morita, Etsuji Ohmura, *Precision Engineering* **34**, 70–75 (2010)
- [YI2006] "A high volume precision compression molding process of glass diffractive optics by use of a micromachined fused silica wafer mold and low T_g optical glass" A Y Yi, Y Chen, F Klocke, G Pongs, A Demmer, D Grewell and A Benatar, *J. Micromech. Microeng.* **16** 2000 (2006)
- [Zheng2008] Experimental Investigation on Ultrasonic Face Machining of Glass with Free Abrasives Shu You Zheng et al., 2008, *Key Engineering Materials*, 375-376, 268
- [Zimmer2008] "Laser-Induced Backside Wet Etching of Transparent Materials with Organic and Metallic Absorbers" K. Zimmer and R. Böhme *Laser Chemistry* Vol. **2008** (2008), Article ID 170632, DOI :10.1155/2008/170632
- [Zoubir2003] "Practical uses of femtosecond laser micro-materials processing" A. zoubir, L. shah, K. Richardson, M. richardson, *Appl. Phys. A* **77**, 311–315 (2003)

Internet references:

[Beam profiler]

http://www.thorlabs.de/newgrouppage9.cfm?objectgroup_id=804

[MM-400]

http://www.nikon.com/products/instruments/lineup/industrial/measuring_instruments/measuring_microscope/mm-400_800/index.htm

[Spectrophotometer]

<http://www.perkinelmer.com/Catalog/Category/ID/UVis%20UVisNIR%20Systems>

[FESEM]

<http://www.zeiss.com/microscopy>

[SENSOFAR]

<http://www.sensofar.com/>

Resumen

(Castellano)

Resumen

En la presente tesis se propone la fabricación de elementos en vidrio para micro-óptica y microfluídica que exigen microestructuras de alta calidad. Estos elementos son altamente demandados desde sectores industriales, por lo que se precisan técnicas de procesado, rápidas, sencillas y de bajo coste.

Tradicionalmente, los materiales más comúnmente utilizados para la fabricación de elementos microópticos son los polímeros, por ser materiales de bajo coste. Por el contrario, estos materiales tienen algunas limitaciones debido al reducido abanico de índices de refracción que presentan, la estabilidad limitada a altas temperaturas, el quemado en su procesado con láseres de alta potencia, su menor transparencia al UV y consecuente degradación. Estos límites se pueden superar mediante el uso de vidrios. Los materiales vítreos debido a sus características termo-mecánicas son adecuados para muchas aplicaciones en micro y nanotecnología. Las principales ventajas del vidrio frente a los materiales poliméricos se derivan de sus propiedades y características específicas, ofreciendo una alta compatibilidad con el sílice para su empaquetamiento, el buen comportamiento químico y la alta resistencia a la radiación, así como una buena estabilidad térmica y mecánica.

La micro-óptica juega un papel importante en diversos procesos de producción industrial, como la micro-electrónica, micro-mecanizado por láser, procesamiento de materiales, inspección óptica, visión artificial y la metrología de precisión. Los elementos se encuentran en la industria médica, sistemas de análisis de bio-fotónica y sensores ópticos. Muchas de las aplicaciones de estos elementos microópticos requieren una muy buena calidad de los mismos (precisión, calidad,

duración...) por eso es importante alcanzar estas características al menor coste de producción posible para poder ofrecer elementos competitivos.

En el entorno de la microfluidica, el uso de dispositivos de microfluídica se va abriendo paso rápidamente en las nuevas técnicas analíticas de laboratorio, principalmente debido a su pequeña huella física, velocidad y eficiencia de las separaciones químicas, y la reducción de consumo de reactivos. Tradicionalmente, los sistemas y dispositivos de análisis han sido fabricados en silicio, debido a sus propiedades y a las técnicas de micromecanizado que son comunes en la industria microelectrónica. Recientemente se ha comenzado a utilizar dispositivos fabricados a partir de sustratos de polímeros como una alternativa al vidrio, aunque en la medicina clínica biología y química, el vidrio todavía es el material preferido. Los microcanales fabricados en vidrio tienen una importancia creciente en la miniaturización de los dispositivos de microfluidos para la industria química y biológica.

Los diferentes métodos de micromecanizado proporcionan la capacidad de obtener microestructuras con alta precisión y repetitividad. Las técnicas más comunes utilizadas para microestructurado de vidrio son la ablación por láser, el grabado, moldeado y micromecanizado mecánico. El micromecanizado por láser ofrece un método de un solo paso para la escritura directa de los microcanales en el vidrio. Utilizando esta técnica de ablación por láser, es posible fabricar geometrías con profundidad variable y alta relación de aspecto que no puede lograrse mediante las técnicas tradicionales de microlitografía. La rigidez mecánica, resistencia química y las propiedades de baja permeabilidad del vidrio, junto con su transparencia óptica, hacen una buena opción. En ese contexto, el objetivo de esta tesis es desarrollar un método para la fabricación de microlentes y microcanales sobre sustratos de vidrio, con aplicaciones en micro-optica y

microfluidica. El método propuesto está compuesto por una técnica de escritura láser directa que nos permite fabricar estructuras en vidrio, un mordentado químico que nos permite eliminar las imperfecciones generadas durante la ablación con láser y un tratamiento térmico para modificar la topografía y mejorar las cualidades ópticas y morfológicas de la microlentes y microcanales fabricados. La técnica de escritura laser directa utilizada para el el microestructurado de vidrio se basa en el uso de un láser pulsado combinado con un sistema galvanométrico que nos permite fabricar elementos con diferentes configuraciones, como por ejemplo elementos cilíndricos, que darán lugar a microlentes después del tratamiento térmico, o a microcanales con diferentes geometrías.

Como paso intermedio entre el procesado laser y la modificación de la estructura mediante el tratamiento térmico, se ha aplicado con éxito un mordentado químico con ácido fluorhídrico, con la finalidad de suavizar la superficie mediante la eliminación de la rugosidad, y para eliminar cualquier estructura secundaria generadas durante la ablación láser de vidrio de soda-cálcico y que será perjudicial para el posterior refundido térmico. Durante el ataque químico se ha investigado el comportamiento del mordentado en función del tiempo de interacción entre el vidrio y el acido, manteniendo constantes la concentración y la temperatura. Los valores de concentración se han mantenido en un 10% durante todo el proceso operando siempre a temperatura ambiente, lo cual reduce al mínimo los riesgos de toxicidad que presenta el acido fluorhídrico.

Como última etapa, se aplica un tratamiento térmico para modificar la forma y la rugosidad de los elementos. Gracias al reflujo térmico de vidrio es posible obtener microlentes y microcanales con una rugosidad de 3 y 7,35 nanómetros respectivamente. Los valores de rugosidad obtenidos están dos órdenes de

magnitud por debajo de la rugosidad después del microestructurado láser. Con el fin de optimizar el proceso se investigó la influencia de la temperatura, para un tiempo de calentamiento determinado, sobre el desplazamiento de material fundido en función de la forma y empaquetamiento de los elementos generados con el láser. Las temperaturas analizadas se encuentran comprendidas entre 620°C y 680°C, ambas situadas por encima de la temperatura de fusión del vidrio situada a 564°C. En nuestros experimentos observamos que a temperaturas menores de 620°C no se modifica el material y a temperaturas mayores de 680°C el material se funde en exceso dando lugar a geometrías planas que no funcionan como microlentes ni mantienen la forma de microcanal.

Paralelamente al proceso de fabricación, se investiga la interacción entre el haz láser y varios materiales vítreos (zafiro, borosilicato, soda-cálcico y sílica fundida). Analizados los resultados y en base a las propiedades de cada vidrio podemos dar una visión general del proceso de ablación de los distintos vidrios. Atendiendo a esto y en función de los umbrales de ablación obtenidos para cada vidrio, hemos identificado una reducción en un orden de magnitud en un lado del vidrio de soda-calcio. Esta reducción está relacionada con impurezas de Sn que son incorporadas al vidrio durante el proceso de fabricación, en el cual el vidrio aun fundido se deposita en un baño de estaño, el cual le confiere planitud durante el proceso de enfriamiento. La reducción del umbral de ablación de estos vidrios hace de ellos el substrato elegido para fabricar, con menor gasto de energía, los elementos microópticos que en esta tesis se presentan.

En cuanto a factores que aportan información para comprender los mecanismos de desencadenan el proceso ablativo se ha investigado la influencia de las impurezas, el papel de la rugosidad y defectos en las superficies así como el efecto de la anchura de pulso. Se ha mostrado que tanto la presencia de impurezas,

rugosidad o defectos superficiales favorecen el proceso ablativo, contribuyendo significativamente a la reducción del umbral de ablación. Esta reducción es fundamental para el uso de láseres de nanosegundos para la ablación de materiales dieléctricos y en particular el vidrio.

En cuanto a los factores que aportan datos para la optimización del proceso de fabricación se ha analizado, el tamaño del haz, la superposición de pulsos, el umbral de ablación y la deposición de los desechos generados durante la fabricación de los elementos.

Adicionalmente, y como respuesta a los resultados obtenidos con los vidrios sodocálcicos y las impurezas presentes en él, se presenta un mecanismo de mejora del proceso ablativo mediante la deposición de una capa de aluminio de espesor 15nm, que actúa como mecanismo de confinamiento de la luz, reduciendo dos órdenes de magnitud el umbral de ablación.

Por último, se presentan las capacidades de multiestructurado de las matrices de microlentes para superficies de materiales tales como la fabricación simultánea de agujeros o perforaciones, la eliminación de suciedad superficial y el microestructurado selectivo. Sin embargo, en todas las tareas se observó un deterioro significativo de las matrices de microlentes debido a la deposición de los residuos arrancados en el proceso de ablación sobre la superficie de las mismas. Con el fin de reducir esta degradación hemos propuesto y demostrado la aplicación del efecto Talbot. Este efecto, ampliamente conocido en la literatura, consiste en la formación de imágenes no convencionales, cuando se ilumina un objeto periódico con una fuente de luz coherente. Las imágenes Talbot tienen lugar a distancias discretas cuyo valor depende del periodo del objeto iluminado y de la longitud de onda de la fuente de iluminación. El efecto Talbot se emplea en esta

tesis como instrumento para aumentar la distancia de trabajo entre la matriz de microlentes y el sustrato. De este modo, se produce una reducción en el depósito de escombros sobre la matriz, aumentando la vida útil del elemento óptico

El esquema de la tesis es el que sigue:

En el capítulo 1 se presentan los materiales de vidrio y sus aplicaciones en micro-óptica y microfluidos. Además, se describen algunos métodos comunes usados para microestructurado de materiales de vidrio tales como el mordentado químico, grabado por iones reactivos (RIE) y técnicas de mecanizado por pulido y abrasión, centrándose en la tecnología láser

El capítulo 2 analiza los mecanismos que conducen a la ablación con láser en un vidrio transparente a la longitud de onda del láser y pone de relieve los diferentes procesos que tienen lugar cuando se utilizan láseres con distintas duraciones de pulsos (nanosegundos, picosegundos y femtosegundos).

El capítulo 3 describe las propiedades ópticas, mecánicas, térmicas y de composición del vidrio sódico-cálcico. También describe las herramientas de caracterización utilizadas en el desarrollo de esta tesis, para determinar la composición, morfología, y propiedades ópticas. Se presentan los láseres utilizados para el microestructurado de vidrio en este trabajo y las características del horno en el que se aplicó el tratamiento térmico necesario para la optimización de los elementos desarrollados.

El Capítulo 4 presenta una visión general del proceso de ablación de los vidrios sódico-cálcicos, la influencia de las impurezas, el papel de la rugosidad y los

defectos de la superficie y de la duración del pulso del láser. Se estudia cómo determinar el diámetro del haz, el umbral de la ablación y la deposición de los residuos generados en el proceso ablativo. Se investiga la influencia que tiene en el umbral de ablación, la deposición de una película delgada de aluminio sobre el sustrato de vidrio en el que se van a realizar los elementos microópticos.

El capítulo 5 presenta una técnica de escritura láser directa para la fabricación de microlentes plano-convexas y microcanales basados en la ablación láser de un vidrio sódico-cálcico. Las microlentes se obtienen mediante la fabricación de postes cilíndricos obtenidos por ablación de vidrio con un láser Q-switch Nd:YVO₄, con pulsos de nanosegundos, trabajando en su longitud de onda fundamental (1064nm). Para el desplazamiento del haz láser a lo largo de la estructura diseñada se utiliza un sistema galvanométrico controlado por software comercial de la casa ROFIN. En el caso de los microcanales, cada estructura se obtiene por la ablación de líneas individuales en diferentes configuraciones. Con el fin de reducir la rugosidad superficial de estos elementos, producida por la ablación láser, se ha utilizado un mordentado químico con ácido fluorídrico al 10% y a temperatura ambiente, con el fin de reducir la toxicidad del proceso. Este mordentado también permite eliminar los restos de material depositados sobre el vidrio después de la ablación láser así como de los postes secundarios que aparecen en la fabricación de microlentes. En este sentido el mordentado químico he demostrado ser una herramienta eficaz para la eliminación de residuos, y para posibilitar la fabricación de microlens en diámetros grandes, en torno a 140 μm y mayores, donde los postes secundarios, debido a su mayor volumen, interfieren con los postes principales que darán lugar a las microlentes, evitando el correcto desplazamiento del material fundido, durante el proceso térmico.

Como última etapa en el proceso de fabricación, se ha aplicado y analizado el comportamiento de los elementos fabricados con el tratamiento térmico. En el caso de las microlentes, la conversión de los postes cilíndricos fabricados mediante ablación por láser se inicia por encima de la temperatura de transición del vidrio ($T_g = 564^\circ\text{C}$), a partir de la cual, al reducirse la viscosidad del vidrio y por tanto la tensión superficial del material fundido, se induce la modificación de las superficies a moldear a través de la redistribución del material de los lados superiores al espacio situado entre los postes cilíndricos. Basándose en esto, se ha analizado el comportamiento del tratamiento térmico para temperaturas por encima de la T_g , (620°C , 630°C , 640°C , 650°C , 660°C , 670°C , 680°C) para un tiempo de calentamiento constante en todos los experimentos de 2 horas. La morfología de las microlentes obtenidas para cada temperatura se analizó con microscopio confocal SENSOFAR PI μ 3200.

Los mecanismos de desplazamiento del material para la fabricación de microcanales son similares al de fabricación de microlentes. Al aplicar el tratamiento térmico a 620°C (durante 2 horas) se obtienen microcanales de alta calidad que mantienen la forma inicial, con una reducción de la rugosidad de un orden de magnitud en comparación con la rugosidad del canal después del procesado laser. A 670°C los valores de rugosidad obtenidos son similares a los del vidrio sin procesar pero la forma cambia considerablemente, perdiendo las propiedades de canal. En este caso se ha propuesto la temperatura de 630°C ya que es la que mejor balance entre rugosidad superficial y deformación del elemento presenta.

Con esta técnica se ha conseguido fabricar arrays de microlentes con diámetros de $40\mu\text{m}$, $60\mu\text{m}$, $140\mu\text{m}$ cada una de ellas con una distancia focal de $510\mu\text{m}$, 1.180 mm y 5.100 mm respectivamente.

En esta sección también presentamos un estudio exhaustivo sobre la calidad de las microlentes fabricadas con la metodología propuesta y en función de la temperatura con la que se aplica el tratamiento térmico. Para ello se escogieron de nuevo las microlentes de 40 micras de diámetro y el rango de temperaturas comprendido entre 650°C , 660°C y 670°C ya que para temperaturas inferiores apenas hay cambios en la forma de los postes de vidrio y superiores la deformación es excesiva llegando a desaparecer. El análisis de las muestras puso de manifiesto la bondad del procedimiento así como una serie de cuestiones relevantes. Por una parte se observó que el diámetro del elemento es prácticamente independiente de la temperatura del tratamiento térmico. Por otra parte sí que se observa una reducción en la sagita que conlleva un cambio en la potencia dióptrica del elemento y por tanto en la distancia focal. También se observa un incremento progresivo en la reducción de la rugosidad superficial, tanto de la microlente como del intersticio lo que disminuye la dispersión de luz mejorando la calidad de los focos. Por otra parte el tratamiento térmico también contribuye a aumentar la similitud entre las microlentes de la matriz y a reducir las aberraciones ópticas. Como ejemplo de la calidad de las microlentes fabricadas decir que en el caso del tratamiento térmico a 670°C se han obtenido aberraciones del orden de $\lambda/28$.

En el capítulo 6 se presentan varias aplicaciones de las matrices de microlentes tales como multiestructurado de superficies de diferente naturaleza (tanto metales como plásticos), la fabricación simultánea de agujeros o perforaciones, la eliminación de restos y el microestructurado selectivo. Asimismo y con el fin de reducir la degradación generada por las partículas despedidas del material durante el proceso ablativo y que alcanzan la superficie de las microlentes durante el proceso de microestructurado, hemos propuesto y demostrado la aplicabilidad del efecto Talbot permitiendo más separación entre las microlentes y

el substrato, lo cual reduce la deposición de partículas, y el alargamiento de la vida útil de las microlentes. En particular se han realizado texturizados superficiales empleando una matriz de microlentes de 60 μ m de diámetro y 1,18mm de focal, colocando el substrato de Cromo a una distancia de 14,7mm, que se corresponde con el segundo plano Talbot ($\lambda=1064$ nm.)

En el capítulo 7 se presentan las conclusiones.

Publications

Publications

"Laser microstructuring of commercial soda-lime glass: Influence of Sn impurities", D. Nieto, J. Arines, C. Gómez-Reino, M. Flores-Arias and G.M. O'Connor. Applied Optics, (2012) (Submitted)

"Laser-based microstructuring of surfaces using low-cost microlens arrays", Daniel Nieto, Gemma Vara, Jose Antonio Diez, Gerard O'Connor, Justo Arines, Carlos Gomez-Reino, Maite Flores-Arias Journal of Micro/Nanolithography, MEMS and MOEMS, (2012) (Accepted)

"Fabrication and characterization of microlens arrays on soda-lime glass using a combination of direct laser write and thermal reflow technique", D. Nieto, J. Arines, C. Gomez-Reino, G. M. O'Connor and M. T. Flores-Arias, Journal of Applied Physics **110**, 023108 (2011)

"A Laser direct-write technique for fabricating microlens arrays on soda lime glass with a Nd:YVO₄ laser", Daniel Nieto, M.T Flores-Arias, G. M. O'Connor and Carlos Gomez-Reino Applied Optics, **49**(26), 4979-4983 (2010)

"Fabricación de microlentes con un láser de Nd:YVO₄", Daniel Nieto, M.T. Flores-Arias and C.Gomez-Reino, Óptica Pura y Aplicada, **42** (4) 241-244 (2009)

"Design of reconfigurable GRIN planar optical interconnects" M.T.Flores-Arias, Carmen Bao, Daniel Nieto, M. Victoria Pérez y C. Gómez-Reino Óptica Pura y Aplicada, **43** (1) 23-26 (2009)

"Laser Backwriting process on glass via ablation of metal targets" A. Castelo, D. Nieto, C. Bao, M.T. Flores-Arias, M. V. Perez, C.Gomez-Reino, C. Lopez Gascona and G.de la fuente. Optics Communications, **273**, 193 - 199 (2007)

"Focusing of Light by zone plates in selfoc gradient GRIN lens", M. Rivas-Moscoso, D. Nieto, C. Gomez-Reino and C. R. Fernandez-Pousa Optics Letters, **28**, 1180-1182 (2004)

Proceedings SPIE.

"Laser-based microstructuring of surfaces materials using low-cost microlens arrays", Daniel Nieto I, Vara, G., Diez, J. A., et al Proceedings of SPIE Vol. 8248, 82480K (2012)

"Laser ablated glass microlens arrays: aberrations dependence on reflowing temperature", Arines, J., Nieto, D., Flores-Arias, M. T., et al., Proceedings of SPIE Vol. 8011, 801105 (2011)

"Microlenses fabrication on glass by combining laser with thermal-reflow technique" Nieto D., Arines, J., Gomez-Reino, C., et al., Proceedings of SPIE Vol. 8011, 80110T (2011)

"Fabrication of microlens arrays on soda-lime glasses with a Nd:YVO₄ laser", Nieto, D., Flores-Arias, M. T., O'Connor, G. M., et al., Proceedings of SPIE Vol. 8001, 80010Q (2011)

"Design of reconfigurable GRIN planar optical interconnects", Gomez-Reino, C., Flores-Arias, M. T., Perez, M. V., Nieto D. et al., Proceedings of SPIE Vol. 6992, 699211 (2008)

"Temperature dependence of laser backwriting process on glass," Castelo, A., Nieto, D., Flores-Arias, M. T., et al., Proceedings of SPIE Vol. 6185, 61851B (2006)

"Laser backwriting process on glass via ablation of metal targets," Castelo, A., Nieto, D., Flores-Arias, M. T., et al., Proceedings of SPIE Vol. 5958, 59582H (2005)

"Lau effect in GRIN media" Garcia-Allegue, M. C., Nieto, D., Flores-Arias, M. T., et al., Proceedings of SPIE Vol. 5956, 595614 (2005)

Contributions to conferences

"Talbot effect for multistructuring of metal surfaces", M. Flores-Arias, J. Arines, C. Gómez-Reino, D. Nieto, G. Vara, P. M. Romero, N. Otero, 13th International Symposium on Laser Precision Micro-fabrication (LPM2012), Washington, EE.UU (2012) (Accepted)

"Microestructurado de superficies mediante efecto Talbot", Daniel Nieto, Justo Arines, Carlos Gómez-Reino, Pablo M. Romero, Nerea Otero and María Teresa Flores-Arias, Reunión Nacional de Óptica, Zaragoza, Spain (2012) (Accepted)

"Fabricación de microlentes por ablación láser: aplicación en microestructurado de superficies", Daniel Nieto, Justo Arines, Carlos Gómez-Reino, Ana I. Gomez-Varela, Gerard M.O'Connor, G. Vara and María Teresa Flores-Arias Reunión Nacional de Óptica, Zaragoza, Spain, (2012) (Accepted)

"Laser-based microstructuring of materials surfaces using low-cost microlens arrays" Nieto, Daniel, Vara, G., Diez, J., Gerard M. O'connor, Justo Arines, C. Gomez-Reino and M. Flores-Arias, Photonic West 2012, San Francisco, EE.UU (2012)

"Laser ablated glass microlens arrays: Aberrations dependence on reflowing temperatures" Daniel Nieto, M. Teresa Flores-Arias Carlos Gómez-Reino and G.M.O'Connor. - ICO-22 General Congress of International Commission of Optics , Puebla, Mexico (15-19 August 2012)

"Microlens fabrication on glass by combining laser with thermal reflow techniques", Daniel Nieto, Justo Arines, M. Teresa Flores-Arias, Carlos Gomez-Reino and G.M.O'Connor - ICO-22 General Congress of International Commission of Optics, Puebla, Mexico, (15-19 August 2011)

"Fabrication of microlens arrays on soda-lime glasses with a Nd:YVO₄ laser" Nieto, Daniel, Flores-Arias, M. Teresa, O'Connor, Gerard; Gomez-Reino, Carlos International conference on Applications of Optics and Photonics, Braga, (3-7 May 2011)

"Microstructuring of glass using laser processing: Micro-Optics and Microfluidics", Daniel Nieto, M.T Flores-Arias, G.M. O'Connor and Carlos Gómez-Reino, 2nd International School on "Laser-surface interactions for new materials production", Venice,Italy(11-18 July 2010)

"Fabrication of Microlens by Nd:YVO₄ laser", D. Nieto, María Teresa Flores Arias and Carlos Gómez-Reino". 6º Spanish Optoelectronics conference -OPTOEL 09 Malaga, Spain (2009)

"Fabricación de recubrimientos de substratos de vidrio plano mediante láser de CO₂", F. Rey-García, D. Nieto, C. Gómez-Reino, M.T. Flores-Arias, G.F. De la Fuente, W. Assenmacher, W. Mader, XLIX - Congreso Anual de la Sociedad Española de Cerámica y Vidrio, Linares (2009)

"Diseño de un Interconector óptico GRIN reconfigurable", M.T. Flores-Arias, Carmen Bao-Varela, D. Nieto, M.V. Pérez, C. Gómez-Reino, IX Reunion Nacional de Optica. Orense, Spain (2009)

"Fabricación de guías de onda mediante tecnología sol-gel sobre sustratos de vidrio plano", F. Rey-García, D. Nieto, M.T. Flores-Arias, C. Gómez-Reino, M.V. Pérez, A. Duran, Y. Castro and G.F. De la Fuente IX Reunion Nacional de Optica. Orense, Spain (2009)

"Fabrication of Microlens by Nd:YVO₄ laser irradiation of glass frit layers", D. Nieto, María Teresa Flores-Arias and Carlos Gómez-Reino CLEO Europe. Munich, Deutschland (2009)

"Fabricación de guías de onda en substratos de vidrio planos mediante tecnología Sol-Gel" F. Rey-García, D. Nieto, C. Gómez-Reino, M.T. Flores-Arias, G.F. De la Fuente, A. Durán, Y. Castro XLVIII Congreso Anual de la Sociedad Española de Cerámica y Vidrio Oviedo, Spain (2008)

"Replication of Si moulds microlenses with glass" D. Nieto. M. T. Flores-Arias, Antonio Castelo, Carlos Gómez-Reino 14 Microoptics Conference, MOC08. Brussels, Belgium (2008).

"Silicon moulds of microlenses for different replicación techniques", Albero, L. Nieradko, C. Gorecki, H. Ottevaere, V. Gomez, S. Van Overmeire, N. Passily, B. Paivanranta, D. Nieto, M. T. Flores-Arias, C. Gómez-Reino. 14 Microoptics Conference-MOC08. Brussels, Belgium (2008).

"Design of reconfigurable GRIN planar optical interconnects" Photonics C. Gómez-Reino, M.T. Flores-Arias, M.V. Pérez, C.Bao, A.Castelo, and D. Nieto Europe, Strabourg, France (2008)

"Fabrication and characterisation of glassing engraved waveguides" F. Rey-García, D. Nieto, C. Gómez-Reino, M.T. Flores-Arias, M.V. Pérez, V. Lennikov and G.F. De la Fuente Congreso Franco-Español de Química y Física del Estado Sólido, Clermont-Ferrand, France (2008)

"Fabricación de guías de onda en sustratos de vidrio planos", F. Rey-García, D. Nieto, C. Gómez-Reino, M.T. Flores-Arias, M.V. Pérez, C. Bao, V.V. Lennikovy G.F. De la Fuente. Congreso Anual de la Sociedad Española de Cerámica y Vidrio, Toledo, Spain (2007)

"Fabricación de guías mediante el recubrimiento de sustratos de vidrio planos con fritas cerámicas". F. Rey-García, D. Nieto, C. Gómez-Reino, M.T. Flores-Arias, M.V. Pérez, V. Lennikov and G.F. De la Fuente Optoelectronics conference 2007, Bilbao, Spain, (2007)

"Preparation of planar waveguides on planar substrates". F. Rey-García, D. Nieto, C. Gómez-Reino, M.T. Flores-Arias, M.V. Pérez, V. Lennikov and G.F. De la Fuente Conference on Solid State Chemistry XI, Caen, France (2007)

"Fabrication of planar waveguides via coating of planar glass substrates with ceramic frits", F. Rey-García, D. Nieto, C. Gómez-Reino, M.T. Flores-Arias, A. Castelo, M.V. Pérez, C. Bao, V. Lennikov y G.F. De la Fuente Second General Scientific Networking Meeting, Florence, Italy (2007).

"Temperature dependence of laser backwriting process on glass", Castelo; D. Nieto; M.T.Flores-Arias; C.Bao; M.V.Perez; C.Gomez-Reino; C.I. López-Gascón; X. de la Fuente; R. Rangel-Rojo. Photonics Europe 2006: Photonics Applications, Proc. SPIE vol. 6185, Strasbourg, France (2006)

"Efecto Lau en medios GRIN: Sistema ABCD", García Allegue Miguel C, Nieto Daniel, Flores Arias María Teresa, Gómez-Reino Carnota Carlos. Reunión Nacional de Óptica, Alicante, España (2006)

"Nuevas técnicas de fabricación de guías de onda planas sobre sustratos de vidrio". Castelo A. , Nieto D. , Flores-Arias M. T. , Bao Varela C, Pérez Martín M. V. , Gómez-Reino C. , López Gascón I., de la Fuente G., Rangel-Rojo R. Reunión Nacional de Óptica, Alicante, España (2006)

"Escritura Laser en Vidrio mediante ablacion de muestras metalicas: Estudio para diferentes velocidades de trabajo", A. Castelo, D. Nieto, C. Bao, M. Flores-Arias, C. Gomez-Reino, G.F. De la Fuente, XXX Reunión Bienal de la Real Sociedad Española de Física y 15º encuentro Ibero para la enseñanza de la Física, Orense, Spain (2005)

"Lau effect in GRIN media", Miguel Garcia-Allegue,D. Nieto, Maria Teresa Flores-Arias and Carlos Gomez-Reino International Congress on Optics and Optoelectronics,Warsaw, Poland (2005)

"Laser Backwriting Process on Glass via Ablation of Metal Targets", A. Castelo, D. Nieto, M.T. Flores-Arias, M.V. Perez, C. López-Gascón, G.F. de la Fuente, Congress on Optics and Optoelectronics, Warsaw, Poland (28/08- 02/09/2005)

"Escritura láser en vidrio por ablación de muestras metálicas", Castelo, D. Nieto, M.T. Flores-Arias, C. Gómez-Reino y G. De La Fuente, Española de Optoelectronica, Alicante Spain (13-15 July 2005)

"Fabrication and characterization of phase gratings on PbO-SiO₂ glasses by laser irradiation", A.Castelo, D.Nieto, C.Bao, M.T. Flores-Arias and M.V. Perez, Microoptics conference, Jena, Germany (28/08- 01/09/2004)

Workshop presentation

"Laser micro-structuring of glass materials", 4th Workshop, Marie Curie Actions – LOA, UMR 7639 du CNRS, laboratoire commun de l'ENSTA-Paris Tech et de l'Ecole Polytechnique, Palaiseau, (15-16 July 2010)

"Enhanced laser ablation of glass using thin films" The first workshop: Short pulse laser processing of thin films, Oxford, United Kingdom (24-April 2012)